eXPRESS Polymer Letters Vol.9, No.9 (2015) 756
Available online at www.expresspolymlett.com
DOI: 10.3144/expresspolymlett.2015.70

Editorial corner – a personal view

Using thermogravimetric analysis to determine polymer thermal stability: Relevance of changes in onset temperature of mass loss

A. S. Luyt[*]

Center for Advanced Materials, Qatar University, Doha, Qatar

When one reads through publications, especially in the field of polymer composites and nanocomposites, where composite samples were characterised, thermogravimetric analysis (TGA) data are almost always presented as part of a whole range of analysis methods. Most of the time the shifting of the TGA mass loss steps to higher temperatures is interpreted as being indicative of delays in the thermal degradation process and hence improvements in the thermal stability of the polymer(s) brought about by the presence of the filler (nano)particles.

The question one should ask oneself: Is it possible to measure the onset of degradation of a polymer or composite by using TGA, or does one only measure the onset of mass loss? Of course one only measures the onset of mass loss, which means that anything that may delay the transport of volatile degradation products out of the composite will cause a delay in the evaporation of these products, and the onset of mass loss will only be seen after a longer time or at a higher temperature, depending on whether the analysis was performed as function of time or temperature. This means that the (nano) filler probably had no effect on the thermal stability of the polymer matrix, but that it either contributed to the formation of a carbonaceous char layer or strongly interacted with the volatile degradation products, both of which would retard the diffusion of these degradation products out of the polymer. This would give rise to the mass loss step starting at higher temperatures (after longer periods of time) giving the impression of an apparent increase in thermal stability.

On the other hand, one cannot neglect the possibility that the (nano)filler can retard the actual degradation process though strong interaction with the polymer chains and/or free radical chains, which can restrict the chain mobility and slow down the degradation propagation reactions. Whatever the reason for the delayed onset of mass loss, one has to delve deeper to find the real reason and not just assume that it is the result of the (nano)filler improving the thermal stability of the polymer. It is also important to realise that, although the onset of degradation is not necessarily delayed in the presence of (nano)filler particles, any delay in the volatilization of the degradation products (which is measurable with TGA) is an important factor to keep in mind regarding the flammability of the polymer.

Prof. Dr. Adriaan Stephanus Luyt
Member of International Advisory Board

[*]Corresponding author, e-mail: aluyt@qu.edu.qa

eXPRESS Polymer Letters Vol.9, No.9 (2015) 757–763
Available online at www.expresspolymlett.com
DOI: 10.3144/expresspolymlett.2015.71

Plant oil-based shape memory polymer using acrylic monolith

T. Tsujimoto[*], *E. Ohta, H. Uyama*

Department of Applied Chemistry, Graduate School of Engineering, Osaka University, Yamadaoka 2-1, Suita, 565-0871 Osaka, Japan

Received 21 January 2015; accepted in revised form 15 March 2015

Abstract. This article deals with the synthesis of a plant oil-based material using acrylic monolith. An acrylic monolith bearing oxirane groups was prepared via simple technique that involved the dissolution of poly(glycidyl methacrylate-*co*-methyl methacrylate) (PGMA) in ethanolic – aqueous solution by heating and subsequent cooling. The PGMA monolith had topologically porous structure, which was attributed to the phase separation of the polymer solution. The PGMA monolith was impregnated by epoxidized soybean oil (ESO) containing thermally-latent catalyst, and the subsequent curing produced a crosslinked material with relatively good transparency. The Young's modulus and the tensile strength of polyESO/PGMA increased compared with the ESO homopolymer. The strain at break of polyESO/PGMA was larger than that of the ESO homopolymer and crosslinked PGMA. Furthermore, polyESO/PGMA exhibited good shape memory-recovery behavior.

Keywords: *polymer composites, renewable resource, epoxidized soybean oil, monolith, shape memory polymer*

1. Introduction

The depletion of fossil fuel and the environmental issues of petroleum-based materials piqued large interest in renewable bio-based products synthesized from natural resources. The use of biomass to produce energy and chemicals is currently recommended for the reduction of fossil fuel utilization and carbon dioxide emissions involved in global warming. Furthermore, bio-based materials may offer the advantages of biodegradability in composting subsequent to their primary use [1, 2].

Plant oils, such as linseed, sunflower, soybean, and palm oils, are one of the cheapest and most abundant renewable resources, and their uses as starting materials offer numerous advantages, such as low toxicity and inherent biodegradability [3]. Triglyceride natural oils have been utilized extensively for coatings, inks, plasticizers, lubricants, resins and agrochemicals in addition to their applications in the food industry. Most of plant oil-based polymeric materials, however, do not show the properties of rigidity and strength required for structural applications by themselves. Epoxidized plant oils are synthesized from common unsaturated plant oils, such as linseed, soybean, and palm oils, by standard epoxidation reaction. Epoxidized soybean oil (ESO) is commercially available, and has been used as plasticizers for poly(vinyl chloride), chlorinated rubber, and poly(vinyl alcohol) emulsion, and starting materials for polyurethane foam [4–7]. Furthermore, various polymerizations of epoxidized plant oils can be achieved by acid anhydrides, photoinitiators, latent catalysts, or acid catalysts. These epoxy compounds from renewable resources possess a high potential as a starting material for bio-based thermosetting plastics and coatings [8–10]. Epoxidized plant oils were cured in the presence of inorganic chemicals to produce organic-inorganic hybrid materials [11–13]. Recently,

[*]Corresponding author, e-mail: tsujimoto@chem.eng.osaka-u.ac.jp

a green composite was prepared by the curing of ESO in the presence of porous poly(3-hydroxybutyrate). The porous structure of poly(3-hydroxybutyrate) improved the mechanical properties of the ESO-based network polymer [14].

Shape memory materials have a sensitive response to external stimuli, such as temperature, light, pH, humidity, chemicals, and electricity. In recent years, shape memory polymers have received increasing attention because of their good processability, low cost, and high recovery ability, and have been used in various fields [15–25]. Thermally triggered shape memory polymer is first processed to receive a permanent shape. Above a given temperature range (switching temperature), shape memory polymer can be deformed into a temporary shape that is fixed by cooling under external stress. When the sample is reheated above the switching temperature, the permanent shape is recovered. Although bio-based shape memory polymers including poly (lactic acid) and polyglycolid were developed, most of them were block polymers prepared by a two-stage synthesis or coupling method.

A monolith is defined as a block structured material which consists of continuous substructures of regular or irregular channels [26]. Owing to the exciting properties including high specific surface area, high permeability, low density, and fast mass transfer performance, monoliths have received a considerable amount of attention in various fields [27–31]. Polymer monolithic materials are often prepared by the copolymerization of a monomer and a crosslinker in the presence of a porogen. In this case, the pore in the polymer monolith is fabricated as aggregation of polymer grains formed though an abrupt increase of molecular weight during polymerization. The resultant porous structure is disordered in shape, and it is accompanied by difficulties in the precise control of the porous structural parameters such as pore and skeleton size. Recently, we have reported the fabrication of polymer monolith by thermally induced phase separation (TIPS) [32, 33]. This method is an excellent way to prepare microcellular foams and membranes with controlled morphologies. In this study, an acrylic polymer monolith containing oxirane groups was fabricated by TIPS and used as a reinforcement material for the ESO polymer. The resulting material showed relatively good transparency with improvements in the mechanical properties. Furthermore, the shape memory properties of the resulting material were investigated.

2. Experimental

2.1. Materials

ESO and a thermally-latent cationic catalyst (benzylsulfonium hexafluoroantimonate derivative, commercial name: Sun-Aid SI-60L) were gifts from Mizutani Paint Co., (Osaka, Japan) and Sanshin Chemical Industry Co. (Yamaguchi, Japan), respectively. The number of oxirane groups of ESO was 3.7 per a molecule, determined by nuclear magnetic resonance (^{1}H NMR). Poly(glycidyl methacrylate-*co*-methyl methacrylate) (PGMA) was synthesized by common radical polymerization by using azobisisobutyronitrile as an initiator. The molecular weight of PGMA was determined by size exclusion chromatography (SEC) ($M_w = 1.9\times10^5$, $M_w/M_n = 3.2$). The molar ratio of glycidyl methacrylate unit determined by ^{1}H NMR was 20%. Other reagents and solvents were commercially available and used as received.

2.2. Fabrication of PGMA monolith

The following was a procedure for the fabrication of PGMA monolith. PGMA powder (160 mg) was dissolved in a mixture of ethanol and water (2 mL, 80/20 vol%) at 80°C for 15 min, and the solution was then cooled at 20°C. After 2 h, the resulting white solid was washed with ethanol several times to obtain a PGMA monolith.

2.3. Synthesis of polyESO/PGMA

The synthesis procedure of polyESO/PGMA was carried out as follows. PGMA monolith was immersed in ESO containing thermally-latent catalyst, followed by the removal of residual ethanol under reduced pressure (ca. 800 Pa) at room temperature. Then, the sample was heated at 110°C for 2 h under a pressure of 5 MPa by using a hot-pressing machine (C180, Imoto Machinery Co., Kyoto , Japan) to produce a polyESO/PGMA. The ESO homopolymer and the crosslinked PGMA were synthesized by using thermally-latent catalyst at 110°C for 2 h.

2.4. Investigation of shape memory-recovery behaviors of polyESO/PGMA

The polyESO/PGMA in strip form was prepared as a permanent shape, and was deformed to the spiral form by wrapping around a Teflon rod at 130°C.

The temporary shape of the polyESO/PGMA was fixed by the subsequent cooling to room temperature. Upon reheating at 130°C, the deformed shape was restored to its original shape.

2.5. Measurements

^{1}H NMR spectrum was recorded on a DPX-400 instrument (Bruker Biospin Co., MA, USA). SEC analysis was carried out by using a SC8020 apparatus (Tosoh, Tokyo, Japan) with a refractive index detector at 40°C under the following conditions: TOSOH TSKgel G4000 column and chloroform eluent at a flow rate of 1.0 mL·min^{-1}. The calibration curve was obtained using polystyrene standards. Fourier-transform infrared spectroscopy (FT-IR) was measured by a Spectrum One (Perkin-Elmer Inc., MA, USA) (4 scans). Scanning electron microscopic (SEM) analysis was carried out by using a SU-3500 instrument (Hitachi High-Technologies Co., Tokyo, Japan). Dynamic viscoelasticity analysis (DMA) controlling strain/amplitude was performed by using a DMS6100 (Hitachi High-Tech Science Co., Tokyo, Japan) with a frequency of 1 Hz at a heating rate of 3°C·min^{-1}. Tensile properties were measured by a EZ Graph (Shimadzu Co., Kyoto, Japan) with a crosshead speed of 5 mm·min^{-1}. The sample was cut into a plate shape of 20 mm×10 mm×0.1 mm.

3. Results and discussion

3.1. Synthesis of polyESO/PGMA

In general, water and lower aliphatic alcohols are regarded as non-solvents or poor solvents for acrylic polymers including poly(methyl methacrylate) (PMMA) and its derivatives. However, acrylic polymers are dissolved in a mixture of aliphatic alcohol and water by heating, this phenomenon is called pseudo-classical cosolvent system [34]. Recently, we have developed a new fabrication technique of acrylic monoliths by TIPS using temperature dependence of solubility for the cosolvent. PGMA powder was dissolved in a mixture of ethanol and water (80/20 vol%) at 60°C, and the solution was then allowed to cool at room temperature to yield a white monolithic material retaining the shape of vessel. The general procedure is illustrated in Figure 1.

The morphology of the resulting PGMA monolith was homogeneous macroporous with three-dimensional interconnected fibrous structure (Figure 2). In the process, a homogeneous polymer solution was cooled below the binodal line, and the Gibbs free energy of the system increased, which consequently resulted in phase separation. The phase separation continued until the combination of two phases reached stable condition with lowest energy. In other words, the solution separated into a polymer-rich phase and a polymer-lean phase, and the polymer-rich phase became immobilized by gelation and vitrification.

In this study, the PGMA monolith was used as a reinforcement material for the ESO polymer. A polyESO/PGMA was prepared by an immersion method. This method relies on the penetration of ESO into the PGMA monolith. The PGMA monolith was immersed in ESO containing thermally-latent catalyst, followed by vacuum treatment to remove the residue ethanol.

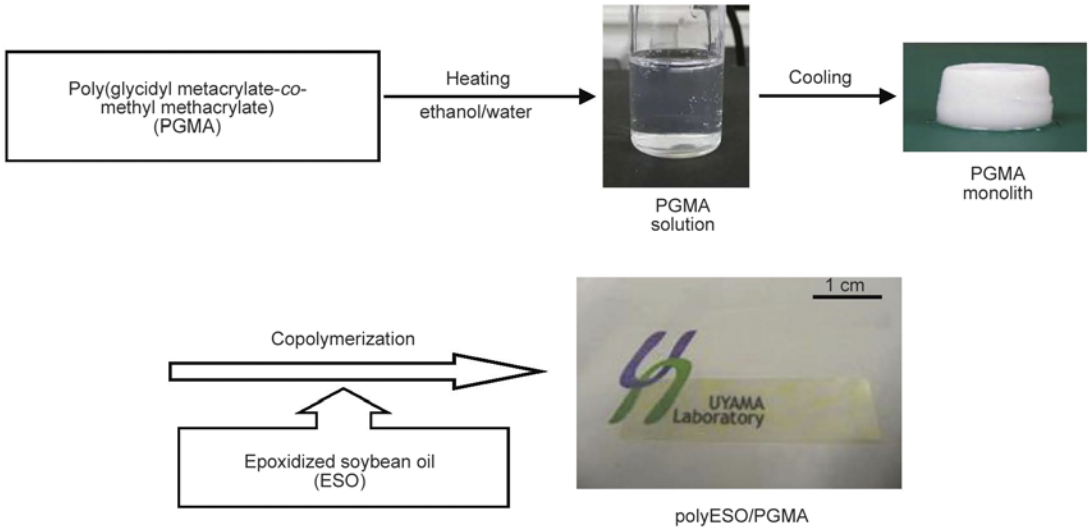

Figure 1. General procedure for preparation of PGMA monolith and polyESO/PGMA

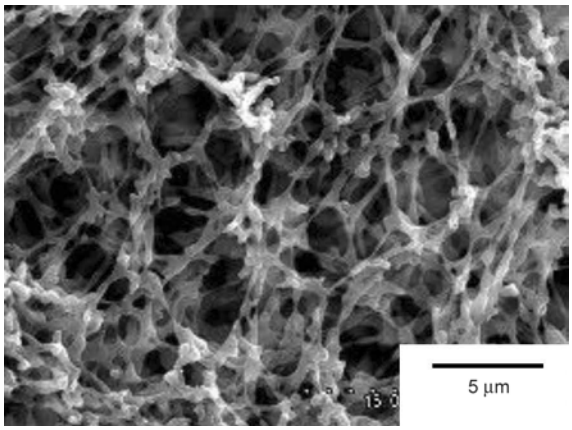

Figure 2. SEM image of PGMA monolith

Then, crosslinking reaction was carried out at 110°C to yield a polyESO/PGMA. The resulting material was insoluble in any organic solvent. The ratio of ESO component, determined by weight change, was 50 wt%. During the reaction, the oxirane groups of ESO and PGMA reacted with each other. The polyESO/PGMA showed relatively high transparency, and the transmittance at 700 nm was more than 75%. On the other hand, the blend of ESO and PGMA prepared by solvent casting was opaque due to the immiscibility of PGMA with ESO. These data suggest that the porous structure of the monolith was retained without shrinkage and that the pore of the PGMA monolith was filled by ESO component.

In the FT-IR spectrum of the polyESO/PGMA, characteristic peaks at ca. 840 cm^{-1}, ascribed to the C–C antisymmetric stretching of the oxirane groups of ESO and PGMA, disappeared, and a broad peak centered at 3400 cm^{-1}, ascribed to the O–H stretching, was observed. These results indicate that the oxirane groups of ESO and PGMA are consumed to form hydroxyl-terminated network polymer.

3.2. Thermal and mechanical properties of polyESO/PGMA

In order to evaluate the effect of the incorporation of PGMA monolith, dynamic viscoelasticity analysis as a function of temperature was performed. The storage modulus and loss factor of the ESO homopolymer, the crosslinked PGMA, and the polyESO/PGMA are shown in Figure 3. In the ESO homopolymer, a rapid decrease of storage modulus was observed at –25°C. The storage modulus of the crosslinked PGMA also decreased remarkably at 120°C, due to low crosslinking density. On the other hand, it can be found that the storage modulus of polyESO/PGMA drops stepwise, which is attributed to the glass transitions of ESO polymer and PGMA. This result indicates that ESO polymer and the PGMA monolith are immiscible. At lower temperature, the polyESO/PGMA was glassy with a storage modulus of about 4.0 GPa, and the storage modulus dropped at –25°C, giving rise to the first rubbery state. Upon further heating, the storage modulus dropped again at 120°C to yield the second rubbery state. In second rubbery state, the storage modulus of polyESO/PGMA was about 16 MPa which is higher than that of the crosslinked PGMA, indicating that the oxirane groups of ESO and PGMA react with each other to form the network structure. Figure 4 shows the stress-strain curves of the ESO homopolymer, the crosslinked PGMA, and the polyESO/PGMA. The Young's modulus and the tensile strength of the polyESO/PGMA were larger than those of the ESO homopolymer. These behaviors are related to the three-dimensional porous structure of the PGMA monolith, suggesting that the PGMA monolith effectively reinforces ESO polymer. The ESO homopolymer and the crosslinked PGMA fractured at 14 and 8%, respectively. On the other hand, the polyESO/PGMA was improved in brittleness,

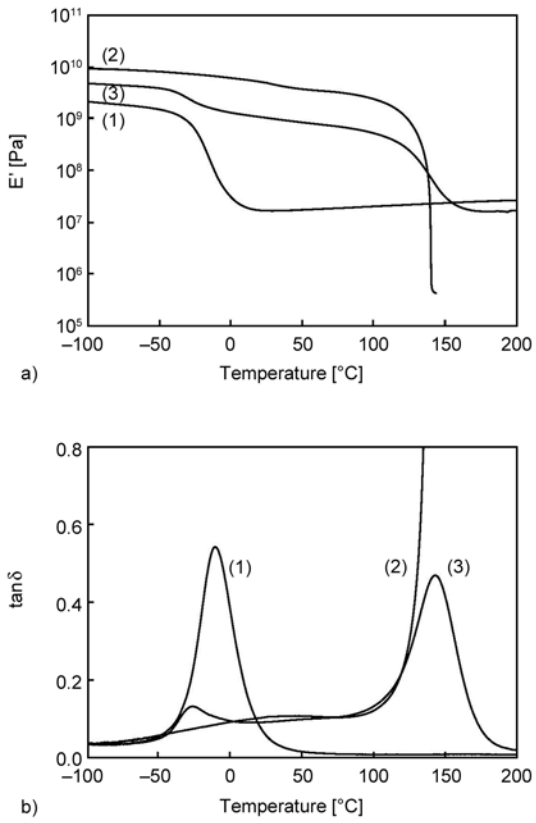

Figure 3. Dynamic viscoelasticity of (1) ESO homopolymer, (2) crosslinked PGMA, and (3) polyESO/PGMA; (a) storage modulus, (b) loss factor

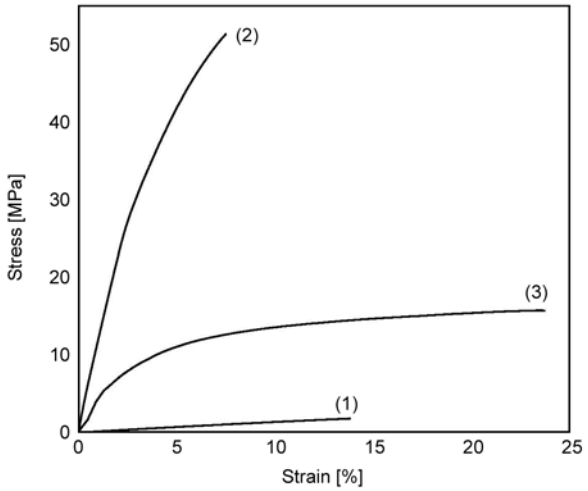

Figure 4. Stress-strain curves of (1) ESO homopolymer, (2) crosslinked PGMA, and (3) polyESO/PGMA

and the strain at break of the polyESO/PGMA was 24%.

3.3. Shape memory-recovery behaviors of polyESO/PGMA

The shape memory-recovery behaviors of the polyESO/PGMA are demonstrated in Figure 5. In this study, the shape memory-recovery behaviors were activated by the glass transition of PGMA component as a switching temperature. The polyESO/PGMA was easily deformed above the glass transition temperature of PGMA component. The ESO homopolymer could not be deformed because of the brittleness. The temporary shape of the polyESO/PGMA was fixed by the subsequent cooling to room temperature. Upon reheating above the glass transition temperature of PGMA component, the deformed shape was recovered to its original shape. On the other hand, the shape of the crosslinked PGMA was not returned to the original shape. Furthermore, the shape memory-recovery behaviors of the polyESO/PGMA were repeatable. The plausible shape memory-recovery mechanism is as follows. The driving force of shape recovery is the elastic force of ESO polymer generated during the deformation. Above the switching temperature, PGMA component is in rubbery state and the sample is easily deformed. After the subsequent cooling, PGMA component becomes glassy and the temporary shape is fixed with the internal stress of ESO polymer. Upon reheating above the switching temperature, the mobility of PGMA chains becomes larger, and the shape of the sample returns to the original shape by the entropy elasticity of ESO polymer.

4. Conclusions

In this study, an acrylic monolith bearing oxirane groups was fabricated via thermally induced phase separation in ethanol aqueous solution. The resulting PGMA monolith was a piece of white material with three-dimensional interconnected porous structure. The PGMA monolith was immersed in ESO containing thermally-latent catalyst under vacuum condition, and the subsequent crosslinking reaction produced polyESO/PGMA with relatively good transparency. The DMA result of the polyESO/PGMA showed two glass transitions, due to the immiscibility of PGMA with ESO. The Young's modulus and the tensile strength of the polyESO/PGMA were larger than those of the ESO homopolymer. The incorporation of the PGMA monolith also increased the strain at break, indicating that the resulting material is effectively reinforced without sacrificing toughness. Furthermore, the polyESO/PGMA exhibited excellent shape memory property.

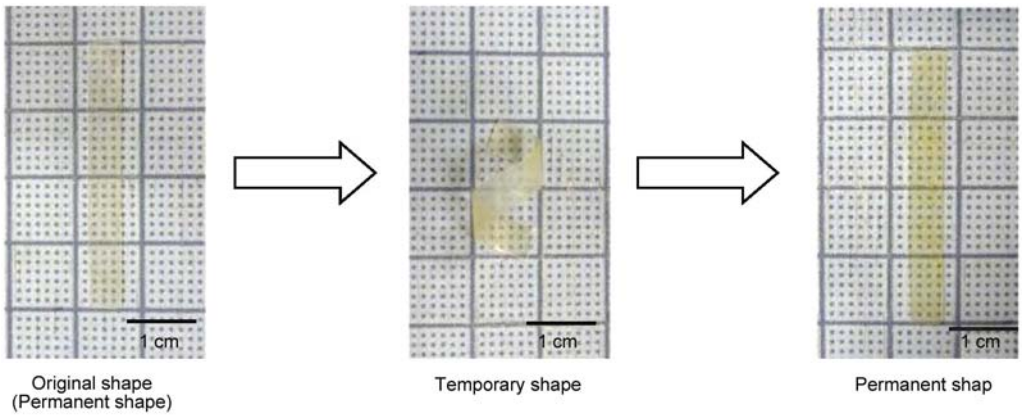

Figure 5. Shape memory-recovery behaviors for polyESO/PGMA

Acknowledgements

This study supported by a Grant-in-Aid for Young Scientists from Japan Society for the Promotion of Science (JSPS) (No. 268101140).

References

[1] Ragauskas A. J., Williams C. K., Davison B. H., Britovsek G., Cairney J., Eckert C. A., Frederick Jr. W. J., Hallett J. P., Leak D. J., Liotta C. L., Mielenz J. R., Murphy R., Templer R., Tschaplinski T.: The path forward for biofuels and biomaterials. Science, **311**, 484–489 (2006).
DOI: 10.1126/science.1114736

[2] Nagarajan V., Mohanty A. K., Misra M.: Sustainable green composites: Value addition to agricultural residues and perennial grasses. ACS Sustainable Chemisry and Engineering, **1**, 325–333 (2013).
DOI: 10.1021/sc300084z

[3] Quirino R. L., Garrison T. F., Kessler M. R.: Matrices from vegetable oils, cashew nut shell liquid, and other relevant systems for biocomposite applications. Green Chemistry, **16**, 1700–1715 (2014).
DOI: 10.1039/c3gc41811a

[4] Swern D., Billen G. N., Findley T. W., Scanlan J. T.: Hydroxylation of monounsaturated fatty materials with hydrogen peroxide. Journal of the American Chemical Society, **67**, 1786–1789 (1945).
DOI: 10.1021/ja01226a050

[5] Petrović Z. S., Zhang W., Javni I.: Structure and properties of polyurethanes prepared from triglyceride polyols by ozonolysis. Biomacromolecules, **6**, 713–719 (2005).
DOI: 10.1021/bm049451s

[6] Biresaw G., Liu Z. S., Erhan S. Z.: Investigation of the surface properties of polymeric soaps obtained by ring-opening polymerization of epoxidized soybean oil. Journal of Applied Polymer Science, **108**, 1976–1985 (2008).
DOI: 10.1002/app.27784

[7] Saithai P., Lecomte J., Dubreucq E., Tanrattanakul V.: Effects of different epoxidation methods of soybean oil on the characteristics of acrylated epoxidized soybean oil-*co*-poly(methyl methacrylate) copolymer. Express Polymer Letters, **7**, 910–924 (2013).
DOI: 10.3144/expresspolymlett.2013.89

[8] Chakrapani S., Crivello J. V.: Synthesis and photoinitiated cationic polymerization of epoxidized castor oil and its derivatives. Journal of Macromolecular Science Part A: Pure and Applied Chemistry, **35**, 1–20 (1998).
DOI: 10.1080/10601329808001959

[9] Tran P., Graiver D., Narayan R.: Biocomposites synthesized from chemically modified soy oil and biofibers. Journal of Applied Polymer Science, **102**, 69–75 (2006).
DOI: 10.1002/app.22265

[10] Wang R., Schuman T. P.: Vegetable oil-derived epoxy monomers and polymer blends: A comparative study with review. Express Polymer Letters, **7**, 272–292 (2013).
DOI: 10.3144/expresspolymlett.2013.25

[11] Tsujimoto T., Uyama H., Kobayashi S.: Green nanocomposites from renewable resources: Biodegradable plant oil-silica hybrid coatings. Macromolecular Rapid Communications, **24**, 711–714 (2003).
DOI: 10.1002/marc.200350015

[12] Miyagawa H., Misra M., Drzal L. T. Mohanty A. K.: Novel biobased nanocomposites from functionalized vegetable oil and organically-modified layered silicate clay. Polymer, **46**, 445–453 (2005).
DOI: 10.1016/j.polymer.2004.11.031

[13] Lligadas G., Ronda J. C., Galià M., Cádiz V.: Bionanocomposites from renewable resources: Epoxidized linseed oil–polyhedral oligomeric silsesquioxanes hybrid materials. Biomacromolecules, **7**, 3521–3526 (2006).
DOI: 10.1021/bm060703u

[14] Hosoda N., Tsujimoto T., Uyama H.: Plant oil-based green composite using porous poly(3-hydroxybutyrate). Polymer Journal, **46**, 301–306 (2014).
DOI: 10.1038/pj.2014.1

[15] Feninat F. E., Laroche G., Fiset M., Mantovani D.: Shape memory materials for biomedical applications. Advanced Engineering Materials, **4**, 91–104 (2002).
DOI: 10.1002/1527-2648(200203)4:3<91::AID-ADEM91>3.0.CO;2-B

[16] Yamashiro M., Inoue K., Iji M.: Recyclable shape-memory and mechanical strength of poly(lactic acid) compounds cross-linked by thermo-reversible Diels-Alder reaction. Polymer Journal, **40**, 657–662 (2008).
DOI: 10.1295/polymj.PJ2008042

[17] Kolesov I. S., Radusch H-J.: Multiple shape-memory behavior and thermal-mechanical properties of peroxide cross-linked blends of linear and short-chain branched polyethylenes. Express Polymer Letters, **2**, 461–473 (2008).
DOI: 10.3144/expresspolymlett.2008.56

[18] Luo X., Mather P. T.: Triple-shape polymeric composites (TSPCs). Advanced Functional Materials, **20**, 2649–2656 (2010).
DOI: 10.1002/adfm.201000052

[19] Guo B., Chen Y., Lei Y., Zhang L., Zhou W. Y., Rabie A. B. M., Zhao J.: Biobased poly(propylene sebacate) as shape memory polymer with tunable switching temperature for potential biomedical applications. Biomacromolecules, **12**, 1312–1321 (2011).
DOI: 10.1021/bm2000378

[20] Ratna D., Karger-Kocsis J.: Shape memory polymer system of semi-interpenetrating network structure composed of crosslinked poly (methyl methacrylate) and poly(ethylene oxide). Polymer, **52**, 1063–1070 (2011).
DOI: 10.1016/j.polymer.2010.12.054

[21] Julich-Gruner K. K., Löwenberg C., Neffe A. T., Behl M., Lendlein A.: Recent trends in the chemistry of shape-memory polymers. Macromolecular Chemistry and Physics, **214**, 527–536 (2013).
DOI: 10.1002/macp.201200607

[22] Fejős M., Molnár K., Karger-Kocsis J.: Epoxy/polycaprolactone systems with triple-shape memory effect: Electrospun nanoweb with and without graphene *versus co*-continuous morphology. Materials, **6**, 4489–4504 (2013).
DOI: 10.3390/ma6104489

[23] Tsujimoto T., Uyama H.: Full biobased polymeric material from plant oil and poly(lactic acid) with a shape memory property. ACS Sustainable Chemisry and Engineering, **2**, 2057–2062 (2014).
DOI: 10.1021/sc500310s

[24] Tsujimoto T., Toshimitsu K., Uyama H., Takeno S., Nakazawa Y.: Maleated *trans*-1,4-polyisoprene from *Eucommia ulmoides* Oliver with dynamic network structure and its shape memory property. Polymer, **55**, 6488–6493 (2014).
DOI: 10.1016/j.polymer.2014.10.035

[25] Karger-Kocsis J. Kéki S.: Biodegradable polyester-based shape memory polymers: Concepts of (supra) molecular architecturing. Express Polymer Letters, **8**, 397–412 (2014).
DOI: 10.3144/expresspolymlett.2014.44

[26] Ceylan S., Kirschning A.: Organic synthesis with mini flow reactors using immobilised catalysts. in 'Recoverable and recyclable catalysts' (ed.: Benaglia M.) Wiley, New York, 379–410 (2009).

[27] Hüsing N., Schubert U.: Aerogels–airy materials: Chemistry, structure, and properties. Angewandte Chemie International Edition, **37**, 22–45 (1998).
DOI: 10.1002/(SICI)1521-3773(19980202)37:1/2<22::AID-ANIE22>3.0.CO;2-I

[28] Mayr M., Mayr B., Buchmeiser M. R.: Monolithic materials: New high-performance supports for permanently immobilized metathesis catalysts. Angewante Chemie International Edition, **40**, 3839–3842 (2001).
DOI: 10.1002/1521-3773(20011015)40:20<3839::AID-ANIE3839>3.0.CO;2-O

[29] Hosoda N., Tsujimoto T. Uyama H.: Green composite of poly(3-hydroxybutyrate-*co*-3-hydroxyhexanoate) reinforced with porous cellulose. ACS Sustainable Chemisry and Engineering, **2**, 248–253 (2014).
DOI: 10.1021/sc400290y

[30] Wang H., Zhang H., Lv Y., Svec F., Tan T.: Polymer monoliths with chelating functionalities for solid phase extraction of metal ions from water. Journal of Chromatography A, **1343**, 128–134 (2014).
DOI: 10.1016/j.chroma.2014.03.072

[31] Hasegawa G., Kanamori K., Nakanishi K., Yamago S.: Fabrication of highly crosslinked methacrylate-based polymer monoliths with well-defined macropores via living radical polymerization. Polymer, **52**, 4644–4647 (2011).
DOI: 10.1016/j.polymer.2011.08.028

[32] Okada K., Nandi M., Maruyama J., Oka T., Tsujimoto T., Kondoh K., Uyama H.: Fabrication of mesoporous polymer monolith: A template-free approach. Chemical Communications, **47**, 7422–7424 (2011).
DOI: 10.1039/c1cc12402a

[33] Yoneda S., Han W., Hasegawa U., Uyama H.: Facile fabrication of poly(methyl methacrylate) monolith *via* thermally induced phase separation by utilizing unique cosolvency. Polymer, **55**, 3212–3216 (2014).
DOI: 10.1016/j.polymer.2014.05.031

[34] Cowie J. M. G., Mohsin M. A., MacEwen I. J.: Alcohol-water cosolvent systems for poly(methyl methacrylate). Polymer, **28**, 1569–1572 (1987).
DOI: 10.1016/0032-3861(87)90360-0

eXPRESS Polymer Letters Vol.9, No.9 (2015) 764–772
Available online at www.expresspolymlett.com
DOI: 10.3144/expresspolymlett.2015.72

Development of novel antibacterial active, HaCaT biocompatible and biodegradable CA-*g*-P(3HB)-EC biocomposites with caffeic acid as a functional entity

H. M. N. Iqbal[1*], *G. Kyazze*[1], *I. C. Locke*[1], *T. Tron*[2], *T. Keshavarz*[1]

[1]Applied Biotechnology Research Group, Department of Life Sciences, Faculty of Science and Technology, University of Westminster, W1W 6UW London, United Kingdom
[2]Aix Marseille Université, CNRS, Centrale Marseille, iSm2 UMR 7313, 13397 Marseille, France

Received 1 January 2015; accepted in revised form 26 March 2015

Abstract. We have developed novel composites by grafting caffeic acid (CA) onto the P(3HB)-EC based material and laccase from *Trametes versicolor* was used for grafting purposes. The resulting composites were designated as CA-*g*-P(3HB)-EC *i.e.*, P(3HB)-EC (control), 5CA-*g*-P(3HB)-EC, 10CA-*g*-P(3HB)-EC, 15CA-*g*-P(3HB)-EC and 20CA-*g*-P(3HB)-EC. FT-IR (Fourier-transform infrared spectroscopy) was used to examine the functional and elemental groups of the control and laccase-assisted graft composites. Evidently, 15CA-*g*-P(3HB)-EC composite exhibited resilient antibacterial activity against Gram-positive and Gram-negative bacterial strains. Moreover, a significant level of biocompatibility and biodegradability of the CA-*g*-P(3HB)-EC composites was also achieved with the human keratinocytes-like HaCaT cells and soil burial evaluation, respectively. In conclusion, the newly developed novel composites with multi characteristics could well represent the new wave of biomaterials for medical applications, and more specifically have promising future in the infection free would dressings, burn and/or skin regeneration field due to their sophisticated characteristics.

Keywords: *polymer composites, enzymatic grafting, laccase, biocompatible, biodegradable*

1. Introduction

Bio-polymers generated from natural sources are non-toxic in nature and therefore should be extraordinarily suitable for biomedical applications such as tissue engineering. Among the most promising and well-characterised bio-polymers of natural origin, P(3HB) and cellulose are of particular interest to prepare composites with novel functionalities [1, 2]. Depending on the physiochemical nature and compatibility of the individual constituent surfaces, either P(3HB) or cellulose, various interactions can occur at the interface. Interfacial chemical reactions can lead to various intermolecular bonds such as hydrogen bonding type interactions. Surface functionalities of P(3HB) and cellulose include moderately polar (>C=O) and polar groups (–OH and –COOH) and one primary and two secondary hydroxyl groups, respectively which possibly interact, and generate some new bonds during composite formation [3, 4]. In recent years, a great interest has grown in the development of polymeric materials or composites with multifunctional characteristics, such as antibacterial, anticorrosive, biocompatible and biodegradable, to explore their potential for wider use in a variety of applications *e.g.* biomedical, pharmaceutical, drug delivery, food packaging, sanitary materials, household, energy and military items [2, 4–8]. In our previous work, novel enzyme-based composites by grafting poly(3-hydroxybutyrate) [P(3HB)] onto the ethyl cellulose (EC) and bacterial cellulose (BC) as

*Corresponding author, e-mail: hafiz.iqbal@my.westminster.ac.uk

a backbone polymers were developed under mild and eco-friendly environment and analysed the improved thermo-mechanical properties conferred to the biomaterials based composites obtained [2, 4, 7]. From the last few years, antimicrobial finishing of medical materials has become extremely important in the production of protective, biocompatible, biodegradable, non-toxic products with respect to the health and safety. This has provided opportunities to expand the use of biomaterials to different applications in the pharmaceutical, medical, tissue engineering, agricultural, and food industries [4–7]. Most phenols like caffeic acid, as natural auxiliaries host antimicrobial activity and can also be grafted to improve or impart existing or antimicrobial properties, respectively. The cross-linking of some of the natural phenolic compounds to different polymers is evidenced after an enzymatic stage with *P. cinnabarinus* laccase [9, 10]. Laccase catalyses the oxidation of aromatic compounds using molecular oxygen as electron acceptor thus has been successfully applied for grafting of phenolic compounds on different natural polymers. In the last decade several authors have shown that laccase treatments can improve physical/chemical properties by producing phenoxy radicals that undergo cross-linking reactions [11–13], thus enhancing and/or imparting completely new properties to the materials, for a better performance, or to create new value-added products. The recent years have also witnessed a revival of the interest for natural materials capable of controlling microbial contaminations due to their fewer side effects and non-toxicity [14, 15]. Thus they hold a great potential and represent a valuable alternative and new challenges for the future to keep under control microbial contamination.

In this work, we have developed novel CA-*g*-P(3HB)-EC composites, which exert strong antibacterial activities. The improved resistance against a wide spectrum of microbes as well as the HaCaT compatibility and biodegradability all indicate that the newly synthesised CA-*g*-P(3HB)-EC based novel composites could be potential candidate biomaterials for medical applications, and more specifically have promising future in the infection free wound dressings, burn and/or skin regeneration field due to their sophisticated characteristics.

2. Experimental section

2.1. Bacterial cultures and maintenance

The pure cultures of the Gram-positive bacteria *i.e.*, *Bacillus subtilis* NCTC 3610 and *Staphylococcus aureus* NCTC 6571 and the Gram-negative *i.e.*, *Escherichia coli* NTCT 10418 and *Pseudomonas aeruginosa* NCTC 10662 were obtained from the culture collection unit of the University of Westminster London, UK. All of the collected strains were streaked on nutrient agar plates and subsequently used for inoculum development. Each strain, separately, was grown overnight in 50 mL sterile nutrient broth at 30°C and 120 rpm. The main constituents of the broth were: 1.0 g/L; yeast extract, 2.0 g/L; peptone, 5.0 g/L; sodium chloride, 5.0 g/L.

2.2. Production and extraction of P(3HB)

The Gram-positive *B. subtilis* NCTC 3610 was used for the production of P(3HB) using a modified G medium (MGM) [16]. After the stipulated fermentation time period (72 h), (P3HB) was extracted from the cells using the chloroform-hypochlorite dispersion method [17]. Isolated P(3HB) was then stored in air tight desiccated jars to keep moisture free and used further in subsequent graft synthesis experiments.

2.3. Grafting of CA onto the P(3HB)-EC

The grafting of CA onto the as-reported P(3HB)-EC based composite [2], was performed by adopting surface dipping and incorporation (SDI) technique. Briefly, the pre-weight P(3HB)-EC composite was dipped into the CA solution in the presence of laccase for 60 min at 30°C. After that weight of the com-

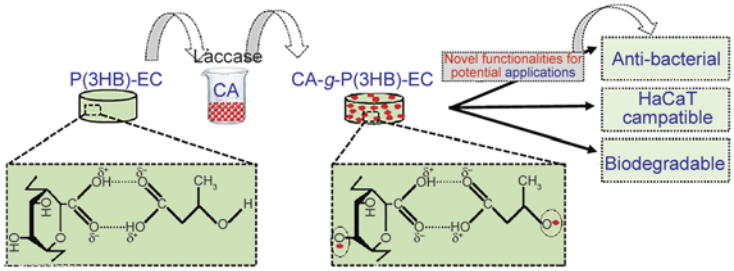

Figure 1. Schematic representation of preparation and evaluation of CA-*g*-P(3HB)-EC composites

posite was recorded in a swollen state followed by incubation at 50°C until fully dried. To eliminate the un-reacted CA monomers each composite was washed three times using sodium malonate buffer and then dried again at 50°C and final dry weight was recorded to calculate the grafting parameters. Subsequently, the resulting composites were designated as P(3HB)-EC, 5CA-*g*-P(3HB)-EC, 10CA-*g*-P(3HB)-EC, 15CA-*g*-P(3HB)-EC and 20CA-*g*-P(3HB)-EC. A possible mechanism of action between CA and P(3HB)-EC composite is shown in Figure 1.

2.4. Fourier transform infrared spectroscopy (FT-IR)

A Perkin Elmer System 2000 FT-IR spectrophotometer was used to identify the structural elements of the individual CA, P(3HB)-EC and CA-*g*-P(3HB)-EC composites. The individual polymers and grafted composites were placed on the diamond crystal, and infrared absorption spectra were recorded from the wavelength region of 4000–500 cm^{-1}. All spectra were collected with 64 scans and 2 cm^{-1} resolution and assigned peak numbers.

2.5. Grafting parameters

The grafting parameters *i.e.*, graft yield (*GY*%), grafting efficiency (*GE*%) and swelling ratio (*SR*%) were measured. Graft yield was calculated in percentage by Equation (1), grafting efficiency was calculated in percentage by Equation (2) and swelling ratio was calculated in percentage by Equation (3):

$$\text{Graft yield} \quad (GY\%) = \frac{W_f - W_i}{W_i} \times 100 \quad (1)$$

$$\text{Grafting efficiency} \quad (GE\%) = \frac{W_f - W_i}{W_s - W_i} \times 100 \quad (2)$$

$$\text{Swelling ratio} \quad (SR\%) = \frac{W_s - W_i}{W_i} \times 100 \quad (3)$$

where, W_i = initial weight before immersion; W_f = final dry weight after immersion; and W_s = weight of a sample in the swollen state.

2.6. Testing antibacterial activity

The antibacterial activities of the P(3HB)-EC and CA-*g*-P(3HB)-EC composites were tested against the aforementioned Gram-positive and Gram-negative strains. An overnight grown spore suspensions containing approximately 10^5 CFU/mL were inoculated onto the sterilised surfaces of the P(3HB)-EC and CA-*g*-P(3HB)-EC composites followed by incubation at 30°C. After the stipulated incubation period (24 h), the bacterial cells were washed twice using 50 mL of phosphate buffer. The CFU/mL in each of the washed suspension was determined by conventional spread-plate method. In comparison with control (initial bacterial count) the CFU/mL values were used to calculate the antibacterial efficacy of the P(3HB)-EC and CA-*g*-P(3HB)-EC composites by Equation (4):

$$\textit{Log reduction} = \textit{Log CFU control} - \textit{Log CFU treated sample} \quad (4)$$

2.7. *In-vitro* cell viability and adherent morphology

HaCaT cell line was adopted to evaluate the cytotoxicity of the P(3HB)-EC and CA-*g*-P(3HB)-EC composites. HaCaT cells at a density of 1×10^5 cells per well were seeded in 24-well tissue culture plates containing P(3HB)-EC and CA-*g*-P(3HB)-EC composites separately. After 1, 3 and 5 days of incubation the culture media were removed and the specimens were rinsed with phosphate buffer saline three times in order to remove the un-attached cells. Cell viability of the adherent cells was measured using neutral red uptake assay. Thermomax micro-plate reader (Model 680, Bio-Rad, CA) was used to record optical density values at 540 nm using Softmax Pro version 4.8 software. Percent cell viability of the test specimens was calculated by Equation (5). Whereas, the adherent morphology of HaCaT cell line seeded onto the P(3HB)-EC and CA-*g*-P(3HB)-EC composites was observed using Nikon light microscope after staining with neutral red dye. After 1 h incubation in dye solution, the stained cells were first washed with PBS and then images were recorded at 100× magnification.

$$\%\ \textit{Cell viability} = \frac{OD_{\text{Test composite}} - OD_{\text{Negative control}}}{OD_{\text{Positive control}}} \quad (5)$$

2.8. Soil burial test

The biodegradability of the P(3HB)-EC and CA-*g*-P(3HB)-EC composites was evaluated using soil burial test as-described earlier by Wattanakornsiri *et al*. [18]. The soil burial test lasted for 6 weeks (42 days).

A set of triplicate samples were buried under the soil surface and after every 7 days of burial, each set was removed, washed with distilled water, dried under ambient environment and loss in weight was recorded. The weight loss was calculated in percentage by Equation (6):

$$\%\ Loss\ in\ weight = \frac{Control\ weight - Loss\ in\ weight}{Control\ weight} \quad (6)$$

3. Results and discussion

3.1. Fourier transform infrared spectroscopy (FT-IR)

An FT-IR was used to examine the functional and elemental groups of CA and P(3HB)-EC and their laccase-assisted graft composites *i.e.*, 5CA-*g*-P(3HB)-EC, 10CA-*g*-P(3HB)-EC, 15CA-*g*-P(3HB)-EC and 20CA-*g*-P(3HB)-EC. In comparison to the untreated caffeic acid as shown in Figure 2, an increase in the absorbance at 1720 cm^{-1} (C=O) band, and 1050–1300 cm^{-1} (C–O) was noticed. The –OH bands overlapped in the 3400 cm^{-1} region, whereas, the peaks at 3396 cm^{-1} and in a broad 3100–3470 cm^{-1} region can be attributed to –OH, stretch [19, 20]. In Figure 2, CA-loaded composites shows a band at 3345 cm^{-1} corresponding to phenolic –OH stretching involving hydrogen bonding, and a peak at 1360 cm^{-1} corresponds to –OH bending of the phenolic group [21].

3.2. Grafting parameters

The results obtained are illustrated as mean values of three replicates in Figure 3, whereas, the standard error of means are shown as Y-error bars in Figure 3. The data revealed the increase in both the graft yield (*GY*%) and graft efficiency (*GE*%) reaching its maximum value at 15 mM CA concentration, then starts to decrease showing that higher concentrations do not promote further grafting. One possible reason for the observed behaviour could be the substantial amount of CA grafted onto the baseline composite, which creates steric hindrance for further grafting. The increase in monomer concentration would be expected to increase both the grafting percentage which in turn increase the molecular weight of the graft composite [22, 23]. The order of *SR*% observed was: 20CA-*g*-P(3HB)-EC > 15CA-*g*-P(3HB)-EC >

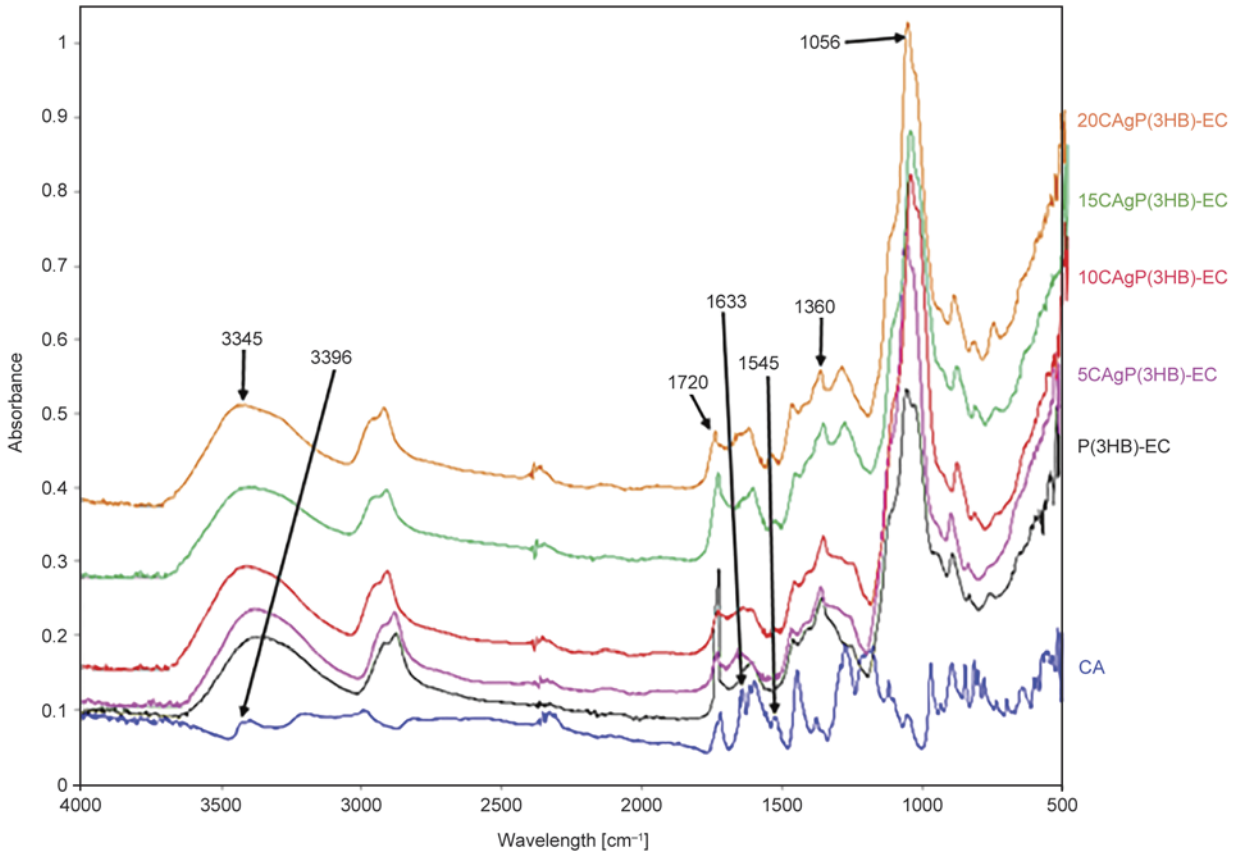

Figure 2. Typical FT-IR spectra of caffeic acid (CA) and CA-*g*-P(3HB)-EC composites prepared using laccase as a model catalyst

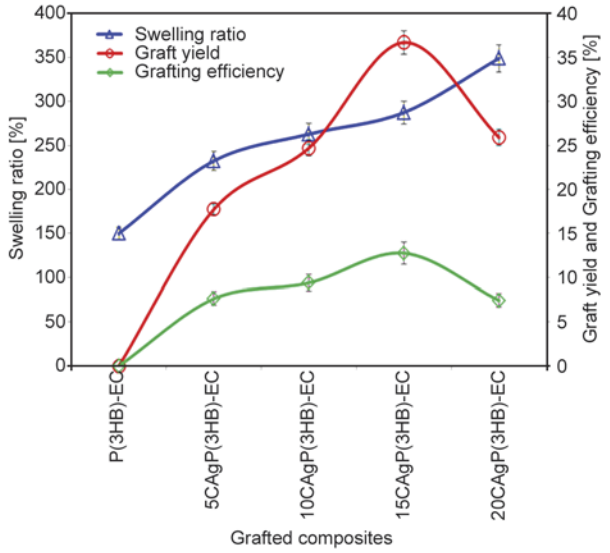

Figure 3. Graft yield (*GY*%), grafting efficiency (*GE*%) and swelling ratio (*SR*%) behaviours of CA-*g*-P(3HB)-EC composites prepared using laccase as a model catalyst

10CA-*g*-P(3HB)-EC > 5CA-*g*-P(3HB)-EC > P(3HB)-EC. It has also been reported in literature that the reaction time is an important parameter which can increase or decrease the grafting parameters like graft yield, grafting efficiency and swelling behaviour [24].

3.3. Testing antibacterial activity

The antibacterial potential of CA-*g*-P(3HB)-EC composites was tested against Gram-positive and Gram-negative strains. As shown in Figure 4a and 4b, after 24 h incubation the remaining bacterial counts decreased with increasing CA content onto the surface of P(3HB)-EC, and this trend was maximum at the concentration of 15 mM CA. A significant antibacterial potential was detected for 15CA-*g*-P(3HB)-EC against Gram-positive strains *i.e.*, *B. subtilis* NCTC 3610 and *S. aureus* NCTC 6571 and the Gram-negative *i.e.*, *E. coli* NTCT 10418 and *P. aeruginosa* NCTC 10662 in comparison to the control sample and relative to other concentrations. However, P(3HB)-EC without any CA concentration was found 100% susceptible against all of the tested micro-organisms. A strong antibacterial potential of 15CA-*g*-P(3HB)-EC was recorded against Gram-negative as compare to the Gram-positive, which is, probably because of the difference between Gram-negative and Gram-positive bacteria in terms of cell structures and antimicrobial mechanism [25, 26].

3.4. *In-vitro* cell viability and adherent morphology

In-vitro biocompatibility evaluation of the grafted composites with HaCaT cell line was analysed using neutral red dye assay and the results obtained are shown in Figure 5. The study demonstrated that when HaCaT cells were seeded onto the composite surfaces after 30 min UV sterilisation, the cells showed high viability after 5 days of incubation, whereas, the

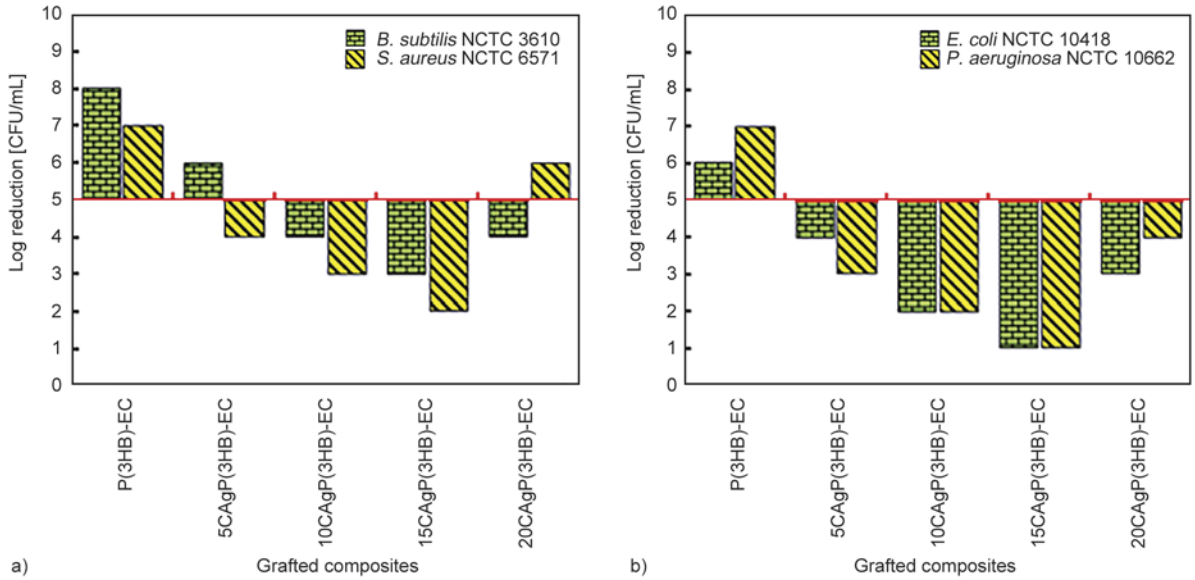

Figure 4. Antimicrobial activity of CA-*g*-P(3HB)-EC composites (a) against Gram-positive strains *i.e.*, *B. subtilis* NCTC 3610 and *S. aureus* NCTC 6571 and (b) against Gram-negative strains *i.e.*, *E. coli* NTCT 10418 and *P. aeruginosa* NCTC 10662

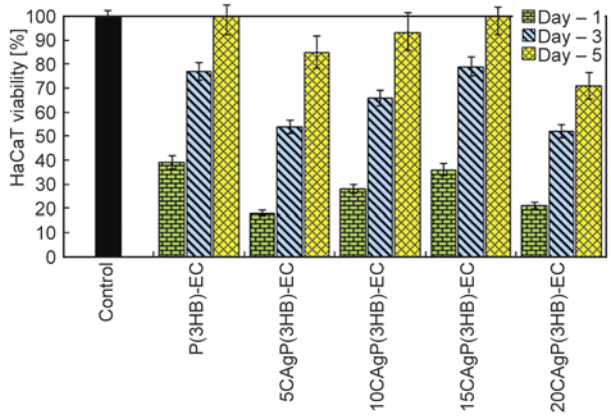

Figure 5. Neutral red dye concentration dependent percentage cell viability of human keratinocytes-like HaCaT cells after 1, 3 and 5 days of incubation onto the CA-*g*-P(3HB)-EC composite surfaces (mean ± SD, $n = 3$)

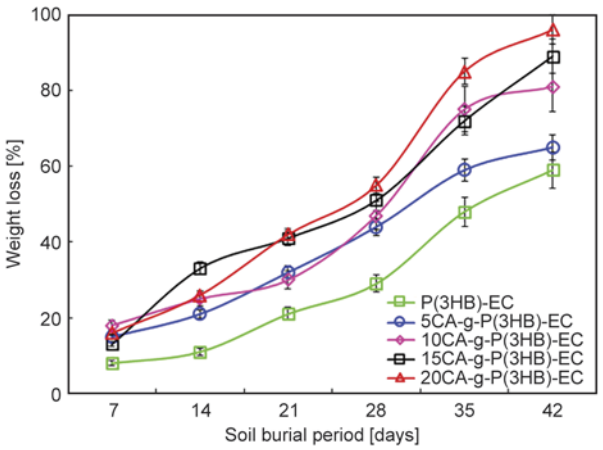

Figure 7. Percentage weight loss of CA-*g*-P(3HB)-EC composites buried for prescribed periods (mean±SD, $n = 3$)

non-toxicity of test samples *i.e.*, P(3HB)-EC, 5CA-*g*-P(3HB)-EC, 10CA-*g*-P(3HB)-EC, 15CA-*g*-P(3HB)-EC and 20CA-*g*-P(3HB)-EC were depicted by the % viability of the HaCaT cells. However, the composite prepared with 20 mM CA concentration and designated as 20CA-*g*-P(3HB)-EC showed a lower % viability of HaCaT cells in comparison with the control and 15CA-*g*-P(3HB)-EC composites after a long contact period (5 days) under the same culturing environment. Additionally, the morphologies of cell cultured on the sterilised surface of 15CA-*g*-P(3HB)-EC composite was higher than those of 20CA-*g*-P(3HB)-EC composite (Figure 6), which is again consistent with the results from viability analyses.

3.5. Biodegradability evaluation

The degradation behaviour of P(3HB)-EC and CA grafted P(3HB)-EC composites has been investigated by measuring the % weight loss of the composites. Figure 7 illustrates the % weight loss of the test composites as a function of degradation time, as represented, all of the composites show an increased degradation rate up to different extent during the buried process which is much likely a result of the moisture (water) penetration into the composites, causing the hydrolysis of surfaces and interfaces [27, 28]. After 6 weeks consecutive exposure, the weight loss of composites reaches 54 wt% for the pristine P(3HB)-EC, 65 wt% for 5CA-*g*-P(3HB)-EC, 81 wt% for 10CA-*g*-P(3HB)-EC, 89 wt% for 15CA-*g*-P(3HB)-EC and 96 wt% for 20CA-*g*-P(3HB)-EC. The degradation profile revealed that the degradability of the CA grafted composites is higher than that of bare P(3HB)-EC. It has been reported in literature that during soil burial the polymer molecular chains degrade which followed by their transformation into water and CO_2 after a long term degradation, thus, it seems that the soil burial degradation mechanism involves a recyclable, green, and environmentally friendly process to fully degrade the biodegradable polymeric composites [29].

4. Conclusions

It could be concluded from the data discussed above, the newly developed novel composites could well represent the new wave of biomaterials for medical application, to be used to treat specific infections rather than the broad spectrum which can cause significant morbidity as a consequence of their lack of specificity. The improved resistance against a wide spectrum of microbes as well as HaCaT compatibility all indicates that CA-*g*-P(3HB)-EC could be potential candidates for biomedical applications particularly in the area of infection free wound healing. Undoubtedly, the results obtained, herein, after soil burial degradation revealed that CA-*g*-P(3HB)-EC composites will not cause any deleterious ecological impact.

Acknowledgements

The authors thankfully acknowledge the financial support and laboratory facilities from the University of Westminster under Cavendish Research Scholarship program.

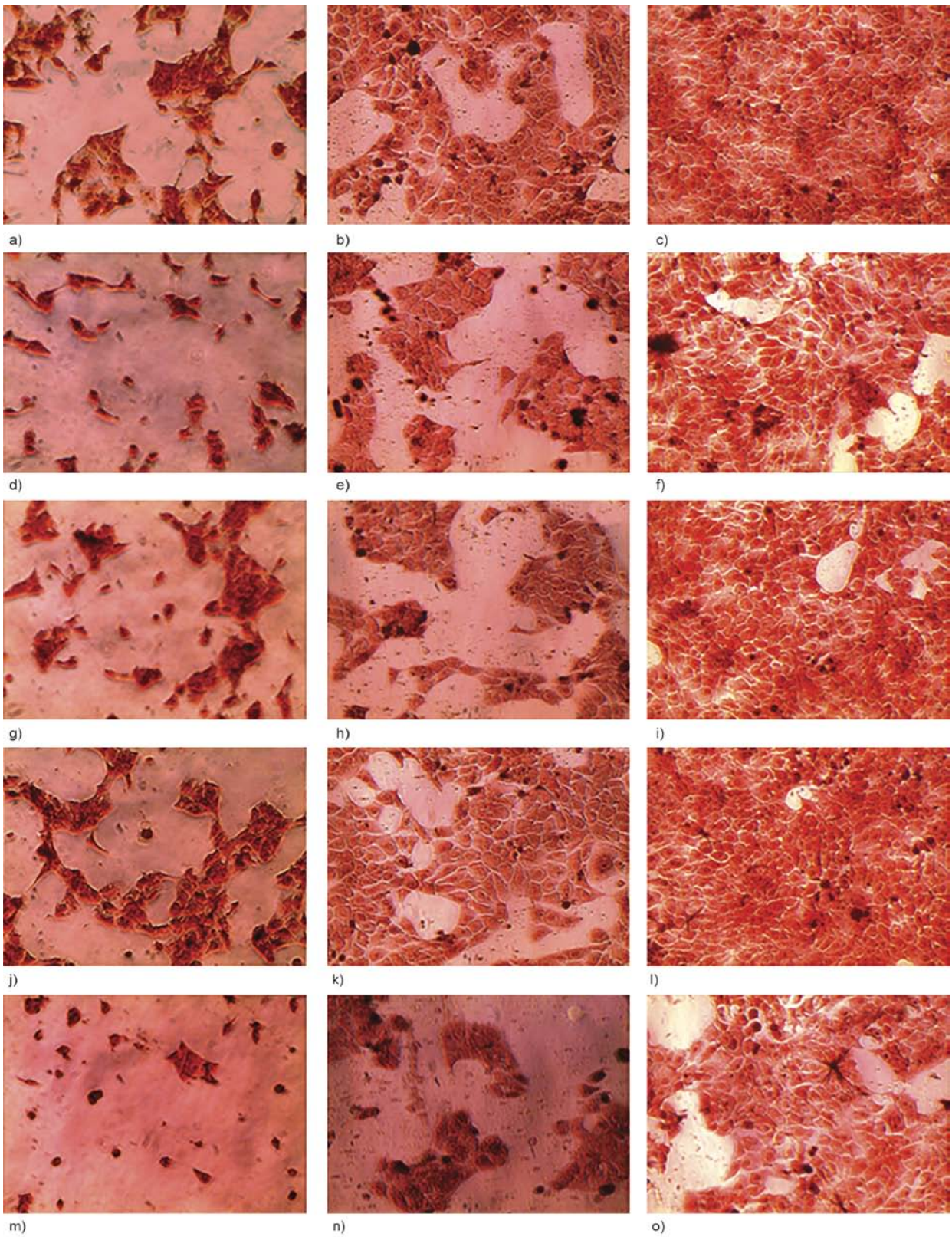

Figure 6. Adherent morphology of HaCaT cells seeded onto the composite surfaces. Images (a), (b) and (c) represent the HaCaT cells on native P(3HB)-EC composite (*i.e.*, P(3HB)-EC) after 1, 3 and 5 days of incubation, respectively; images (d), (e) and (f) represent the HaCaT cells on 5CA-*g*-P(3HB)-EC composite after 1, 3 and 5 days of incubation, respectively; images (g), (h) and (i) represent the HaCaT cells on 10CA-*g*-P(3HB)-EC composite after 1, 3 and 5 days of incubation, respectively; images (j), (k) and (l) represent the HaCaT cells on 15CA-*g*-P(3HB)-EC composite after 1, 3 and 5 days of incubation, respectively and images (m), (n) and (o) represent the HaCaT cells on 20CA-*g*-P(3HB)-EC composite after 1, 3 and 5 days of incubation, respectively. All images were taken at 100× magnification.

References

[1] Satyanarayana K. G., Arizaga G. G. C., Wypych F.: Biodegradable composites based on lignocellulosic fibers – An overview. Progress in Polymer Science, **34**, 982–1021 (2009).
DOI: 10.1016/j.progpolymsci.2008.12.002

[2] Iqbal H. M. N., Kyazze G., Tron T., Keshavarz T.: A preliminary study on the development and characterisation of enzymatically grafted P(3HB)-ethyl cellulose based novel composites. Cellulose, **21**, 3613–3621 (2014).
DOI: 10.1007/s10570-014-0337-9

[3] Iqbal H. M. N., Kyazze G., Tron T., Keshavarz T.: Laccase-assisted approach to graft multifunctional materials of interest: Keratin-EC based novel composites and their characterisation. Macromolecular Materials and Engineering, in press (2015).
DOI: 10.1002/mame.201500003

[4] Iqbal H. M. N., Kyazze G., Tron T., Keshavarz T.: Laccase-assisted grafting of poly(3-hydroxybutyrate) onto the bacterial cellulose as backbone polymer: Development and characterisation. Carbohydrate Polymers, **113**, 131–137 (2014).
DOI: 10.1016/j.carbpol.2014.07.003

[5] Fillat A., Gallardo O., Vidal T., Pastor F. I. J., Díaz P., Roncero M. B.: Enzymatic grafting of natural phenols to flax fibres: Development of antimicrobial properties. Carbohydrate Polymers, **87**, 146–152 (2012).
DOI: 10.1016/j.carbpol.2011.07.030

[6] Chang K. C., Chuang T. L., Ji W. F., Chang C. H., Peng Y. Y., Shih H., Hsu L. C., Yeh J. M., Tang W. C., Su Y. C.: UV-curable nanocasting technique to prepare bioinspired superhydrophobic organic-inorganic composite anticorrosion coatings. Express Polymer Letters, **9**, 143–153 (2015).
DOI: 10.3144/expresspolymlett.2015.15

[7] Iqbal H. M. N., Kyazze G., Tron T., Keshavarz T.: 'One-pot' synthesis and characterisation of novel P(3HB)–ethyl cellulose based graft composites through lipase catalysed esterification. Polymer Chemistry, **5**, 7004–7012 (2014).
DOI: 10.1039/C4PY00857J

[8] Maiti S., Khatua B. B.: Polyaniline integrated carbon nanohorn: A superior electrode materials for advanced energy storage. Express Polymer Letters, **8**, 895–907 (2014).
DOI: 10.3144/expresspolymlett.2014.91

[9] Aracri E., Fillat A., Colom J. F., Gutiérrez A., del Río J. C., Martínez Á. T., Vidal T.: Enzymatic grafting of simple phenols on flax and sisal pulp fibres using laccases. Bioresource Technology, **101**, 8211–8216 (2010).
DOI: 10.1016/j.biortech.2010.05.080

[10] Cadena E. M., Du X., Gellerstedt G., Li J., Fillat A., García-Ubasart J., Vidal T., Colom J. F.: On hexenuronic acid (HexA) removal and mediator coupling to pulp fiber in the laccase/mediator treatment. Bioresource Technology, **102**, 3911–3917 (2011).
DOI: 10.1016/j.biortech.2010.11.127

[11] Elegir G., Kindl A., Sadocco P., Orlandi M.: Development of antimicrobial cellulose packaging through laccase-mediated grafting of phenolic compounds. Enzyme and Microbial Technology, **43**, 84–92 (2008).
DOI: 10.1016/j.enzmictec.2007.10.003

[12] Wong K. K. Y., Richardson J. D., Mansfield S. D.: Enzymatic treatment of mechanical pulp fibers for improving papermaking properties. Biotechnology Progress, **16**, 1025–1029 (2000).
DOI: 10.1021/bp000064d

[13] Felby C., Hassingboe J., Lund M.: Pilot-scale production of fiberboards made by laccase oxidized wood fibers: Board properties and evidence for cross-linking of lignin. Enzyme and Microbial Technology, **31**, 736–741 (2002).
DOI: 10.1016/S0141-0229(02)00111-4

[14] Kalemba D., Kunicka A.: Antibacterial and antifungal properties of essential oils. Current Medicinal Chemistry, **10**, 813–829 (2003).
DOI: 10.2174/0929867033457719

[15] Yu Q., Wu Z., Chen H.: Dual-function antibacterial surfaces for biomedical applications. Acta Biomaterialia, **16**, 1–13 (2015).
DOI: 10.1016/j.actbio.2015.01.018

[16] Akaraonye E., Keshavarz T., Roy I.: Production of polyhydroxyalkanoates: the future green materials of choice. Journal of Chemical Technology and Biotechnology, **85**, 732–743 (2010).
DOI: 10.1002/jctb.2392

[17] Rai R., Yunos D. M., Boccaccini A. R., Knowles J. C., Barker I. A., Howdle S. M., Tredwell G. D., Keshavarz T., Roy I.: Poly-3-hydroxyoctanoate P(3HO), a medium chain length polyhydroxyalkanoate homopolymer from *Pseudomonas mendocina*. Biomacromolecules, **12**, 2126–2136 (2011).
DOI: 10.1021/bm2001999

[18] Wattanakornsiri A., Pachana K., Kaewpirom S., Traina M., Migliaresi C.: Preparation and properties of green composites based on tapioca starch and differently recycled paper cellulose fibers. Journal of Polymers and the Environment, **20**, 801–809 (2012).
DOI: 10.1007/s10924-012-0494-6

[19] Shahidi S., Rashidi A., Ghoranneviss M., Anvari A., Rahimi M. K., Bameni Moghaddam M., Wiener J.: Investigation of metal absorption and antibacterial activity on cotton fabric modified by low temperature plasma. Cellulose, **17**, 627–634 (2010).
DOI: 10.1007/s10570-010-9400-3

[20] Shahidi S., Aslan N., Ghoranneviss M., Korachi M.: Effect of thymol on the antibacterial efficiency of plasma-treated cotton fabric. Cellulose, **21**, 1933–1943 (2014).
DOI: 10.1007/s10570-014-0250-2

[21] Rukmani A., Sundrarajan M.: Inclusion of antibacterial agent thymol on β-cyclodextrin-grafted organic cotton. Journal of Industrial Textiles, **42**, 132–144 (2012).
DOI: 10.1177/1528083711430244

[22] Aggour Y. A.: Reaction kinetics of graft copolymerization and thermochemical studies of the degradation of poly(vinyl alcohol) graft copolymer. Polymer International, **50**, 347–353 (2001).
DOI: 10.1002/pi.635

[23] Constantin M., Mihalcea I., Oanea I., Harabagiu V., Fundueanu G.: Studies on graft copolymerization of 3-acrylamidopropyl trimethylammonium chloride on pullulan. Carbohydrate Polymers, **84**, 926–932 (2011).
DOI: 10.1016/j.carbpol.2010.12.043

[24] Sun T., Xu P., Liu Q., Xue J., Xie W.: Graft copolymerization of methacrylic acid onto carboxymethyl chitosan. European Polymer Journal, **39**, 189–192 (2003).
DOI: 10.1016/S0014-3057(02)00174-X

[25] Li S-M., Jia N., Ma M-G., Zhang Z., Liu Q-H., Sun R-C.: Cellulose–silver nanocomposites: Microwave-assisted synthesis, characterization, their thermal stability, and antimicrobial property. Carbohydrate Polymers, **86**, 441–447 (2011).
DOI: 10.1016/j.carbpol.2011.04.060

[26] Dong C., Ye Y., Qian L., Zhao G., He B., Xiao H.: Antibacterial modification of cellulose fibers by grafting β-cyclodextrin and inclusion with ciprofloxacin. Cellulose, **21**, 1921–1932 (2014).
DOI: 10.1007/s10570-014-0249-8

[27] Vieira A. C., Vieira J. C., Ferra J. M., Magalhães F. D., Guedes R. M., Marques A. T.: Mechanical study of PLA–PCL fibers during *in vitro* degradation. Journal of the Mechanical Behavior of Biomedical Materials, **4**, 451–460 (2011).
DOI: 10.1016/j.jmbbm.2010.12.006

[28] Tham W. L., Ishak Z. M., Chow W. S.: Water absorption and hygrothermal aging behaviors of sebs-g-mah toughened poly(lactic acid)/halloysite nanocomposites. Polymer-Plastics Technology and Engineering, **53**, 472–480 (2014).
DOI: 10.1080/03602559.2013.845208

[29] Alam A. K. M. M., Beg M. D. H., Mina M. F., Mamun A. A., Bledzki A. K.: Degradation and stability of green composites fabricated from oil palm empty fruit bunch fiber and polylactic acid: Effect of fiber length. Journal of Composite Materials, in press (2014).
DOI: 10.1177/0021998314560219

eXPRESS Polymer Letters Vol.9, No.9 (2015) 773–789
Available online at www.expresspolymlett.com
DOI: 10.3144/expresspolymlett.2015.73

Novel poly(butylene succinate) nanocomposites containing strontium hydroxyapatite nanorods with enhanced osteoconductivity for tissue engineering applications

M. Nerantzaki[1], M. Filippousi[2], G. Van Tendeloo[2], Z. Terzopoulou[1], D. Bikiaris[1], O. M. Goudouri[3], R. Detsch[3], A. Grüenewald[3], A. R. Boccaccini[3]*

[1]Aristotle University of Thessaloniki, GR-541 24 Thessaloniki, Macedonia, Greece
[2]EMAT, University of Antwerp, Groenenborgerlaan 171, B-2020 Antwerp, Belgium
[3]Institute of Biomaterials, Department of Materials Science and Engineering, University of Erlangen-Nuremberg, Cauerstrasse 6, 91058 Erlangen, Germany

Received 31 January 2015; accepted in revised form 6 April 2015

Abstract. Three series of poly(butylene succinate) (PBSu) nanocomposites containing 0.5, 1 and 2.5 wt% strontium hydroxyapatite [$Sr_5(PO_4)_3OH$] nanorods (SrHAp nrds) were prepared by *in situ* polymerisation. The structural effects of $Sr_5(PO_4)_3OH$ nanorods, for the different concentrations, inside the polymeric matrix (PBSu), were studied through high angle annular dark field scanning transmission electron microscopy (HAADF-STEM). HAADF-STEM measurements revealed that the SrHAp nanorods at low concentrations are dispersed inside the polymeric PBSu matrix while in 1 wt% some aggregates are formed. These aggregations affect the mechanical properties giving an enhancement for the concentration of 0.5 wt% SrHAp nrds in tensile strength, while a reduction is recorded for higher loadings of the nanofiller. Studies on enzymatic hydrolysis revealed that all nanocomposites present higher hydrolysis rates than neat PBSu, indicating that nanorods accelerate the hydrolysis degradation process. *In vitro* bioactivity tests prove that SrHAp nrds promote the formation of hydroxyapatite on the PBSu surface. All nanocomposites were tested also in relevant cell culture using osteoblast-like cells (MG-63) to demonstrate their biocompatibility showing SrHAp nanorods support cell attachment.

Keywords: *nanocomposites, poly(butylene succinate), strontium nanorods, scaffolds*

1. Introduction

Polymers are versatile materials and are used in many applications including biomedical applications because of their biocompatibility and to their modifiable properties [1, 2]. Biodegradable aliphatic polyesters can be prepared to provide a wide range of degradation rates and mechanical properties [3]. Especially those belonging to the family of poly(lactic acid) (PLA) and poly(glycolic acid) (PGA), play an increasingly important role in the fledgling field of tissue engineering because they can be fashioned into porous scaffolds or carriers of cells, extracellular matrix components, and bioactive agents [4]. Poly (butylene succinate) (PBSu) is also a type of biodegradable aliphatic polyester, which can be efficiently synthesized from the starting materials of succinic acid and butan-1,4-diol. When compared with PLA and PGA, PBSu has better processability and mechanical properties similar to those of polyethylene and polypropylene [5]. Biocompatibility and osteoconductive properties of PBSu have also been shown by its ability to allow cellular adhesion and proliferation both *in vitro* and *in vivo* [6, 7].

*Corresponding author, e-mail: dbic@chem.auth.gr

Moreover research has shown that all living systems are governed by molecular behaviour at nanoscale. Nanometer structural components are thus being considered as promising biomaterials [8]. Studies in the literature have shown significant increases in bone cell functions when nanophase (compared to conventional) ceramic particles are incorporated into polymer composites. Specifically, up to three times more osteoblasts adhered to PLGA when it contained nanophase particles compared to conventional titania at the same weight ratio and porosity. Moreover, significantly greater *in vitro* osteoblast functions leading to mineral deposition were observed on carbon fibers with nanometer size compared to conventional dimensions [8]. These results suggest that the proactive surface roughness of nanophase materials may be transferable to polymers to promote orthopedic implant efficacy.

In order to promote tissue regeneration and to modulate cellular function, researchers have also focused on the challenge of designing bone tissue engineering scaffolds that mimic the unique mechanical properties of bone. Nanophase reinforcement has the potential of improving current materials to achieve mechanical strength comparable to the native tissue. Recently, carbon nanotubes and alumoxane nanoparticles have been examined as reinforcing fillers for biodegradable polymers. The effect of a filler on the mechanical properties depends on the size, shape, and dispersion of the filler. Furthermore, the interaction between the filler and the organic matrix can also impact the level of reinforcement. Therefore, optimal performance is achieved when the small particles are uniformly dispersed throughout the polymer and interact strongly with the organic matrix.

Recently, PBSu nanocomposites containing SiO_2 nanotubes and SrHAp nanorods at relatively high concentrations 5 and 20 wt% were prepared by melt mixing and studied as potential materials for tissue engineering applications [9]. Concerning of Sr-substituted hydroxyapatite SrHAp nrds could stimulate osteoblasts proliferation *in vitro* and provide an ideal environment for colonization, proliferation, and differentiation of osteoblasts to form new bone *in vivo*, due to its numerous phosphate groups, which could have a positive effect on cell growth. The results confirmed SiO_2 nanotubes to support cell attachment and growth. However, the presence of strontium led to cytotoxicity of the nanocomposites, which might be related to critical concentration of Sr being released from the composite material.

The aim of the present study is the preparation and study of PBSu nanocomposites with optimized strontium hydroxyapatite nanorods' concentrations for tissue engineering applications. As an alternative development method *in situ* polymerization will be used, in order to achieve a more uniform dispersion of the nanofillers in the polymer matrix and thus improve the physical properties. Compared with the method of melt mixing, *in situ* polymerization gives more satisfactory dispersion of nanoparticles and stronger interactions between the reinforcements and the polymeric phase. Therefore, nanocomposites fabricated by *in situ* processing tend to display better mechanical properties and a lower percolation threshold than those composites made by ex situ methods.

2. Experimental

2.1. Materials

Succinic acid (CAS Number: 110-15-6) (purum 99+%), 1,4-butanediol (110-63-4) (purity >99%) and titanium (IV) butoxide (TBT) (5593-70-4) (>97%) were obtained from Sigma-Aldrich Chemical Co (Chemie GmbH, Germany) and used as received. Strontium nitrate [$Sr(NO_3)_2$] (10042-76-9) (≥99%), ammonium phosphate dibasic [$(NH_4)_2HPO_4$] (7783-28-0) (≥98%) and trisodium citrate dehydrate (labelled as Cit^{3-}) (6132-04-3) (≥99%) were supplied from Sigma Aldrich Chemical Co (Chemie GmbH, Germany). Cetyltrimethyl-ammonium bromide (57-09-0) (labelled as CTAB) (≥99%) was purchased from Panreac Quimicha (Panreac Quimica S.L.U., Spain). All other materials and solvents used in the analytical methods were of analytical grade.

2.2. Synthesis of strontium hydroxyapatite nanorods

Strontium hydroxyapatite nanorods were synthesized via the hydrothermal method that Zhang *et al*. [10] previously described. In a typical procedure, 3 mmol of $Sr(NO_3)_2$, 0.5 g of CTAB, and 10 mL of ammonia solution ($NH_3 \cdot H_2O$) (used for adjusting the pH value as alkaline solution) were dissolved in 30 mL of deionized water to form solution 1. Then, 6 mmol of trisodium citrate (labeled as Cit^{3-}, the molar ratio of Cit^{3-}/Sr^{2-} is 2:1) and 2 mmol of $(NH_4)_2HPO_4$ were added into 20 mL H_2O to form solution 2. After vigorously stirring for 30 min, solu-

tion 2 was introduced into solution 1 (dropwise). After additional agitation for 20 min, the as-obtained mixing solution was transferred into a Teflon bottle (80 mL) held in a stainless steel autoclave, sealed, and maintained at 180°C for 24 h. As the autoclave cooled to room temperature naturally, the precipitate was separated by centrifugation, washed with deionized water and ethanol in sequence. Then, the obtained product was redispersed in 150 mL of acetone and refluxed at 80°C for 48 h to remove the residual template CTAB. Finally, the precipitate was separated by centrifugation again and dried in vacuum at 70°C for 24 h to obtain the final sample [10].

2.3. *In situ* prepared nanocomposites

Nanocomposites of PBSu and SrHAp nanorods were prepared *in situ* by the two-stage melt polycondensation method using succinic acid (SA) and 1,4-butanediol (BD) in a glass batch reactor at a molar ratio SA:BD of 1:1.15. Appropriate amount of SrHAp nrds was first dispersed in 1,4-butanediol by ultrasonic vibration (50 W, Hielscher UP50H) and intense stirring with a magnetic stirrer (300 rpm) for 10 min prior to polymerization. The polymerization mixture, after being placed in a 250 cm^3 round bottom flask, was de-aired and purged with dry nitrogen three times. Thereupon, the mixture was heated under a nitrogen atmosphere for 3.5 h at 200°C under constant stirring (350 rpm), with water removed as the reaction by-product of esterification. Afterwards, for the second reaction stage of polycondensation, 0.3 wt% of TPP as heat stabilizer and $1.0 \cdot 10^{-3}$ mol per mole of succinic acid of TBT as polycondensation catalyst were added. The reaction was continued under increased mechanical stirring (720 rpm) and high vacuum (~5.0 Pa), which was applied slowly over a period of time of about 30 min, to avoid excessive foaming and to minimize oligomer sublimation, at 220 and 240°C for 1 h intervals, respectively. Polymerization was stopped by fast cooling to room temperature. After the polycondensation reaction was completed, the polyesters were easily removed from the flask. According to this procedure neat PBSu and nanocomposites containing 0.5, 1 and 2.5 wt% SrHAp nrds have been prepared.

2.4. Nanocomposites characterization

2.4.1. Gel permeation chromatography (GPC)

GPC analysis was performed using a Waters 150C GPC (Waters Corp., Milford, MA) equipped with a differential refractometer as detector and three ultrastyragel (103, 104, 105E) columns in series. $CHCl_3$ was used as the eluent (1 mL/min) and the measurements were performed at 35°C. Calibration was performed using polystyrene standards with a narrow molecular weight distribution.

2.4.2. Fourier Transformed-Infrared Spectroscopy (FTIR)

FTIR spectra were obtained using a Perkin–Elmer FTIR (Perkin–Elmer Inc. USA) spectrometer, model Spectrum One. The materials were in the form of thin films with a thickness of approximately 30 μm. The IR spectra of these films were obtained in absorbance mode and in the spectral region of 400–4000 cm^{-1} using a resolution of 4 cm^{-1} and 64 co-added scans.

2.4.3. X-ray photoelectron spectroscopy (XPS)

The element composition and interfacial interactions were studied using X-ray photoelectron spectroscopy (XPS). In the XPS analysis (AXIS Ultra 'DLD' X-ray photoelectron spectrometer) (Shimadzu Corp., Japan), a monochromatic Al Ka X-ray was used at 14 kV. A binding energy of 284.8 eV for the C 1s of aliphatic carbons was taken as the reference energy. The XPS curve fitting of C 1s, O 1s and Sr3d were accomplished using Kratos' Vision 2 Processing software.

2.4.4. Scanning electron microscopy (SEM)

The morphology of the prepared nanocomposites was examined using a scanning electron microscopy system (SEM) type JEOL (JMS-840) (Jeol Ltd., Tokyo) equipped with an energy-dispersive X-ray (EDX) Oxford ISIS 300 micro-analytical system (Oxford Instruments UK). The studied surfaces were coated with carbon black in order to obtain good conductivity for the electron beam. Operating conditions were: accelerating voltage 20 kV, probe current 45 nA and counting time 60 s.

2.4.5. High angle annular dark field scanning transmission electron microscopy

Samples suitable for HAADF-STEM measurements were sectioned using a Leica UC7 ultramicrotome equipped with a FC7 cryo chamber and the sections had a thickness of 100–120 nm. The sections were placed on Quantifoil C coated Cu grids. Samples were cut at –80°C. HAADF-STEM images were

acquired using a FEI Tecnai G2 electron microscope operated at 200 kV.

2.4.6. X-ray Diffractometry (WAXD)

XRD studies of nanocomposites, in the form of thin films, were performed over the range 2 h from 5 to 80°, at steps of 0.05° and counting time of 5 s, using a MiniFlex II XRD system from (RIGAKU Co., Ltd., Japan). The degree of crystallinity was measured using instrument's software.

2.4.7. Mechanical properties

Measurements of mechanical properties of the prepared nanocomposites in tension were performed on an Instron 3344 dynamometer (Instron, USA) in accordance with ASTM D638, using a crosshead speed of 5 mm/min. Relative thin sheets of about 350±25 μm were prepared using an Otto Weber, Type PW 30 hydraulic press connected with an Omron E5AX Temperature Controller, at a temperature of 130±5°C. The moulds were rapidly cooled by immersing them in water at 20°C In order to measure the mechanical properties from these sheets, dumb-bell-shaped tensile test specimens (central portions 5×0.5 mm thick, 22 mm gauge length) were cut in a Wallace cutting press and conditioned at 25°C and 55–60% relative humidity for 48 h. The values of Young's modulus, yield stress, elongation at break and tensile strength at the break point were determined. At least five specimens were tested for each sample and the average values are reported.

2.4.8. Dynamic mechanical analysis (DMA)

The dynamic mechanical properties of the nanocomposites were measured with a Perkin-Elmer Diamond DMA (PerkinElmer, Inc. USA). The bending (dual cantilever) method was used with a frequency of 1 Hz, a strain level of 0.04%, in the temperature range of –70.0 to 80.0°C. The heating rate was 3°C/min^{-1}. Testing was performed using rectangular bars measuring approximately 30×10×3.0 mm^3. These were prepared with a hydraulic press, as described above, and the exact dimensions of each sample were measured before the scan.

2.4.9. Contact angle measurements

Contact angle measurements, before and after sterilization, were performed using a DSA30 analyzer, (KRUSS GmbH, Germany). The samples were in the form of thin films of 500±50 μm thickness and 0.5 cm diameter. The drop of water used had a diameter of 3 μm.

2.4.10. Enzymatic hydrolysis

Samples in the form of films (10×20×0.4 mm^3) prepared using an Otto Weber Type PW 30 hydraulic press at 130°C, were placed in test tubes, wherein 5 mL of phosphate buffer solution (0.2 M, pH 7.0) was added, containing *Rhizopus delemar* ≥0.4 U/mg and *Pseudomonas Cepacia* ≥30 U/mg lipase. The concentrations of the lipases were 0.09 and 0.01 mg/mL, respectively, because 0.1 mg/mL total enzyme concentration in PBS is sufficient to cause notable mass loss over a period of 40 days of enzymatic treatment at 37°C. The loosely capped test tubes were kept at 37.0±1.0°C in an oven for several days while the media were replaced every 3 days. After a predetermined time the films were removed from the lipase solution, washed thoroughly with distilled water and ethanol and then dried at room temperature under vacuum, until constant weight. Every measurement was repeated three times. As a control, the same experiment was carried out under the same conditions without any lipase being added. The degree of biodegradation was estimated from the mass loss. The morphology of the prepared films during enzymatic hydrolysis was examined through scanning electron micrographs (SEM).

2.4.11. Formation of bone-like apatite

After ultrasonic cleaning in acetone and rinsing with distilled water, all the samples were soaked in a simulated body fluid (SBF) for 14 and 28 days in order to assess their bioactivity. The ionic concentrations in the SBF solution are nearly equal to those in human body blood plasma, and the solution was buffered at pH 7.4 with trimethanol aminomethane-HCL. After the immersion test, each specimen was gently washed with distilled water, gradually dried with ethanol. Finally, the specimens were observed by scanning electron microscopy.

2.4.12. Cell culture studies

The *in vitro* biocompatibility of all materials was evaluated in contact with MG63 osteoblast-like cells after 48 h of incubation. Six samples from each category were disinfected by immersion in 70 vol% ethanol solution for 1 h. After disinfection the samples were washed with phosphate-buffered saline (PBS, Gibco®) and were placed into a single well of

a 24-well plate (Corning, Cambridge, MA). 1.5 mL of Dulbecco's Modified Eagle's medium (DMEM, Gibco, Germany) supplemented with 10 vol% fetal bovine serum (FBS, Sigma-Aldrich, Germany) and 1 vol% penicillin and streptomycin (Gibco, Germany) containing 10^5 cells was added to each well. The same amount of culture medium with cells without specimens was used as positive control. All samples and controls were incubated at 37°C in a humidified atmosphere (5% CO_2 in 95% air, SteriCycle, Thermo Fisher Scientific) for 48 hours. Afterwards, the samples were washed with PBS and 1 mL of AlamarBlue solution was added in the well plate. The well plate was incubated at 37°C (95% humidity, 5% CO_2) for 4 hours. The AlamarBlue solution was prepared by mixing 10 vol% of Alamar Blue reagent (Invitrogen, Germany) with DMEM supplemented with FCS and antibiotics as previously described. After 4 hours of incubation, the optical density of the solutions was measured at 570 and 600 nm with a plate reader (Anthos, Germany). Cell morphologies were obtained by SEM microscopy (Quanta 200, FEI, The Netherlands). All samples were washed with PBS, fixed with a solution containing 3 vol% glutaraldehyde (Sigma, Germany) and 3 vol % paraformaldehyde (Sigma, Germany) in 0.2 M sodium cacodylate buffer (pH 7.4) and finally rinsed three times with PBS. Consequently, all samples were dehydrated in a graded ethanol series (30, 50, 70, 80, 90, 95, and 99.8 vol%). Samples were maintained in 99.8 vol% ethanol and critical-point dried (EM CPD300, Leica, Germany) before imaging with SEM.

3. Results and discussion

3.1. Synthesis and characterization of *in situ* prepared PBSu/SrHAp nrds nanocomposites

PBSu nanocomposites were synthesized by two-step reactions of esterification and polycondensation. According to this procedure polyesters with high molecular weight can be prepared and the M_n and M_w values of neat PBSu are calculated at 40 850 and 92 220 g/mol, respectively, which is quite satisfactory for aliphatic polyesters [11]. The presence of the nanorods in the polymerization mixture, affected the reaction, leading to variations of the final molecular weight of the synthesized polymers. As shown in Table 1, the average molecular weight of the nanocomposites varies. Initially the molecular weight was increased for a SrHAp nanorod concentration of 0.5 wt%, followed by a gradual decrease at higher concentrations. This is due to the interactions that probably are taking place between nanorods and PBSu macromolecules, since SrHAp nanorods have a lot of hydroxyl groups that could react with the –COOH or –OH end groups of PBSu macromolecules.

Table 1. Molecular weight of prepared nanocomposites

Sample	M_n [g/mol]	M_w [g/mol]	M_w/M_n
PBSu	40 850	92 220	2.3
PBSu/SrHAp nrds 0.5 wt%	51 100	122 950	2.4
PBSu/SrHAp nrds 1.0 wt%	37 790	83 380	2.2
PBSu/SrHAp nrds 2.5 wt%	21 550	41 010	1.9

Due to these interactions at a low concentration the nanoparticles could act as chain extenders, increasing the molecular weight of the polyester, and thus macromolecules with higher molecular weight than pure polyester were produced, as in the nanocomposite containing 0.5 wt% SrHAp nrds. However, at higher concentrations, due to extended reactions, branched and/or cross-linked macromolecules could be formed, since SrHAp nrds, due to the surface hydroxyl groups, can act as a multifunctional agent, leading to a partial reduction of molecular weight [12], as in nanocomposites containing 1.0 and 2.5 wt% SrHAp nanorods. Branched polymers generally have lower intrinsic viscosities than the corresponding linear ones having the same molecular weight. This happens due to the hydrodynamic dimensions of branched macromolecules, which is what the methods used for the determination of the molecular weight actually measure, are smaller in solution than linear ones. Similar reactions were mentioned in PBSu/silica nanocomposites and it was revealed that silanol groups (Si–OH) in SiO_2 nanoparticles could react with the hydroxyl end groups of the polyesters. Such a reaction was verified using results from solid-state ^{29}Si NMR and FTIR spectra of PBSu/silica nanocomposites, indicating covalent bonding between SiO_2 particles and the PBSu macromolecular chain [13–15].

In the present study FTIR and XPS were used to examine the possibility of such reactions to take place between Sr–OH groups of SrHAp nanorods and PBSu. As shown in Figure 1 for the neat PBSu sample, the characteristic ester absorption peak for the stretching vibration of the –C=O bond appears at 1717 cm^{-1}. The peak at 2960 cm^{-1} is attributed to

the stretching vibration of C-H of the –CH2- group while the wide peak at 3100-3700 cm^{-1} corresponds to hydroxyl groups of the polyester. For the PBSu nanocomposites, the infrared spectra retained most of the band of PBSu, although some of them changed in intensity. Thus, it seems that no interactions between inorganic nanoparticles and PBSu matrix took place and covalently bonds between PBSu and SrHAp nanorods have not been formed. However, there is also the possibility due to the low amount of added SrHAp nanorods, these interactions could not be detected with FTIR, due to its low sensitivity.

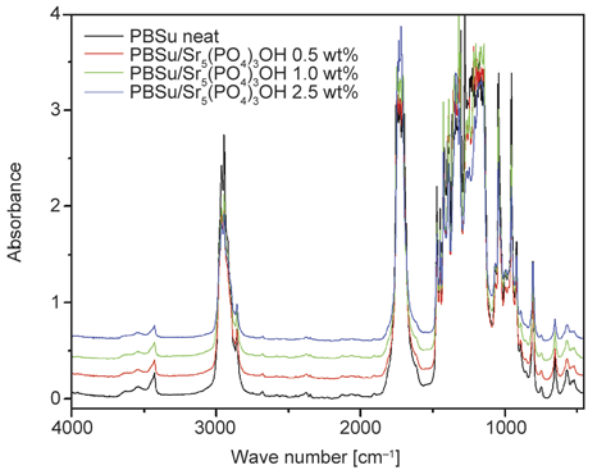

Figure 1. FTIR spectra of prepared nanocomposites

In order to investigate the possible covalent bonding between SrHAp nanorods and the PBSu polymer backbone chain, XPS analysis was performed. Neat PBSu has characteristic peaks at the regions C 1s and O 1s with binding energies 283–292 and 529–536 eV, respectively (Figure 2). Both peaks can be further analyzed to different binding energies corresponding to different carbonyl components like C_1 = CC and CH (284.52 eV), C_2 = bC to ester (285.32 eV), C_3 = C–O (286.52 eV), C_4 =ester (C=O)–O (288.72 eV) (Figure 2) and oxygen like O_1 = ester(C=O)–O (532.01 eV), O_2 = carbonyl (C=O) (533.38 eV) and O_3 carboxylic (O=C)–OH (535,42 eV) (Figure 3) [16]. XPS study was performed for all the nanocomposites, but for the samples with PBSu/SrHAp nrds 0.5 wt% and PBSu/SrHAp nrds 1.0 wt% the presence of the nanofiller was not confirmed. XPS analysis is a surface-sensi-

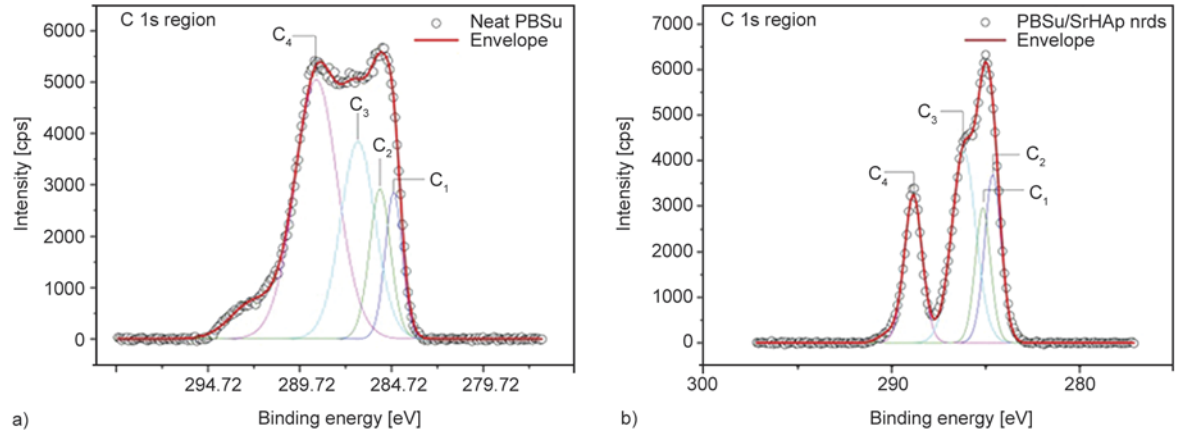

Figure 2. XPS spectra of a) PBSu and b) PBSu/SrHAp 2.5 wt% nrds in C 1s region

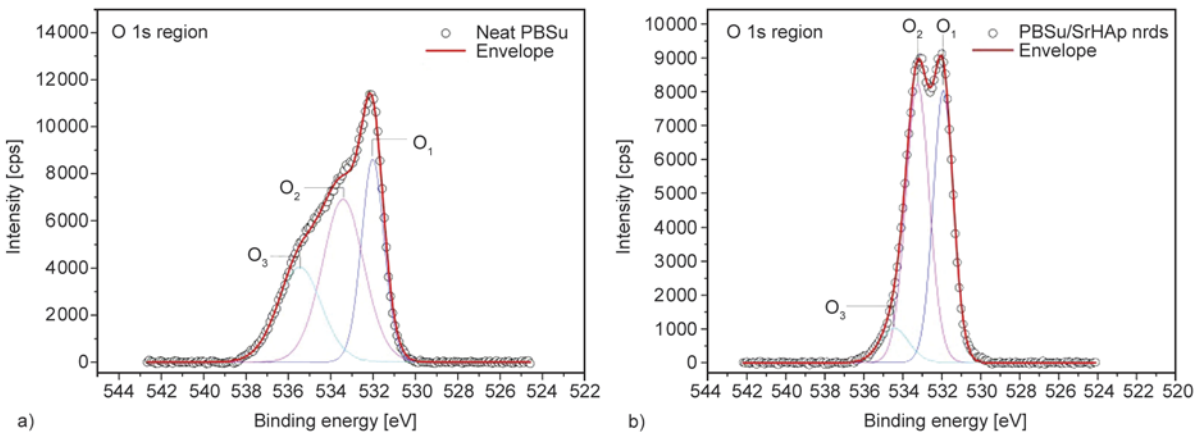

Figure 3. XPS spectra of a) PBSu and b) PBSu/SrHAp nrds 2.5 wt% in O 1s region

Table 2. Characteristic binding energies of carbonyl and oxygen components in PBSu and PBSu/SrHAp nrds 2.5 wt% nanocomposite

Component	Peak position [eV]	
	NeatPBSu	PBSu/SrHAp nrds
C_1	284.52	284.6
C_2	285.32	285.09
C_3	286.52	286.17
C_4	288.72	288.76
O_1	532.01	531.92
O_2	533.38	533.34
O_3	535.42	534.35

where: C_1 =CC and CH, C_2 =bC to ester, C_3 =C–O, C_4 =ester (C=O)–O, O_1 = ester(C=O)–O, O_2 = carbonyl (C=O) and O_3 =carboxylic (O=C)–OH

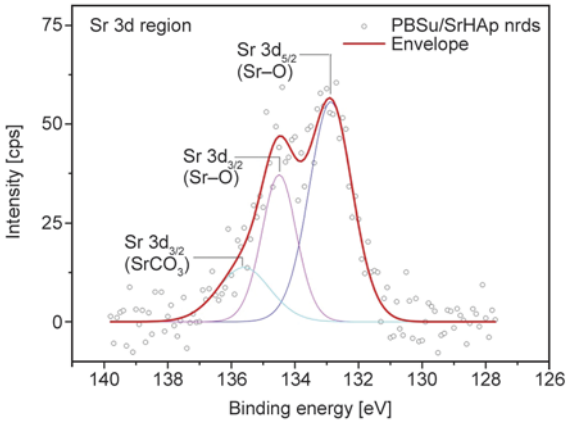

Figure 4. XPS spectra of PBSu/$Sr_5(PO_4)_3$ 2.5 wt% nanocomposite in Sr3d region

tive quantitative spectroscopic technique and for this reason penetration depth is low. For the nanocomposites with SrHAp nrds content less than 2.5 wt% it is probable that the nanofiller was embedded in the polymeric matrix during bulk polymerization and thus was not possible to be detected in order to investigate chemical bonds.

The binding energies of the sample PBSu/SrHAp nrds 2.5 wt% are presented in Table 2. Comparing the carbonyl group binding energies between neat PBSu and its nanocomposite with 2.5 wt% SrHAp nrds it can be seen that these are almost identical. However, same small differences are recorded in the oxygen region and mainly of the O_1 ester and O_3 carboxylic group (Figure 3). These values are slightly to lower binding energies indicating the existence of some interactions between PBSu and these nanoparticles [17].

After the peak analysis in the Sr3d region of the XPS spectrum at (130.5–137.6 eV) for the PBSu/SrHAp nrds 2.5 wt% nanocomposite, it is clear that new peaks are formed, indicating the formation of new covalent bonds between SrHAp nrds nanoparticles and PBSu (Figure 4). Probably, a new chemical bond (Sr–O–C) is formed by the reaction between Sr–OH and the hydroxyl end groups of PBSu macromolecular chains. The binding energy of this new peak is 137.6 eV, while the peaks at 132.86 and 134.52 eV more likely correspond to Sr–O bonds of SrHAp nrds [10, 18, 19].

Regarding WAXD analysis, many interesting results could be concluded studying XRD pattern of PBSu and its nanocomposites. However, the authors focus firstly on the confirmation of PBSu synthesis and secondly on the effect of nanofiller on the degree of crystallinity. The crystalline structure of the nanocomposites was studied using XRD. The crystal unit cell of PBSu is monoclinic and diffraction peaks from [020] and [110] are observed at 2θ 19.8 and 22.6° respectively [9, 11, 20]. Although SrHAp nanorods are crystalline materials none of their peaks can be recognized, even these with high intensity at 20.4, 26.6 and 31°, because they are overlapped by denser PBSu peaks (Figure 5). In general, as no shifting of PBSu peaks is observed, we deduce that the unit cells of the polyester and nanofillers remain the same. However, the addition of SrHAp nanorods has a small effect on the PBSu degree of crystallinity, which in neat PBSu is about 41.2%. This was slightly increased in nanocomposites containing 0.5, 1 and 2.4 wt% SrHAp nanorods to 42.5, 43.1 and 43.3%, respectively. This is because SrHAp nanorods may act as nucleating agents promoting the heterogeneous nucleation of PBSu.

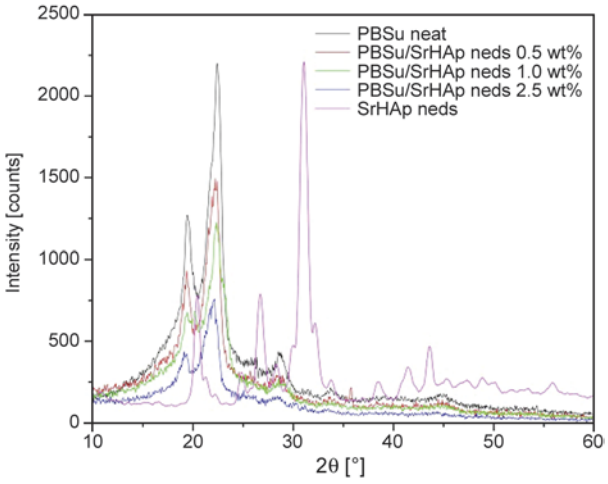

Figure 5. XRD patterns of neat PBSu, neat SrHAp nanorods and their nanocomposites containing different content of SrHAp nanorods

3.2. Morphological, mechanical and dynamic mechanical analysis of PBSu/SrHAp nrd nanocomposites.

Considering that low adhesion between the used nanoadditives and the PBSu matrix could affect their dispersion, we analysed their morphological features. In Figures 6 and 7, HAADF-STEM images of the samples SrHAp nanorods 0.5 and 1.0 wt% respectively, inside the polymeric matrix in low and high magnification, are presented. From these images the particles seem to aggregate, even though we can observe a better dispersion for the sample consisting of 0.5 wt% the nanorods compared to that with the 1.0 wt% concentration,. It seems that the dispersion of nanorods in 1,4-butanediol by ultrasonic vibration, before their *in situ* addition in the PBSu matrix, contributed to the high level of dispersion (≤0.5 μm) and distribution in the polymer matrix. This was the main problem in our previous study in which PBSu/SrHAp nrds nanocomposites have been prepared by melt mixing using 5 and 20 wt% SrHAp nrds [9].

It is well known that the filler dispersion inside the polymer matrix affects the mechanical properties of the materials. From the stress-strain curves of neat PBSu and its nanocomposites it is found that all materials are very brittle since they are breaking before yielding. This is maybe due to the low molecular weight of all materials. From these curves the tensile strength at break, elongation at break and Young's modulus were calculated and presented in Table 3.

Despite that PBSu is a rigid material with high Young's modulus ~408 MPa, it is still brittle, as it does not withstand much elongation before breaking (elongation at break ~9%). Indeed the low flex-

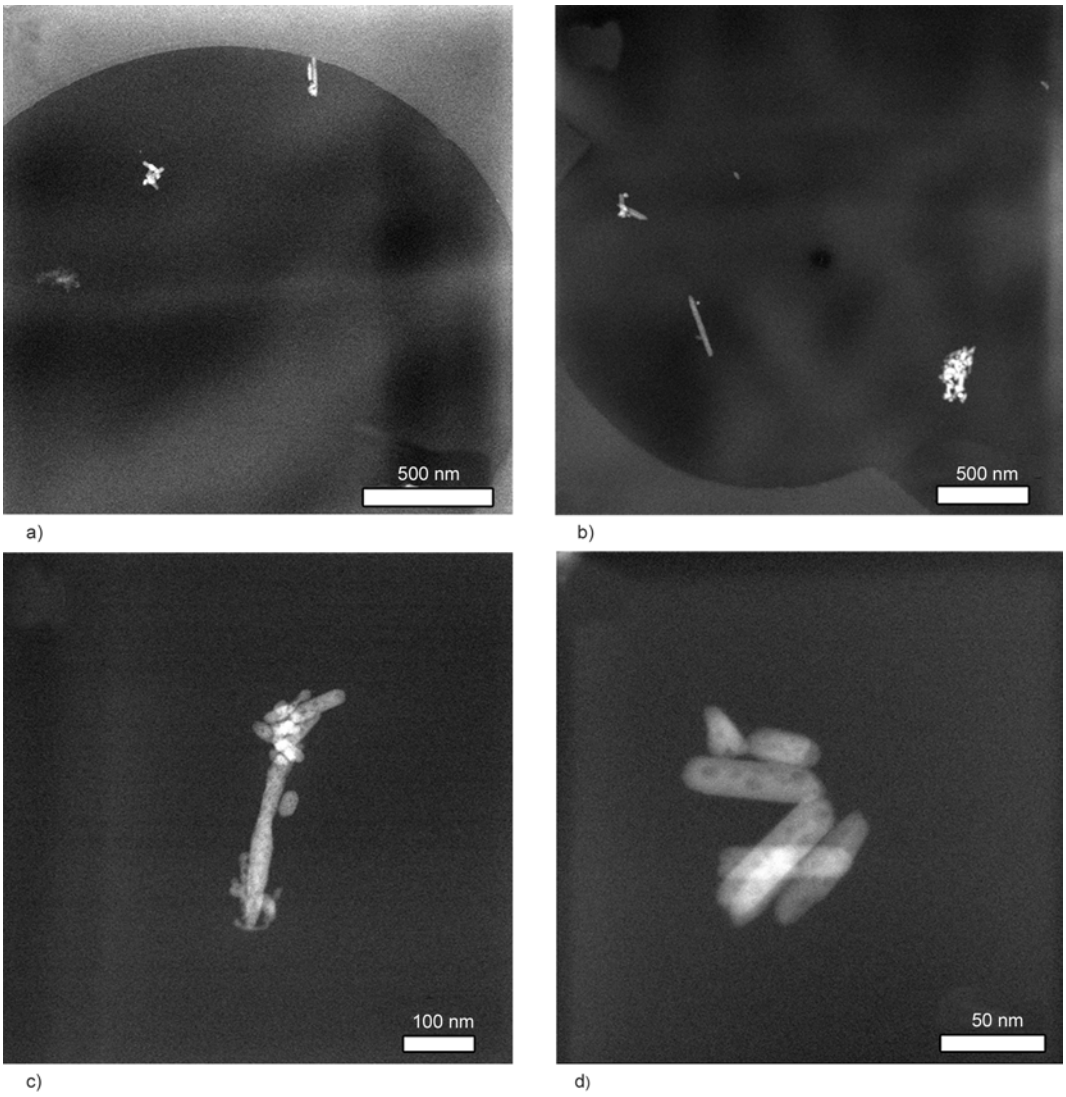

Figure 6. (a)–(d) Low and high magnification HAADF-STEM images of the sample PBSu-SrHAp 0.5 wt% showing the dispersion of the SrHAp nanorods (brighter features) inside the polymeric matrix

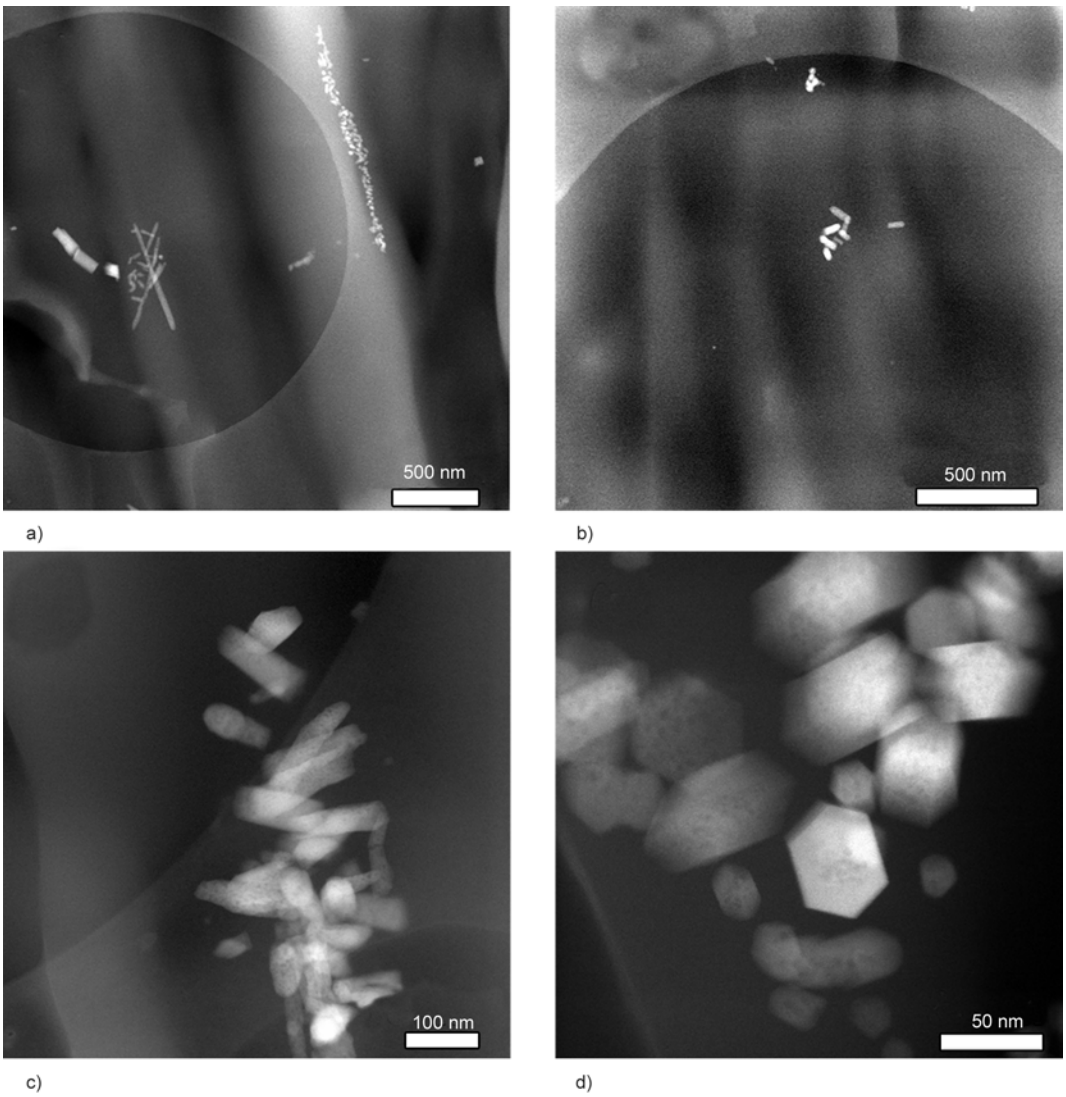

Figure 7. (a)–(d) Low and high magnification HAADF-STEM images of the sample PBSu-SrHAp 1.0 wt% showing the dispersion of the SrHAp nanorods (brighter features) inside the polymeric matrix

ibility is the main problem with aliphatic polyesters and for this reason commercially available materials are prepared using a multifunctional additive as co-monomer. The addition of nano-filler cannot alter the mechanical behaviour of these nanocomposites as evidenced by the almost identical stress-strain curves that recorded breaking before the yielding point (data not shown). However, the presence of the nanoparticles in the PBSu matrix at very low concentration induces improvement of its mechanical properties. Young's modulus, increases from 408 MPa in neat PBSu to 415 MPa in the PBSu/SrHAp nrds 0.5 wt% nanocomposite while tensile strength is also increased from and elasticity increases from 27.42 MPa to 30.66 respectively in the nanocomposite. This is probably due to its higher molecular weight (M_n 51 100 g/mol) as confirmed from gel permeation chromatography and maybe because the SrHAp nanorods can act as reinforcement agents. Furthermore, the lack of extended

Table 3. Mechanical properties of neat PBSu and its nanocomposites containing different SrHAp nanorods content. Standard deviation (σ) has been calculated using the following formula: $\sigma = \sqrt{\Sigma(x - mean)^2/N}$.

Sample	Tensile strength at break [MPa]	Elongation at break [%]	Young's Modulus [MPa]
PBSu	27.42±0.3	9±0.2	408±60
PBSu/SrHAp nrds 0.5 wt%	30.66±0.3	12±0.3	415±50
PBSu/SrHAp nrds 1.0 wt%	24.55±0.4	8±0.4	377±70
PBSu/SrHAp nrds 2.5 wt%	Brittle specimen		

agglomerates, which can act as points of stress concentration that promote material failure, probably contribute to this behaviour [15, 21]. For the sample PBSu/SrHAp nrds 1.0 wt% both Young's modulus and elongation at break aggravated, whereas the nanocomposite PBSu/SrHAp nrds 2.5 wt% was too brittle to withstand tensile testing. This deterioration of mechanical properties can be attributed to the significantly decreased molecular weight of these samples (M_n = 37 790 g/mol and M_n = 21550 g/mol respectively) compared with neat PBSu, or it can be the result of the presence of aggregates in the polymer matrix. In general the nanoparticles act as reinforcing materials for a concentration up to 0.5 wt%. DMA was also used to study the prepared nanocomposites and the reinforcement effect of the nanoparticles. The temperature dependence of the storage modulus (E') and tan δ for *in situ* prepared samples is presented in Figure 8. The nanocomposite PBSu/SrHAp nrds 2.5 wt% could not be measured under these conditions of deformation, due to its significant brittleness. As can be seen E' gradually decreases with increasing temperature and a transition is observed between –60 and –10°C, which is ascribed to the glass transition temperature of PBSu (*T*g) [17]. At low temperatures the storage modulus is higher compared with neat PBSu confirming the reinforcement effect of the nanorods. The increase is bigger in the case of a nanocomposite containing 0.5 wt% SrHAp nrds, in agreement with the results from the tensile test. This fact can be attributed to the restriction of the molecular motion of the PBSu macromolecules due to the fine dispersion of the nanofillers, which leads to increased interactions with the polymer matrix [15, 22]. The extent of this reinforcement is limited above the T_g due to the higher molecular motion of the PBSu macromolecular chains [17]. Thus above the T_g the storage modulus sharply decreases and all nanocomposites have almost similar storage moduli. The restricted molecular motion of the nanocomposites can also be seen from the tan δ curve (Figure 8b). In all nanocomposites this peak has a smaller intensity, compared with neat PBSu. Furthermore, the tan δ curve is progressively shifted to higher values by increasing the nanorod content. Such variation can be found in nanocomposites since between the polymer matrix and the nanofillers there is an interface in which, due to the interactions, the segmental mobility of macromolecules is lower compared with the matrix. However, in the present study the variation in T_g is higher (6°C) than in the usual nanocomposites. This is due to the formed covalently bonds between nanorods and PBSu macromolecules, which further restricts the chain movement.

3.3. Enzymatic hydrolysis of nanocomposites

Specific properties are sometimes required for biomaterials. For example, tissue engineering scaffolds should have both good biocompatibility and cell adhesive properties, in addition to needed biodegradable properties [23]. Polyesters having a relatively large number of methylene groups and those having a- and b-ester bonds as PBSu with low T_m are hydrolysable by lipases [24]. As was reported in the experimental section, enzymatic hydrolysis of PBSu and its nanocomposites was studied in aqueous solutions containing a mixture of *R. delemar* and *Pseudomonas Cepacia* lipases, at 37°C and pH = 7.2 for 40 days. Enzymatic hydrolysis rates of the

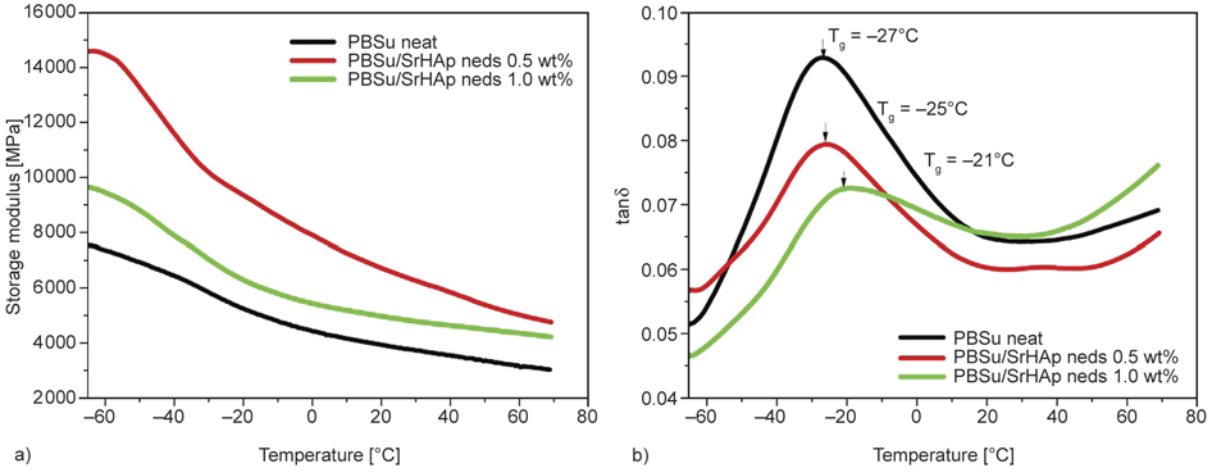

Figure 8. DMA diagrams of neat PBSu and its nanocomposites containing different SrHAp nanorods content. a) Storage modulus variation and b) tan δ variation versus temperature.

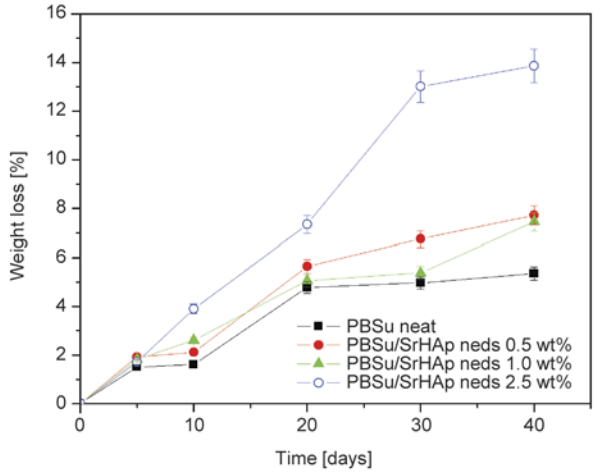

Figure 9. Mass loss graphs of neat PBSu and its nanocomposites during enzymatic hydrolysis

nanocomposites were found significantly different from those of neat PBSu. Figure 9 shows the weight loss of the specimens, expressed as a fraction of 100 (percentage) of the initial mass of the specimen as a function of time of enzymatic hydrolysis. As can be seen, pristine PBSu hydrolyzes slowly losing only about 5% of its original mass after 40 days of enzymatic treatment. The SrHAp nanorods enhance enzymatic hydrolysis and it can be seen that as the amount of nanoparticles increases, the hydrolysis rate becomes higher. PBSu/SrHAp nrds 2.5 wt% shows the fastest enzymatic degradation among the tested samples, losing 14% of its initial after 40 days of enzymatic hydrolysis. These results are in accordance with our previous study on PBSu/SrHAp nanorods and PBSu/SiO_2 nanotubes nanocomposites prepared by the melt mixing technique, where the nanocomposites reported that have higher hydrolysis rates that of neat PBSu [9]. Li *et al*. [25] found that PLA/SiO_2 nanocomposites degrade faster than neat PLA, indicating that incorporation of silica enhances biodegradation of PLA in nanocomposites too. The authors suggested that the addition of silica may lead to a facile attack of the enzyme molecule towards the ester groups of the PLA chains, because of silica's hydrophilicity. All this is in agreement with our study since the addition of SrHAp nanorods accelerates the enzymatic hydrolysis of PBSu due to the initiation of the heterogeneous hydrolysis of polyester by terminal hydroxylated edge groups [26]. However, Vasileiou *et al*. reported that the presence of fumed silica particles has a negative effect on the degradation level of PESu since it reduces macromolecular chain mobility. A reduced hydrolysis rate was also found in PPSeb/MMT nanocomposite, which is in agreement with some reported findings in literature [17, 27, 28]. tR1

Enzymatic degradation of polyesters can be affected by several factors, having to do with the chemical structure, the type and amount of filler, the solid-state of the degraded specimen. Hydrophilic/hydrophobic balance segments within the main chain, molecular weight, frequency of ester bonds along the macromolecular chains, as well as segmental mobility of the macromolecules can also influence the rate of biodegradation [17]. The molecular weight could be a notable factor for such differences since nanocomposites with 1.0 and 2.5 wt% of nanofiller have higher molecular weights than neat PBSu and this could justify the faster enzymatic hydrolysis rates observed. As the degradation rate is associated with the ability of water to wet and subsequently absorb into the nanocomposites, the hydrophilic or hydrophobic character of the nanoparticle can have a strong influence on the extent to which hydrolysis occurs. The hydrophobicity of the samples was evaluated by measuring their contact angle and water uptake Table 4. Neat PBSu has a contact angle of 76.2±0.3°. The addition of SrHAp nanorods seems to decrease gradually the contact angle of nanocomposites, indicating that the materials becomes more hydrophilic. This observation is in good agreement with previous work on PBSu composites, where the addition of poly(l-lactic acid) (PLLA)-grafted TTCP particles (g-TTCP) in the PBSu effectively improved its hydrophobic property [29]. PBSu/SrHAp nanocomposites with 0.5, 1 and 2.5 wt% nanorods have contact angles 74±1, 72.9±0.50 and 70.3±0.2° respectively. PBSu/SrHAp nrds with 2.5 wt% nanorods is the most hydrophilic material due to the high hydrophilic nature of the nanofiller and thus it has the lowest contact angle. This higher hydrophilicity may explain the higher enzymatic hydrolysis rate *f* nanocomposites compared with neat PBSu.

Table 4. Contact angle measurements of prepared nanocomposites. Standard deviation (σ) has been calculated using the following formula:

$$\sigma = \sqrt{\Sigma(x - mean)^2/N}.$$

Sample	Contact angle [°]
PBSu neat	76.2±0.3
PBSu/SrHAp nanorods 0.5%	74.0±1.0
PBSu/SrHAp nanorods 1.0%	72.9±0.5
PBSu/SrHAp nanorods 2.5%	70.3±0.2

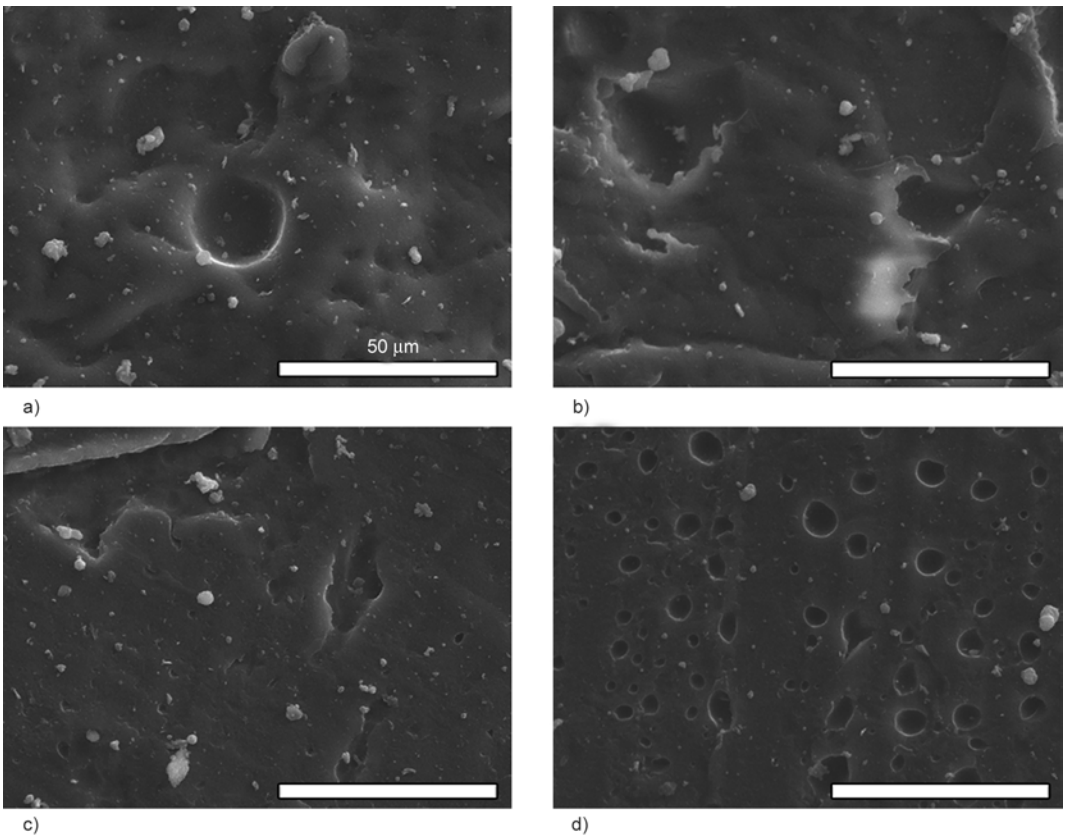

Figure 10. SEM images of (a) the neat sample and the samples with b) 0.5 wt%, (c) 1 wt% and (d) 2.5 wt% SrHAp nanorods after 20 days of enzymatic hydrolysis. The scale is identical in all images.

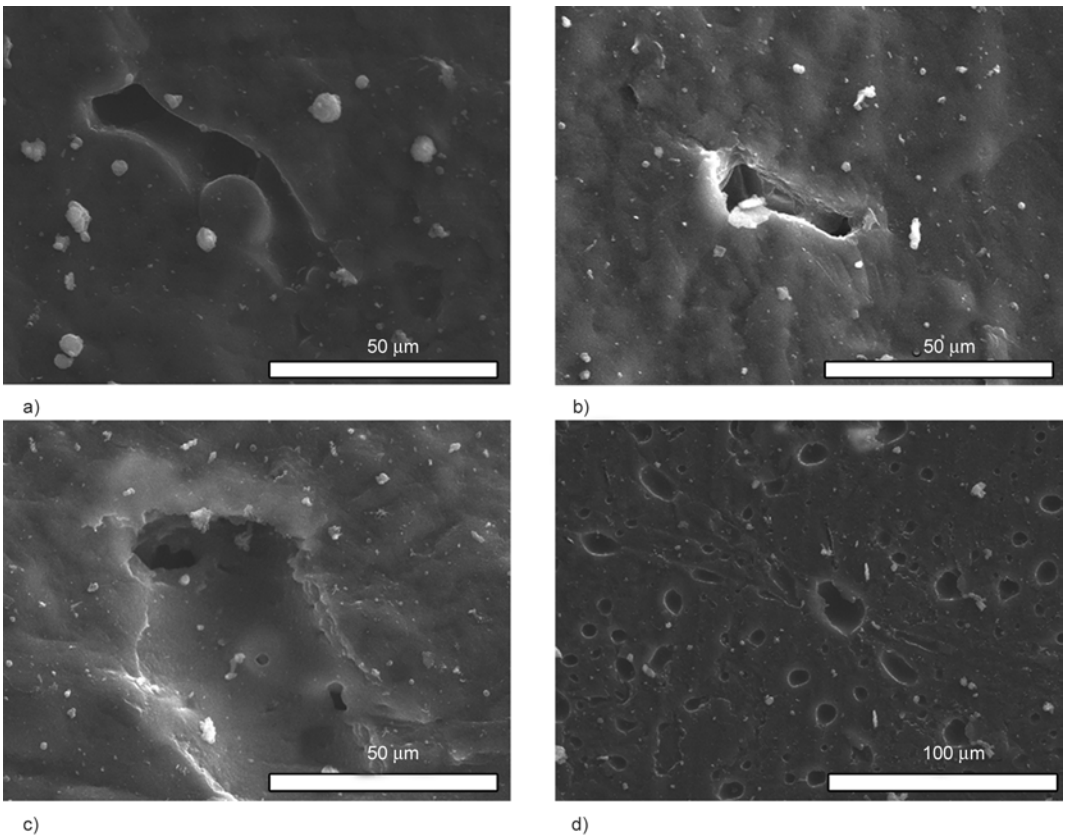

Figure 11. SEM images of (a) the neat sample and the samples with (b) 0.5 wt%, (c) 1 wt% and (d) 2.5 wt% SrHAp nanorods after 40 days of enzymatic hydrolysis

Weight loss measurements provide a general trend of the enzymatic hydrolysis, but don't reveal how this hydrolysis proceeds. For this reason, the morphology of the prepared samples before and after enzymatic hydrolysis was examined using SEM. Neat PBSu presents a less deteriorated surface with only a few cracks and holes appearing after 20 days of enzymatic hydrolysis. On the other hand, nanocomposites exhibit a much damaged surface, almost fully covered by big holes and cracks in some samples, in agreement with the mass-loss results (Figure 10). The most degraded nanocomposite is the one containing 2.5 wt% SrHAp nanorods, which after 40 days of hydrolysis exhibits a highly and well distributed porous-like morphology (Figure 11).

This fact can be attributed to the higher mass loss of the nanocomposites that takes place during enzymatic hydrolysis. In our previous work using higher amounts of nanorods (5 and 20 wt%) and due to their low adhesion with the PBSu matrix, a 'gap' between PBSu and inorganic nanoparticles was formed and lipases could diffuse inside the polymer matrix forming a porous structure. The formation of such a gap and porous structure is known to accelerate the enzymatic degradation of biodegradable polyesters [30]. However, in the present study such a 'gap' was not found from SEM measurements and the higher rate of enzymatic hydrolysis of nanocomposites should be attributed to the higher hydrophylicity of the added nanorods.

3.4. *In vitro* bioactivity test

A bioactive material is defined as a material that elicits a specific biological response at the interface of the material which results in the formation of a bond between the tissue and the material. Kokubo *et al*. [31] suggested that for the bioactive glasses forming surface silanols upon hydration, a silica hydrogel layer is produced by exchange of ions in the SBF, and that this layer acts as a nucleation agent for apatite crystal formation. Once the apatite crystals are formed, they grow by consuming calcium and phosphate ions from the SBF [31]. Given the similarities in composition between bioglass and polymeric systems, many authors have suggested that the formation of hydroxyapatite on the polymer surface may follow a similar mechanism [32, 33]. Figure 12 shows the morphology of PBSu after soaking in SBF for 14 days. Nucleation and growth have occurred on the exposed surfaces, resulting in clusters of mineral precipitates. A similar behaviour was found also in PBSu/SrHAp nrds nanocomposites (Figure 13). Most of the PBSu and PBSu/SrHAp nrds nanocomposites' surfaces were covered by a needle-like apatite layer as shown in Figures 12 and 13. As can be seen from the SEM micrographs apatite layers are further thickened and it was found that a cauliflower-like apatite cluster formed on the surface of these samples. This finding is in agreement with a previous study on plasma-treated PBSu scaffolds [7]. The results obtained by SEM are confirmed by EDX analysis (Figure 12b and Figure 13b) and a significant variation in the intensity of Si, P, and Ca can be observed in PBSu nanocomposites with different content of SrHAp nanorods. After soaking in SBF, the concentration of Ca and P increase, accompanied by the increase of SrHAp naorods in the PBSu matrix for a concentration of the nanofiller up to 1.0 wt%. These results confirm to some extent our initial expectations derived from the literature, that when nanophase (compared to conventional) particles are incorporated into the polymer composite they promote mineral deposition onto the surfaces [34–36].

To characterize the inorganic phase formed onto the surfaces of PBSu and its nanocomposites, XRD analysis was performed on neat PBSu and its nanocomposites after soaking in SBF for 14 days (Figure 14). PBSu is a typical semicrystalline polymer with two characteristic peaks at 2θ 19.8 and 22.6° while the features of interest consists of a broad contour between 2θ = 27–37° resulting from the 002 reflection of hydroxyapatite. New peaks are observed at 2θ 32,4 36,45 and 46° after immersion in SBF which confirm that partially crystallized apatite layer formed on the surfaces of PBSu film as well as on its nanocomposites [33, 37, 38].

3.5. Cell studies

The metabolic activity of MG-63 cells cultivated for 48 h is illustrated in Figure 15. In all cases, except for the scaffold with 0.5 wt% of Sr, the metabolic activity of MG63 cells was significantly ($p < 0.05$) reduced compared to the reference. However, the metabolic activity of all materials was higher than 50%, which is considered as the limit for biocompatibility [39].

These results were further confirmed by SEM after 48 h of cultivation (Figure 16). Although it is hard to detect the dense MG-63 cell monolayer, in all

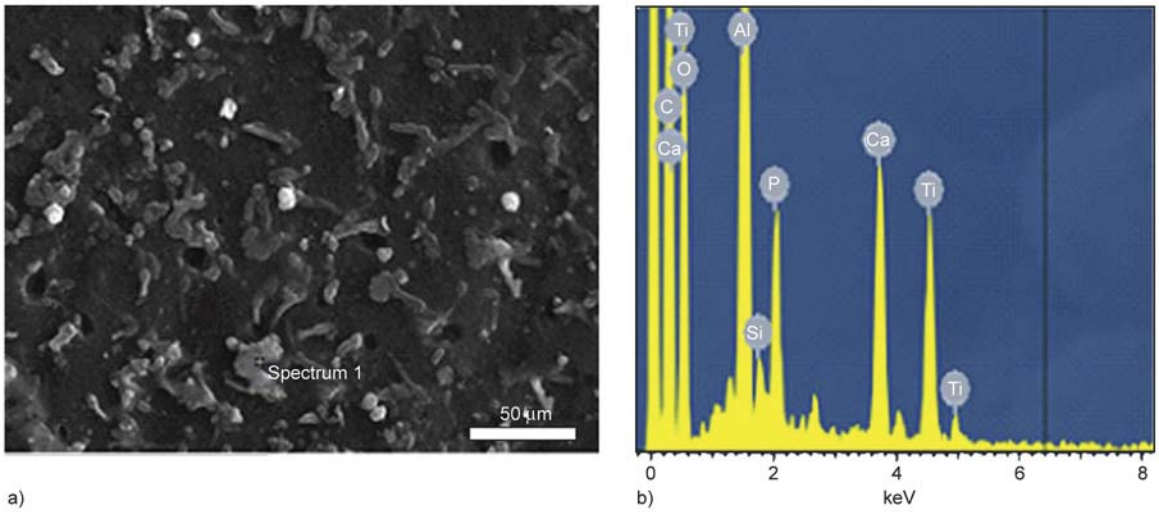

Figure 12. a) SEM micrographs of neat PBSu after soaking in SBF for 14 days and b) EDX analysis of PBSu surface indicating the formation of hydroxyapatite

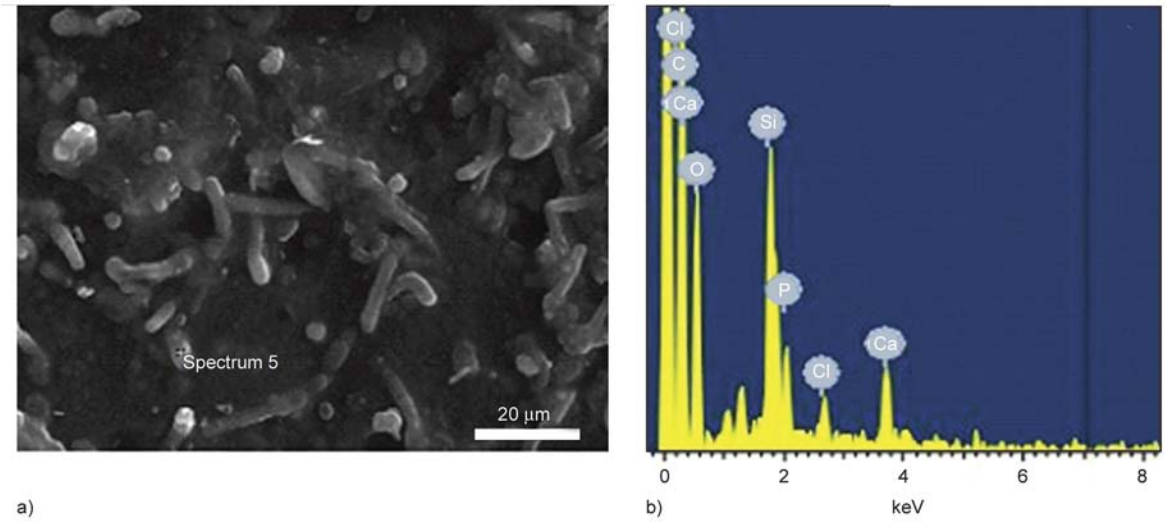

Figure 13. a) SEM micrographs of PBSu/SrHAp nrds containing 0.5 wt% nanorods after soaking in SBF for 14 days and b) EDX analysis of nanocomposites surface indicating the formation of hydroxyapatite

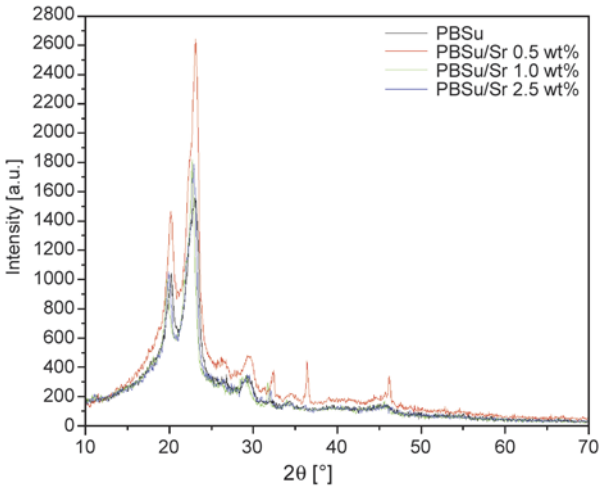

Figure 14. XRD patterns of neat PBSu and its nanocomposites after soaking in SBF for 14 days

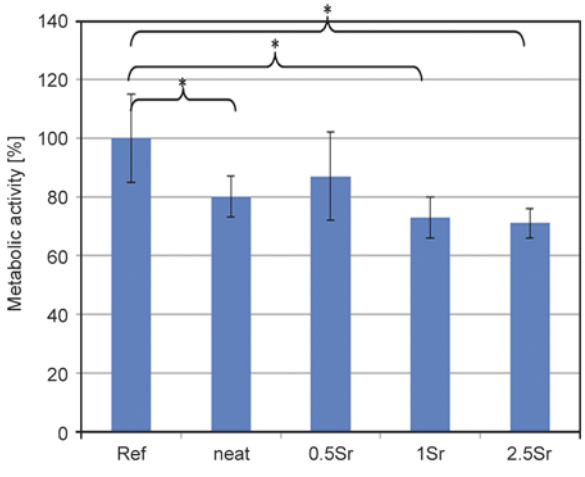

Figure 15. Metabolic activity of MG-63 cells cultivated for 48 h on plane composite samples

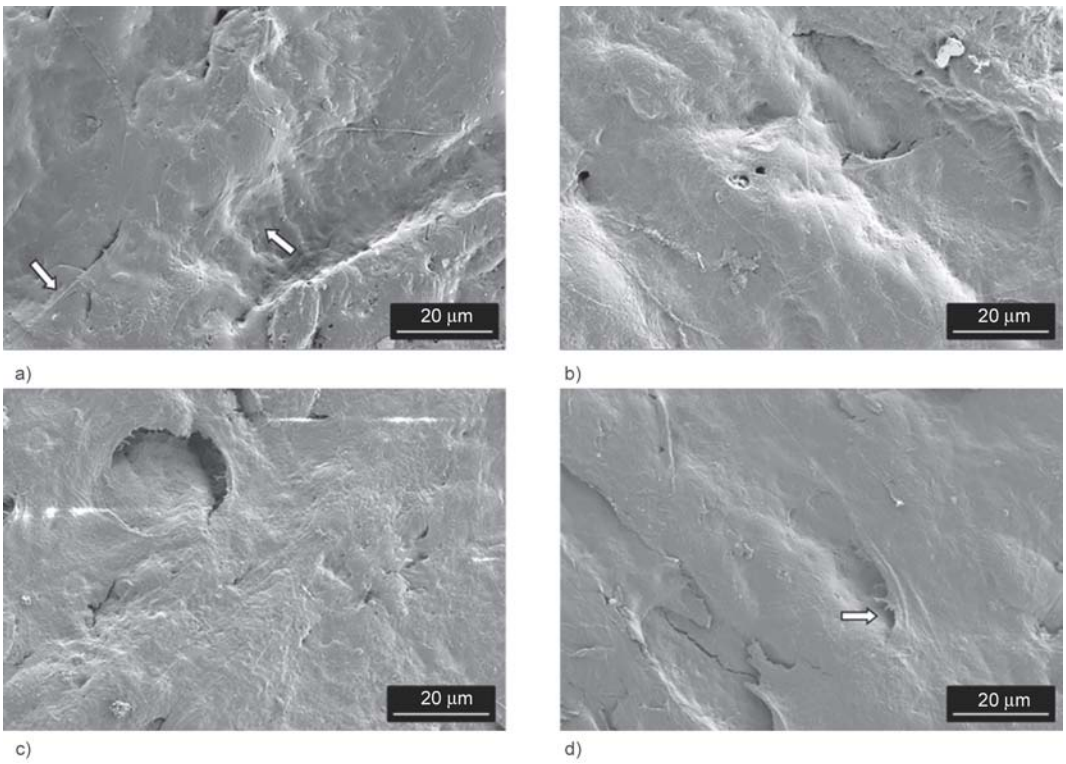

Figure 16. SEM images of (a) the neat sample and the samples with (b) 0.5 wt%, (c) 1 wt% Sr and (d) 2.5 wt% nanorods after incubation with MG63 for 48 hours

cases the cells have attached and spread on the entire surface of the samples. As the expressed morphology of the MG-63 cells on the different surfaces are very flat, no obvious difference in cell behaviour could be analysed applying the different scaffold compositions.

In summary, although a significant reduction of metabolic activity was measured in MG-63 after 48 h of incubation on the test samples compared to the reference, no difference was shown in the cell morphology study. It can therefore be concluded that the tested materials are biocompatible *in vitro* and further *in vitro* and *in vivo* studies have to be carried out to confirm the osteogenic potential of the developed materials in the context of bone regeneration.

4. Conclusions

SrHAp nrds have been hydrothermally synthesized. Afterwards, PBSu nanocomposites containing SrHAp nrds at different concentrations have been *in situ* prepared and studied as potential materials for tissue engineering applications. GPC analysis verified that macromolecules with satisfying M_w and M_n values were obtained while XPS spectra indicated the presence of some interactions between the inorganic filler and the PBSu matrix. The nanocomposite containing 0.5 wt% SrHAp nrds, improved the mechanical properties but further increase of the nanofiller content up to 2.5 wt% caused a deterioration of the mechanical properties as a result of the bad dispersion in the PBSu matrix. It was also found that the nanofiller enhanced enzymatic hydrolysis probably due to the initiation of heterogeneous hydrolysis of the polyester by terminal hydroxylated edge groups. SrHAp nrds can transform the bioinert PBSu surface into a bioactive one, promoting hydroxyapatite formation in SBF solution. In addition to the apatite formation enhancement, SrHAp nrds can induce osteoblast compatibility. Nanocomposites have more hydrophilic surfaces compared to pristine PBSu, thereby causing more osteoblasts to adhere and proliferate on them.

Acknowledgements

The authors wish to acknowledge co-funding of this research by IKY (Greece) and DAAD (Germany), Action 'IKYDA 2012' and the financial support from the European Union under the Seventh Framework Program (Integrated Infrastructure Initiative No. 262348 European Soft Matter Infrastructure, ESMI).

References

[1] Ouchi T., Ohya Y.: Design of lactide copolymers as biomaterials. Journal of Polymer Science Part A: Polymer Chemistry, **42**, 453–462 (2003).
DOI: 10.1002/pola.10848

[2] Puskas J. E., Chen Y.: Biomedical application of commercial polymers and novel polyisobutylene-based thermoplastic elastomers for soft tissue replacement. Biomacromolecules, **5**, 1141–1154 (2004).
DOI: 10.1021/bm034513k

[3] Sabir M. I., Xu X., Li L.: A review on biodegradable polymeric materials for bone tissue engineering applications. Journal of Materials Science, **44**, 5713–5724 (2009).
DOI: 10.1007/s10853-009-3770-7

[4] Li H., Chang J., Cao A., Wang J.: *In vitro* evaluation of biodegradable poly(butylene succinate) as a novel biomaterial. Macromolecular Bioscience, **5**, 433–440 (2005).
DOI: 10.1002/mabi.200400183

[5] Vroman I., Tighzert L.: Biodegradable polymers. Materials, **2**, 307–344 (2009).
DOI: 10.3390/ma2020307

[6] Costa-Pinto A. R., Correlo V. M., Sol P. C., Bhattacharya M., Srouji S., Livne E., Reis R. L., Neves N. M.: Chitosan–poly(butylene succinate) scaffolds and human bone marrow stromal cells induce bone repair in a mouse calvaria model. Journal of Tissue Engineering and Regenerative Medicine, **6**, 21–28 (2012).
DOI: 10.1002/term.391

[7] Wang H., Ji J., Zhang W., Zhang Y., Jiang J., Wu Z., Pu S., Chu P. K:. Biocompatibility and bioactivity of plasma-treated biodegradable poly(butylene succinate). Acta Biomaterialia, **5**, 279–287 (2009).
DOI: 10.1016/j.actbio.2008.07.017

[8] Christenson E. M., Anseth K. S., van den Beucken J. J. J. P., Chan C. K., Ercan B., Jansen J. A., Laurencin C. T., Li W-J., Murugan R., Nair L. S., Ramakrishna S., Tuan R. S., Webster T. J., Mikos A. G.: Nanobiomaterial applications in orthopedics. Journal of Orthopaedic Research, **25**, 11–22 (2007).
DOI: 10.1002/jor.20305

[9] Grigoriadou I., Nianias N., Hoppe A., Terzopoulou Z., Bikiaris D., Will J., Hum J., Roether J. A., Detsch R., Boccaccini A. R.: Evaluation of silica-nanotubes and strontium hydroxyapatite nanorods as appropriate nano-additives for poly(butylene succinate) biodegradable polyester for biomedical applications. Composites Part B: Engineering, **60**, 49–59 (2014).
DOI: 10.1016/j.compositesb.2013.12.015

[10] Zhang C., Li C., Huang S., Hou Z., Cheng Z., Yang P., Peng C., Lin J.: Self-activated luminescent and mesoporous strontium hydroxyapatite nanorods for drug delivery. Biomaterials, **31**, 3374–3383 (2010).
DOI: 10.1016/j.biomaterials.2010.01.044

[11] Ahn B. D., Kim S. H., Kim Y. H., Yang J. S.: Synthesis and characterization of the biodegradable copolymers from succinic acid and adipic acid with 1,4-butanediol. Journal of Applied Polymer Science, **82**, 2808–2826 (2001).
DOI: 10.1002/app.2135

[12] Bikiaris D., Karavelidis V., Karayannidis G.: A new approach to prepare poly(ethylene terephthalate)/silica nanocomposites with increased molecular weight and fully adjustable branching or crosslinking by SSP. Macromolecular Rapid Communications, **27**, 1199–1205 (2006).
DOI: 10.1002/marc.200600268

[13] Vassiliou A. A., Chrissafis K., Bikiaris D. N.: *In situ* prepared PBSu/SiO_2 nanocomposites. Study of thermal degradation mechanism. Thermochimica Acta, **495**, 120–128 (2009).
DOI: 10.1016/j.tca.2009.06.010

[14] Han S-I., Lim J. S., Kim D. K., Kim M. N., Im S. S.: *In situ* polymerized poly(butylene succinate)/silica nanocomposites: Physical properties and biodegradation. Polymer Degradation and Stability, **93**, 889–895 (2008).
DOI: 10.1016/j.polymdegradstab.2008.02.007

[15] Vassiliou A. A., Bikiaris D., Mabrouk K., Kontopoulou M.: Effect of evolved interactions in poly(butylene succinate)/fumed silica biodegradable *in situ* prepared nanocomposites on molecular weight, material properties, and biodegradability. Journal of Applied Polymer Science, **119**, 2010–2024 (2010).
DOI: 10.1002/app.32887

[16] Zhang W., Nefedov A., Naboka M., Cao L., Wöll C.: Molecular orientation of terephthalic acid assembly on epitaxial graphene: NEXAFS and XPS study. Physical Chemistry Chemical Physics, **14**, 10125–10131 (2012).
DOI: 10.1039/C2CP23748B

[17] Bikiaris D. N., Nianias N. P., Karagiannidou E. G., Docoslis A.: Effect of different nanoparticles on the properties and enzymatic hydrolysis mechanism of aliphatic polyesters. Polymer Degradation and Stability, **97**, 2077–2089 (2012).
DOI: 10.1016/j.polymdegradstab.2011.10.024

[18] Wang H., Ji J., Zhang W., Wang W., Zhang Y., Wu Z., Zhang Y., Chu P. K.: Rat calvaria osteoblast behavior and antibacterial properties of O_2 and N_2 plasma-implanted biodegradable poly(butylene succinate). Acta Biomaterialia, **6**, 154–159 (2010).
DOI: 10.1016/j.actbio.2009.07.026

[19] Xia W., Lindahl C., Persson C., Thomsen P., Lausmaa J., Engqvist H.: Changes of surface composition and morphology after incorporation of ions into biomimetic apatite coating. Journal of Biomaterials and Nanobiotechnology, **1**, 7–16 (2010).
DOI: 10.4236/jbnb.2010.11002

[20] Fan R. R., Zhou L. X., Li D. X., Zhang D. M., Wu M., Guo G.: Preparation and characterization of composites based on poly(butylene succinate) and poly(lactic acid) grafted tetracalcium phosphate. Journal of Macromolecular Science Part B: Physics, **53**, 296–308 (2013).
DOI: 10.1080/00222348.2013.810104

[21] Albertsson A. C., Verma I. K.: Aliphatic polyesters: Synthesis, properties and applications. Advances in Polymer Science, **157**, 1–40 (2002).
DOI: 10.1007/3-540-45734-8_1

[22] Kontou E., Niaounakis M.: Thermo-mechanical properties of LLDPE/SiO_2 nanocomposites. Polymer, **47**, 1267–1280 (2006).
DOI: 10.1016/j.polymer.2005.12.039

[23] Liu X., Ma P. X.: Polymeric scaffolds for bone tissue engineering. Annals of Biomedical Engineering, **32**, 477–486 (2004).
DOI: 10.1023/B:ABME.0000017544.36001.8e

[24] Herzog K., Müller R-J., Deckwer W-D.: Mechanism and kinetics of the enzymatic hydrolysis of polyester nanoparticles by lipases. Polymer Degradation and Stability, **91**, 2486–2498 (2006).
DOI: 10.1016/j.polymdegradstab.2006.03.005

[25] Li Y., Han C., Bian J., Han L., Dong L., Gao G.: Rheology and biodegradation of polylactide/silica nanocomposites. Polymer Composites, **33**, 1719–1727 (2012).
DOI: 10.1002/pc.22306

[26] Fukushima K., Tabuani D., Camino G.: Nanocomposites of PLA and PCL based on montmorillonite and sepiolite. Materials Science and Engineering: C, **29**, 1433–1441 (2009).
DOI: 10.1016/j.msec.2008.11.005

[27] Lee S-R., Park H-M., Lim H., Kang T., Li X., Cho W-J., Ha C-S.: Microstructure, tensile properties, and biodegradability of aliphatic polyester/clay nanocomposites. Polymer, **43**, 2495–2500 (2002).
DOI: 10.1016/S0032-3861(02)00012-5

[28] Nerantzaki M., Papageorgiou G. Z., Bikiaris D. N.: Effect of nanofiller's type on the thermal properties and enzymatic degradation of poly(ε-caprolactone). Polymer Degradation and Stability, **108**, 257–268 (2014).
DOI: 10.1016/j.polymdegradstab.2014.03.018

[29] Fan R. R., Zhou L. X., Song W., Li D. X., Zhang D. M., Ye R., Zheng Y., Guo G.: Preparation and properties of g-TTCP/PBS nanocomposites and its *in vitro* biocompatibility assay. International Journal of Biological Macromolecules, **59**, 227–234 (2013).
DOI: 10.1016/j.ijbiomac.2013.04.051

[30] Tsuji H., Kawashima Y., Takikawa H., Tanaka S.: Poly(L-lactide)/nano-structured carbon composites: Conductivity, thermal properties, crystallization, and biodegradation. Polymer, **48**, 4213–4225 (2007).
DOI: 10.1016/j.polymer.2007.05.040

[31] Kokubo T., Kushitani H., Sakka S., Kitsugi T., Yamamuro T.: Solutions able to reproduce *in vivo* surface-structure changes in bioactive glass-ceramic A–W^3. Journal of Biomedical Materials Research, **24**, 721–734 (1990).
DOI: 10.1002/jbm.820240607

[32] Chouzouri G., Xanthos M.: *In vitro* bioactivity and degradation of polycaprolactone composites containing silicate fillers. Acta Biomaterialia, **3**, 745–756 (2007).
DOI: 10.1016/j.actbio.2007.01.005

[33] Hong Z., Reis R. L., Mano J. F.: Preparation and *in vitro* characterization of novel bioactive glass ceramic nanoparticles. Journal of Biomedical Materials Research Part A, **88**, 304–313 (2009).
DOI: 10.1002/jbm.a.31848

[34] Wei G., Ma P. X.: Structure and properties of nano-hydroxyapatite/polymer composite scaffolds for bone tissue engineering. Biomaterials, **25**, 4749–4757 (2004).
DOI: 10.1016/j.biomaterials.2003.12.005

[35] Webster T. J., Smith T. A.: Increased osteoblast function on PLGA composites containing nanophase titania. Journal of Biomedical Materials Research Part A, **74**, 677–686 (2005).
DOI: 10.1002/jbm.a.30358

[36] Peter M., Binulal N. S., Soumya S., Nair S. V., Furuike T., Tamura H., Jayakumar R.: Nanocomposite scaffolds of bioactive glass ceramic nanoparticles disseminated chitosan matrix for tissue engineering applications. Carbohydrate Polymers, **79**, 284–289 (2010).
DOI: 10.1016/j.carbpol.2009.08.001

[37] Chavan P. N., Bahir M. M., Mene R. U., Mahabole M. P., Khairnar R. S.: Study of nanobiomaterial hydroxyapatite in simulated body fluid: Formation and growth of apatite. Materials Science and Engineering: B, **168**, 224–230 (2010).
DOI: 10.1016/j.mseb.2009.11.012

[38] Gadaleta S. J., Paschalis E. P., Betts F., Mendelsohn R., Boskey A. L.: Fourier transform infrared spectroscopy of the solution-mediated conversion of amorphous calcium phosphate to hydroxyapatite: New correlations between X-ray diffraction and infrared data. Calcified Tissue International, **58**, 9–16 (1996).
DOI: 10.1007/BF02509540

[39] Bruinink A., Luginbuehl R.: Evaluation of biocompatibility using *in vitro* methods: Interpretation and limitations. Advances in Biochemical Engineering/Biotechnology, **126**, 117–152 (2012).
DOI: 10.1007/10_2011_111

eXPRESS Polymer Letters Vol.9, No.9 (2015) 790–798
Available online at www.expresspolymlett.com
DOI: 10.3144/expresspolymlett.2015.74

Carboxymethylcellulose acetate butyrate/poly(4-vinyl-*N*-pentyl pyridinium bromide) blends as antimicrobial coatings

L. S. Blachechen[1], *J. Amim Jr.*[1,2], *N. Lincopan*[3,4], *D. F. S. Petri*[1*]

[1]Instituto de Química, Universidade de São Paulo, São Paulo, Brazil
[2]Instituto de Química, Universidade Federal do Rio de Janeiro, Campus Macaé, Brazil
[3]Instituto de Ciências Biomédicas, Universidade de São Paulo, São Paulo, Brazil
[4]Faculdade de Ciências Farmacêuticas, Universidade de São Paulo, São Paulo, Brazil

Received 17 January 2015; accepted in revised form 10 April 2015

Abstract. Blends of carboxymethyl cellulose acetate butyrate (CMCAB), a cellulose derivative, and poly(4-vinyl-*N*-pentyl pyridinium bromide) (QPVP-C5), an antimicrobial polymer, were prepared by casting method and characterized by means of Fourier transform infrared vibrational spectroscopy (FTIR), scanning electron microscopy (SEM), thermogravimetric analysis (TGA), differential scanning calorimetry (DSC) and contact angle measurements. Miscibility between CMCAB and QPVP-C5 was evidenced by DSC measurements of blends, which showed a single thermal event of T_g, and SEM images, which revealed homogenous morphology, regardless the blend composition. Moreover, thermal stability of QPVP-C5 was substantially enhanced, when it was mixed with CMCAB. Upon increasing the QPVP-C5 content in the blend the wettability and antimicrobial activity against Gram-positive bacteria *Micrococcus luteus* increased, indicating the surface enrichment by pyridinium groups. In fact, blends with 70 wt% QPVP-C5 reduced 5 log and 4 log the colony-forming units of *Micrococcus luteus* and *Escherichia coli*, respectively.

Keywords: *coatings, carboxymethylcellulose acetate butyrate, poly(4-vinyl-N-pentyl pyridinium bromide), antimicrobial properties, blends*

1. Introduction

Carboxymethylcellulose acetate butyrate (CMCAB) is a cellulose ester often applied as coating for cellulosic substrates, matrix component of compression tablets or support for biomolecules [1–5]. Although CMCAB has been successfully used as coating material, it could be improved to gain antimicrobial property. Such property might be achieved by immobilizing lysozyme, an enzyme that catalyzes the hydrolysis of peptidoglycans on bacterial cell walls, on the surface of CMCAB, so that the catalytic activity is high enough to kill bacteria, even after many cycles of use [5]. The incorporation of antimicrobial agents, like silver ions or silver nanoparticles [6, 7], antibiotics or quaternary ammonium compounds (QAC) [8], to polymeric matrices is also a common strategy to obtain polymeric surfaces with microbiocidal activity. Particularly the polymers containing QAC in the backbone or sidechains, such as chitosan [9, 10], *N*-alkyl polyethyleneimines [11, 12] and poly(4-vinyl-*N*-alkylpyridinium bromide) with alkyl chains shorter than six carbons [13–18], have been applied as bactericidal materials. The mechanism of their biocide action is well reported in the literature [14, 19–21]. The adsorption of bacteria onto cationic surfaces is driven by electrostatic interac-

*Corresponding author, e-mail: dfsp@iq.usp.br

tion between polymer cationic charges and the bacterial membranes negative charges (teichoic acids of Gram-positive bacteria and negatively charged phospholipids at the outer membrane of Gram-negative bacteria). Upon adsorbing, the compensation of the negative charges of the bacterial envelope is provided by the cationic charges of the substrate, and the bacteria lose their natural counter ions, which are released, increasing the entropic gain. Thus, solid substrate becomes biocidal when the number of cationic sites is large enough to remove counter ions from bacteria, inducing disruption of the bacteria envelope. Moreover, if the polycation chains have hydrophobic side chains, the disruption of outer and cytoplasmic membranes is favored.

Considering the demand for long-lasting antimicrobial coatings based on environmentally friendly and non-toxic products [22], blends of CMCAB and poly(4-vinyl-*N*-pentylpyridinium bromide), QPVP-C5, were prepared by casting in a broad composition range. The morphological structure, miscibility, thermal behavior and wettability were investigated by means of scanning electron microscopy (SEM), differential scanning calorimetry (DSC), thermogravimetric analysis (TGA) and contact angle measurements, respectively. Antimicrobial properties of neat CMCAB and CMCAB/QPVP-C5 blends against Gram-positive bacteria *Micrococcus luteus* were assessed by changes of microbial dispersions turbidity. Moreover, the ability to reduce the colony-forming units (CFU) of *Micrococcus luteus* and *Escherichia coli* was quantitatively evaluated for neat CMCAB and CMCAB/QPVP-C5 blends.

2. Experimental section

2.1. Materials

Carboxymethyl cellulose acetate butyrate (CMCAB-641-0.2) ($\overline{M}_n$ = 20 000 g·mol^{-1}; DS_{Ac} = 0.4; DS_{Bu} = 1.6 and DS_{CM} = 0.3), was kindly supplied by Eastman Chemical Co. (Brazil). The chemical structure of

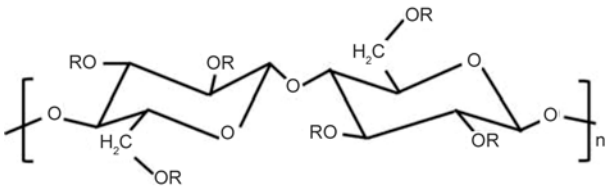

Figure 1. Representation of chemical structures of CMCAB, where R refers to H, $COCH_3$, COC_3H_7 and/or CH_2COOH

CMCAB is represented in Figure 1. Poly(4-vinylpyridine) (PVP, $\overline{M}_w$~ 60 000 g·mol^{-1}, degree of polymerization, *DP*, ~600) and 1-bromopenthane (purity 99%) were obtained from Sigma-Aldrich (Brazil), and anhydrous ethanol (98%), diethyl ether (99%) and HBr (48%) from Labsynth (Brazil). All reagents and solvents were used without previous purification. Gram-positive bacteria *Micrococcus luteus* (ATCC 4698) and Gram-negative bacteria *Escherichia coli* (ATCC25922) were purchased from Adolf Lutz Institute (Brazil).

2.2. Preparation of poly(4-vinyl-*N*-pentyl pyridinium bromide), QPVP-C5

Bromide salt of PVP quaternized with linear pentyl chains was prepared in a flask with a reflux condenser by dissolving PVP (10 wt%) in anhydrous ethanol, adding the 1-bromopentane with an excess of 5 times the stoichiometric amount and keeping the mixture stirring under nitrogen atmosphere for 24 h at 60°C [23, 24], as schematically represented in Figure 2. The mixture was then precipitated in diethyl-ether to obtain a slightly yellow solid that was re-dissolved in ethanol and re-precipitated the same way. The product was washed with a cold HBr 0.1 mol·L^{-1} solution in order to remove any eventual unreacted parts, washed with diethyl-ether once more, and dried under vacuum at room temperature. The effectiveness of the quaternization was evaluated by Fourier transform infrared (FTIR) vibrational spectroscopy observing the shift of the characteristic pyri-

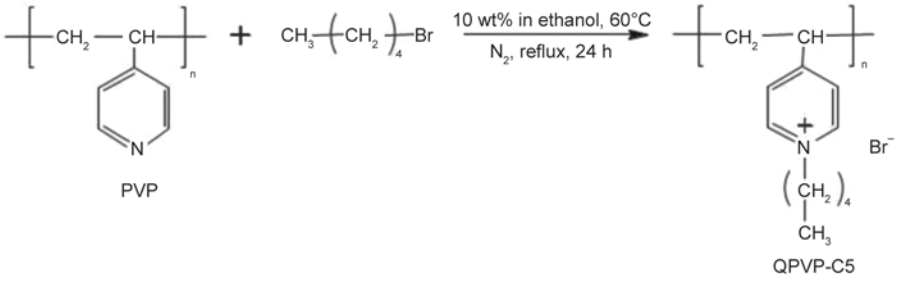

Figure 2. Schematic representation of quaternization of PVP with bromopentane

dine N–C stretching band from 1600 to 1640 cm^{-1}, which is typical for pyridinium cations. The band in 1600 cm^{-1} disappeared entirely, indicating complete quaternization. The resulting polycation was coded as QPVP-C5.

2.3. Preparation of CMCAB/QPVP-C5 blend films

CMCAB/QPVP-C5 blends were prepared by dissolving the polymers in ethanol (1 wt %), which is a good solvent for both polymers and casting the solutions (10 mL) in polyethylene (PE) dishes (4 cm diameter) at 50°C, during 24 h. PE dishes were chosen because when glass Petri dishes were used for polymer film formation, the adhesion to glass surface was so strong that impeached the films removal after drying. The weight fractions (x) of QPVP-C5 in the blends were 0; 0.17; 0.30; 0.50; 0.70 and 1.0.

2.4. Characterization

The CMCAB/QPVP-C5 blends films were analyzed by Fourier transform infrared vibrational spectroscopy (FTIR) in Bomem MB100 equipment, resolution of 4 cm^{-1}. The morphology of CMCAB/QPVP-C5 blends was analyzed by means of scanning electron microscopy with FE-SEM JEOL 7401 equipment. Cryofractured samples were coated with a thin (2 nm) gold layer prior to SEM analyses. Thermogravimetric analyses (TGA) of pure polymers and CMCAB/QPVP-C5 blends were carried out in TGA 2950 equipment (TA Instruments). Pt crucibles containing the samples were heated and cooled down at rate of 10°C·min^{-1}, ranging from 25 up to 500°C, under N_2 atmosphere (50 mL·min^{-1}). Glass transition temperature (T_g) of pure polymers and respective blends were determined by means of differential scanning calorimetry (DSC) in TA-DSC Q10V9.0 equipment. Each sample sealed in Al crucibles was heated and cooled down at rates of 15 and 20°C·min^{-1}, respectively, in the temperature range from 25 to 250°C under dynamic N_2 atmosphere (50 mL·min^{-1}). The DSC cell was calibrated with In (T_m = 157°C; ΔH_m = 28.54 J·g^{-1}) and Zn (T_m = 420°C). An empty crucible was used as reference. The second heating was considered for the determination of T_g values. Contact angle measurements were performed at (25±1)°C in a home-built apparatus [25]. Sessile drops of 8 μL Milli-Q water were used for the advancing contact angle (θ_a) measurements for pure polymers, QPVP-C5 and CMCAB, and CMCAB/QPVP-C5 blends films. Three samples of the same composition were analyzed at two different spots.

2.5. Determination of biocidal action

2.5.1. Monitoring the turbidity of *Micrococcus luteus* dispersions

The antimicrobial action of pure CMCAB, pure QPVP-C5, and CMCAB/QPVP-C5 blends was assessed by a standard assay for the determination of lysozyme activity, as described elsewhere [26]. Briefly, the initial turbidity (τ_i) of aqueous dispersions (pH 6) of *Micrococcus luteus* (ATCC 4698) at 0.5 mg·mL^{-1} was determined at 25°C and 650 nm, using Beckmann Coulter DU-600 spectrophotometer. Polymer films (22 cm^2) were dipped into the *M. luteus* dispersions and allowed to interact during 1 h. After this period of time the turbidity (τ_f) of bacteria dispersions was measured again. Since *M. luteus* is micrometer-sized and the disruption of bacteria envelope leads to decrease in size, antimicrobial activity can be correlated with the relative decrease of turbidity ($\Delta\tau$); the larger is $\Delta\tau$, the more efficient is the antimicrobial agent (Equation (1)):

$$\Delta\tau = \frac{\tau_i - \tau_f}{\tau_i} \cdot 100 \quad (1)$$

As a control experiment, ($\Delta\tau$) values were also measured after 1 h for aqueous dispersions of *M. luteus* (τ_i) in the absence of any polymer.

2.5.2. Determination of the minimum inhibitory concentration (MIC) and minimum bactericidal concentration (MBC) of QPVP-C5 for *Micrococcus luteus* and *Escherichia coli*

The minimum inhibitory concentration (MIC) and minimal bactericidal concentration (MBC) of QPVP-C5 for *E. coli* (ATCC 25922) and *M. luteus* (ATCC 4698) were determined in triplicates by the microdilution broth method in 96-well microplates, as recommended by the CLSI [27]. In brief, twofold serial dilutions of QPVP-C5 were prepared at final volume of 0.1 mL of Mueller-Hinton broth per well in a 96-well microtitre plates. The final concentration of the QPVP-C5 ranged from 6000 to 0.005 μg·mL^{-1}. Each well of the microtitre plate was inoculated with bacterial cell suspension to a final concentration of $5 \cdot 10^5$ CFU·mL^{-1} and the plates were incubated at 35°C for 16 to 20 hours in an ambient air

incubator. MIC was defined as the lowest concentration of QPVP-C5 that completely inhibited growth of the organism (lack of turbidity) in the microdilution wells. To determine the MBC, 10 µL aliquots were taken from selected wells that did not show visible bacterial growth and spread on plates containing Agar Muller-Hinton medium, being incubated for 24 hours at 37°C. Visual observation indicated presence or absence of growth and MBC endpoint was considered as the lowest concentration of QPVP-C5 solution showing no growth.

2.5.3. Colony forming units (CFU) count on CMCAB and CMCAB/QPVP-C5 blends

The antibacterial activity of CMCAB and CMCAB/QPVP-C5 blends, against *M. luteus* ATCC 4698 and *E. coli* ATCC 25922 was essentially determined as described in the JIS Z 2801:2000 standard [28]. An aliquot (400 µL) of a cell suspension of either *M. luteus* ATCC 4698 (10^5 CFU·mL^{-1}) or *E. coli* ATCC 25922 (10^6 CFU·mL^{-1}) was held in intimate contact with each of the 2 replicates of the test surfaces, i.e., CMCAB or CMCAB/QPVP (x = 0.7) films 22 mm of diameter, prepared using sterile 12-well flat bottom plates, for 24 hours at 37°C, under humid conditions. Next, the size of surviving bacterial populations was determined by viable cell counts on Trypticase Soy Agar, after incubation at 37°C for 24 hours of 0.1 mL sample taken from the test surfaces. A negative control experiment (without any bacteria) was also performed.

2.6. Quantification of QPVP-C5 leaching

The amount of QPVP-C5 leached during antimicrobial assays was evaluated by UV-Vis analyses following the same conditions used with bacteria dispersions. Polymeric blend films were dipped in distilled water and after 1 h the concentration of polycation was quantified in water by measuring the absorption intensity at λ = 258 nm using Beckmann Coulter DU-600 spectrophotometer. The amount of QPVP-C5 leached was determined through an analytical curve obtained from five different concentrations of specimen at the wavelength 258 nm, which is assigned to electronic transitions in the pyridinium ring due to the π → π* electronic transition.

3. Results and discussion

3.1. CMCAB/QPVP-C5 blends characterization

FTIR spectra obtained for all CMCAB/QPVP-C5 blends presented the typical absorption bands observed for the corresponding pure CMCAB and QPVP-C5 polymers (Figure 3), namely, the C=O stretch of cellulose ester at 1750 cm^{-1} and the pyridinium group at 1640 cm^{-1}. Considering that strong acid-base interactions can cause shifts of up to 30 cm^{-1} in the carbonyl and carboxylic acid bands [29], the spectra in Figure 3 indicate the absence of such interactions. Liu and Xiao characterized blends of konjac glucomannan gum [30] or chitosan [31] with QPVP-C4 by means of FTIR and other analytical techniques, which evidenced intermolecular interactions between the polymers in the both blends. Whereas in the first case the stretching vibration of –OH in comparison to the pure konjac glucomannan gum shifted gradually to higher wavenumbers as the amount of QPVP-C4 increased, in the latter the –NH_2 band of chitosan split in two denoting interaction with QPVP-C4.

The miscibility between CMCAB and QPVP-C5 was investigated by DSC analyses. The glass transition temperature (T_g) values determined for pure CMCAB, pure QPVP-C5 and blends are presented in the Table 1. DSC curves (Figure 4a) exhibited a sin-

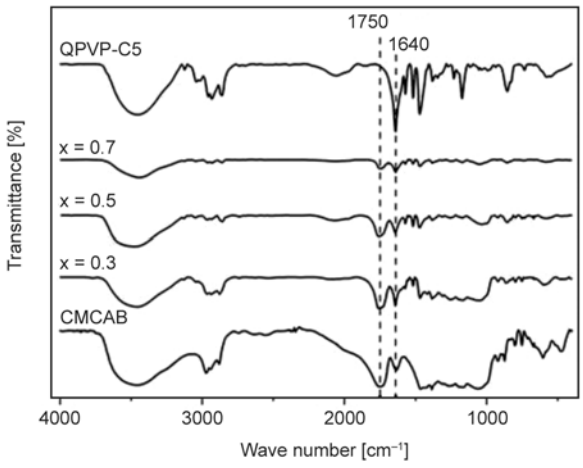

Figure 3. FTIR spectra of pure QPVP-C5 and CMCAB, and CMCAB/QPVP-C5 blends. '*x*' stands for the weight fraction of QPVP-C5 in the blend. The dashed lines indicate the typical absorbance bands of pyridinium group and C=O stretch of ester groups at 1640 and 1750 cm^{-1}, respectively.

Table 1. Experimental glass transition temperature (T_g), glass transition temperature calculated with Fox equation (T_g^F), contact angle (θ) values and turbidity decrease (Δτ) determined for pure CMCAB, pure QPVP-C5 and their blends. '*x*' stands for weight fraction of QPVP-C5 in the blends

Sample	x	T_g [K]	T_g^F [K]	θ [°]	Δτ [%]
QPVP-C5	–	350.6±0.5	–	*	96±2
CMCAB/QPVP-C5	0.7	351±1	364	**	66±5
CMCAB/QPVP-C5	0.5	370±1	380	**	52±2
CMCAB/QPVP-C5	0.3	370±1	389	65±3	30±2
CMCAB/QPVP-C5	0.17	–	–	69±4	10±1
CMCAB	–	419±1	–	71±2	3±1

Films were either (*) dissolved or (**) swollen by droplets of water.

gle T_g value, indicating miscibility of systems. The T_g value of miscible polymer blends can be estimated by the Fox equation (Equation (2)) [32]:

$$\frac{1}{T_g} = \frac{x_1}{T_{g1}} + \frac{x_2}{T_{g2}} \quad (2)$$

where x_1 and x_2 are the weight fraction of each polymer in the blend and T_{g1} and T_{g2} are the T_gs of polymer *a* and polymer *b*, respectively.

For all blends the experimental value of T_g was smaller than the predicted one, as presented in Figure 4b. The negative deviation from Fox equation indicates good miscibility between the two components [32]. Hydrophobic interactions between CMCAB butyl groups (DS_{Bu} = 1.64) and QPVP-C5 pentyl groups might possibly drive the miscibility between the polymers, since no shift in the C=O or pyridinium absorption bands could be observed in the FTIR spectra of blends in comparison to the spectra of pure polymers.

SEM images obtained for cryofractured films of pure CMCAB and QPVP-C5 (Figure 5a and 5b, respectively), and CMCAB/QPVP-C5 blends with x = 0.3; 0.5 and 0.7 (Figure 5c, 5d and 5e, respectively), showed homogeneous phases in all blends composition, corroborating with the DSC results. The images in the insets allow estimating the film thickness, which ranged from ~15 to ~50 μm.

The thermal stability of pure CMCAB and QPVP-C5 was investigated by means of thermogravimetric (TG) curves, as shown in Figure 6a. The events related to the polymers thermal behavior can be better identified in the derivatives weight loss (DTG) curves (Figure 6b). The TG and DTG curves obtained for CMCAB showed a weight loss stage with peak temperature at 355°C, which can be attributed to the thermal degradation of cellulose ester and corresponded to ~80% of initial weight. Between 420 and 500°C the weight remained constant, since the residual material (~15% of initial weight) was mainly ashes. The TG and DTG curves obtained for QPVP-C5 indicated three stages. The first one corresponding to ~10% weight loss at 59°C was attributed to the loss of ethanol molecules entrapped in the bulk material. The second and third stages with peak temperatures at 290 and 336°C, respectively, were attributed to the decomposition of QPVP-C5, remaining ~5% of initial weight as ashes.

The TG and DTG curves obtained for CMCAB/QPVP-C5 blends are presented in Figures 6c and 6d, respectively. The general trend is that the ther-

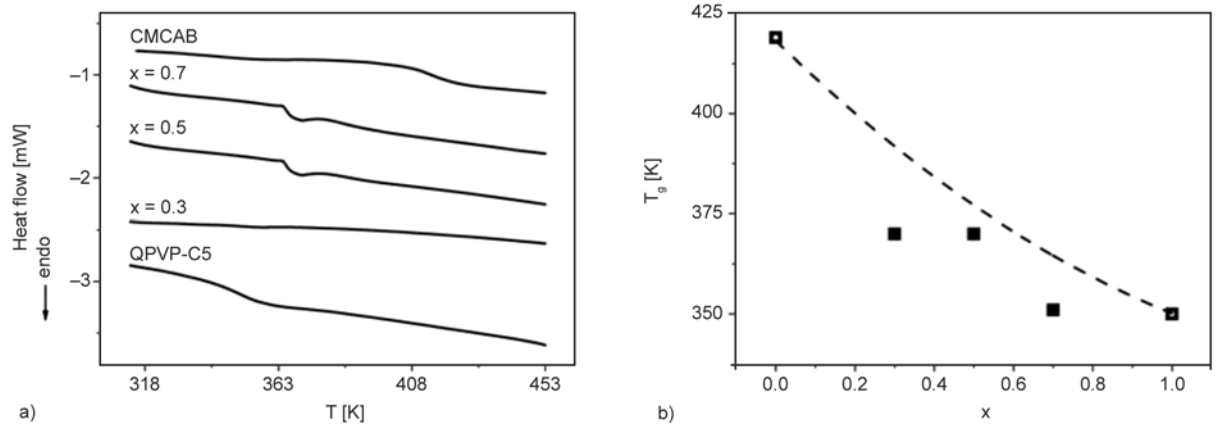

Figure 4. (a) DSC curves obtained for pure QPVP-C5, pure CMCAB, and CMCAB/QPVP-C5 blends. (b) Glass transition temperature (T_g) of pure QPVP-C5, pure CMCAB, and CMCAB/QPVP-C5 blends determined by DSC experiments (squares) and calculated (---) by Fox equation as function of weight fraction of QPVP-C5 in the blends (x).

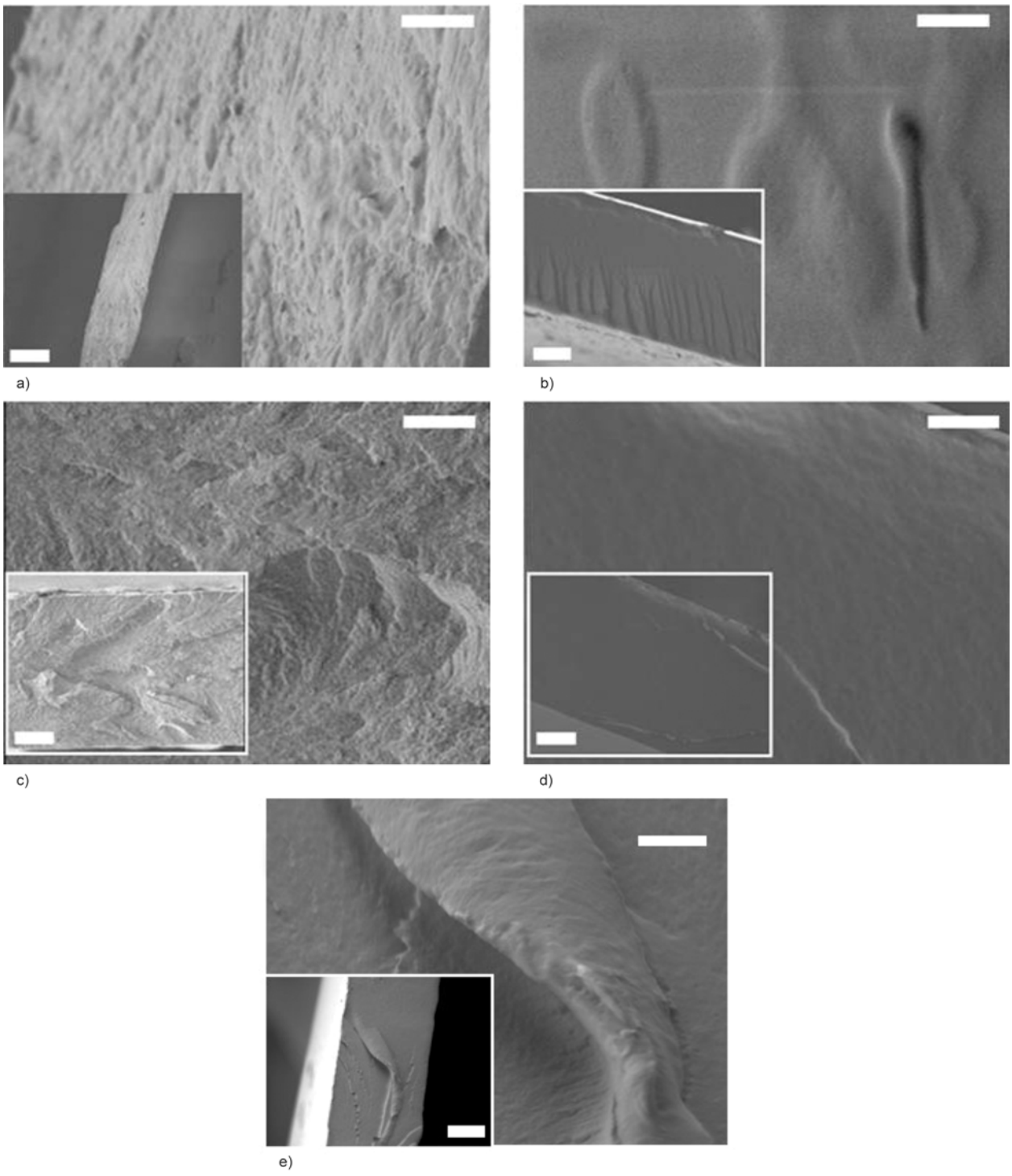

Figure 5. SEM images obtained for pure CMCAB (a), pure QPVP-C5 (b), CMCAB/QPVP-C5 blends with $x = 0.3$ (c), $x = 0.5$ (d) and $x = 0.7$ (e). The scales bars correspond to 2 μm. The scale bars in the insets correspond to 10 μm.

mal stability of the blends was inferior to that of pure CMCAB, but superior to that of pure QPVP-C5. It implies that the thermal stability of QPVP-C5 is enhanced due to the introduction of the CMCAB. A similar behavior was observed for blends of QPVP-C4/ konjac glucomannan, where the polysaccharide enhanced the blends thermostability [30].

3.2. Antimicrobial activity of CMCAB/QPVP-C5 blends

In general polycations are biocidal polymers, but the structural characteristics such as molecular weight, type and degree of alkylation, and distribution of charge affect the antimicrobial action [33]. For instance, the antimicrobial activity of poly(4-vynil-

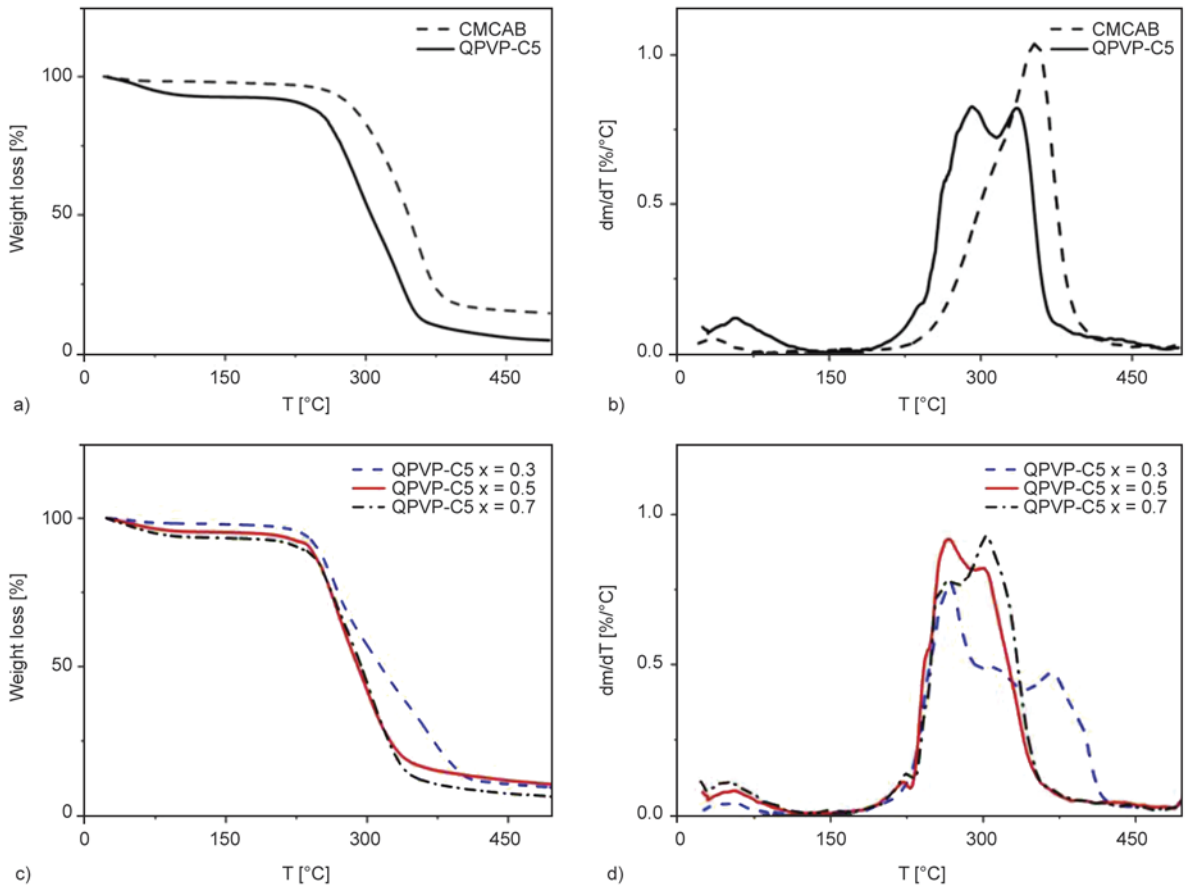

Figure 6. TG (a) and DTG (b) curves determined for pure CMCAB (dash line) and QPVP-C5 (solid line). TG (c) and DTG (d) curves obtained for CMCAB/QPVP-C5 blends with $x = 0.3$ (dash line), 0.5 (solid line) and 0.7 (dash/dot line).

N-alkyl pyridinium) bromide decreases for alkyl side group larger than C6 [13]. The reason for this is a tilt in the geometry; when the alkyl chain is 6 carbons long or shorter, the dihedral angle is 0 or 180°, *i.e.* all the atoms lie in the same plane [24]. From the seventh atom forward the alkyl chain becomes crooked making a dihedral angle different from 0 or 180° [24], shielding the positive charge.

The MIC and MBC of QPVP-C5 for both *M. luteus* and *E. coli* amounted to 11.7 $\mu g \cdot mL^{-1}$. Such low concentration values indicated that QPVP-C5 has outstanding biocidal properties.

The bactericidal activity of pure CMCAB, pure QPVP-C5 and CMCAB/QPVP-C5 blends was correlated to the relative decrease of turbidity ($\Delta\tau$) of *M. luteus* aqueous dispersion. Table 1 shows the $\Delta\tau$ values measured after interacting during 1 h with each polymeric film. In the case of pure QPVP-C5, chains dissolved in aqueous dispersion, presenting maximal $\Delta\tau$ values (96±2%), which is in agreement with studies previously reported [16]. The $\Delta\tau$ values measured for the CMCAB/QPVP-C5 blends decreased with the decrease of QPVP-C5 content in the blends. The best antimicrobial effect was observed for the films of CMCAB/QPVP-C5 $x = 0.7$, with $\Delta\tau = 66\pm5\%$. In other words, the lower was the polycation content in the blends, the less bactericidal was the film. Additionally, the UV-Vis analysis indicated that the amount of leached QPVP-C5 was less than 1.5% of original amount used in the blend preparation, which corresponded to less than 15 $\mu g \cdot mL^{-1}$. Considering that it is very close to the MIC and MBC found for QPVP-C5 against *M. luteus* and *E. coli* (11.7 $\mu g \cdot mL^{-1}$), the biocidal properties of CMCAB and CMCAB/QPVP-C5 ($x = 0.7$) films were determined directly on the polymer. The CFU reduction was quantitatively determined for *M. luteus* and *E. coli* after 24 h, as shown in Table 2. Against *M. luteus* neat CMCAB presented a modest 2 log reduction, while the blend presented a remarkable 5 log reduction. Against *E. coli* neat CMCAB had no biocidal activity, the CFU increased 1 log; however, the CMCAB/QPVP-C5 ($x = 0.7$) films caused 4 log CFU reduction, evidencing the out-

Table 2. CFU reduction determined for *M. luteus* and *E. coli* after 24 h contact with CMCAB and CMCAB/QPVP-C5 ($x = 0.7$) films

	***Micrococcus luteus* ATCC 4698 [CFU/mL]**			
	0 h	**24 h**	**log CFU reduction**	**% reduction**
CMCAB	$1 \cdot 10^5$	$5.75 \cdot 10^3$	2	94.25
CMC/QPVP-C5 ($x = 0.7$)	$1 \cdot 10^5$	0	5	>99.9
Control	0	0		
	***Escherichia coli* ATCC 25922 [CFU/mL]**			
	0 h	**24 h**	**log CFU reduction**	**% reduction**
CMCAB	$1.0 \cdot 10^6$	$6.7 \cdot 10^7$	–	–
CMC/QPVP-C5 ($x = 0.7$)	$1.0 \cdot 10^6$	$7 \cdot 10^2$	4	>99.9
Control	0	0		

standing biocidal properties for Gram-positive and Gram-negative bacteria.

In order to gain insight about the orientation of pyridinium groups on the CMCAB/QPVP-C5 films, contact angle values (θ) were measured for pure CMCAB and blends with $x = 0.17$ and 0.30 of QPVP-C5, as presented in Table 1. The θ values decreased from (71±2)° for pure CMCAB to (65±3)° for blends with $x = 0.30$, indicating a slight increase in the wettability with increasing QPVP-C5 content in the blend. It was not possible to measure the contact angles for blends with $x \geq 0.5$ because the films became swollen by water droplets, invalidating the method. This behavior corroborates with the trend observed for the biocidal activities and supports the idea that upon increasing the QPVP-C5 content in the blends, the pyridinium groups tend to enrich the film surface.

4. Conclusions

Miscible blends of CMCAB/QPVP-C5 were prepared in ethanol, a good solvent for both polymers. The thermal stability of CMCAB/QPVP-C5 blends was superior to that of pure QPVP-C5. Upon increasing the content of QPVP-C5 in the blend, the surface wettability and antimicrobial properties against *M. luteus* and *E. coli* were favored, indicating surface enrichment by pyridinium groups. For practical purposes, CMCAB/QPVP-C5 blends could be co-extruded with polyolefins, polystyrene, poly(methyl methacrylate), providing new materials with antimicrobial activity and good thermal stability, which can be used to manufacture daily items, like keyboards, doorknobs, handles, grips for supermarket trolleys and baskets, with protection against microbial infections transmitted by contact.

Acknowledgements

The authors acknowledge the Brazilian funding agencies CAPES Rede-NANOBIOTEC, CNPq and FAPESP for financial support.

References

[1] Edgar K. J., Buchanan C. M., Debenham J. S., Rundquist P. A., Seiler B. D., Shelton M. C., Tindall D.: Advances in cellulose ester performance and application. Progress in Polymer Science, **26**, 1605–1688 (2001).
DOI: 10.1016/S0079-6700(01)00027-2

[2] El-Sakhawy M., Kamel S., Salama A., Sarhan H-A.: Carboxymethyl cellulose acetate butyrate: A review of the preparations, properties, and applications. Journal of Drug Delivery, **2014**, 575969/1–575969/6 (2014).
DOI: 10.1155/2014/575969

[3] Obie R.: Improving holdout. US Patent 7026470 B2, USA (2006).

[4] Amim Jr. J., Petri D. F. S.: Effect of amino-terminated substrates onto surface properties of cellulose esters and their interaction with lectins. Materials Science and Engineering: C, **32**, 348–355 (2012).
DOI: 10.1016/j.msec.2011.11.004

[5] Amim Jr. J., Petri D. F. S., Maia F. C. B., Miranda P. B.: Ultrathin cellulose ester films: Preparation, characterization and protein immobilization (in Portuguese). Química Nova, **33**, 2064–2069 (2010).
DOI: 10.1590/S0100-40422010001000011

[6] Dallas P., Sharma V. K., Zboril R.: Silver polymeric nanocomposites as advanced antimicrobial agents: Classification, synthetic paths, applications, and perspectives. Advances in Colloid and Interface Science, **166**, 119–135 (2011).
DOI: 10.1016/j.cis.2011.05.008

[7] Knetsch M. L. W., Koole L. H.: New strategies in the development of antimicrobial coatings: The example of increasing usage of silver and silver nanoparticles. Polymers, **3**, 340–366 (2011).
DOI: 10.3390/polym3010340

[8] Melo L. D., Palombo R. R., Petri D. F. S., Bruns M., Pereira E. M .D., Carmona-Ribeiro A. M.: Structure–activity relationship for quaternary ammonium compounds hybridized with poly(methyl methacrylate). ACS Applied Materials and Interfaces, **3**, 1933–1939 (2011).
DOI: 10.1021/am200150t

[9] Vieira D. B., Lincopan N., Mamizuka E. M., Petri D. F. S., Carmona-Ribeiro A. M.: Competitive adsorption of cationic bilayers and chitosan on latex: Optimal biocidal action. Langmuir, **19**, 924–932 (2003).
DOI: 10.1021/la026102f

[10] Goy R. C., de Britto D., Assis O. B. D.: A review of the antimicrobial activity of chitosan (in Portuguese). Polímeros, **19**, 241–247 (2009).
DOI: 10.1590/S0104-14282009000300013

[11] Wong S. Y., Li Q.,Veselinovic J., Kim B-S., Klibanov A. M., Hammond P. T.: Bactericidal and virucidal ultrathin films assembled layer by layer from polycationic *N*-alkylated polyethylenimines and polyanions. Biomaterials, **31**, 4079–4087 (2010).
DOI: 10.1016/j.biomaterials.2010.01.119

[12] Haldar J., An D., De Cienfuegos L. Á., Chen J., Klibanov A. M.: Polymeric coatings that inactivate both influenza virus and pathogenic bacteria. Procedings of the National Academy of Science of the United States of America, **103**, 17667–17671 (2006).
DOI: 10.1073/pnas.0608803103

[13] Tiller J. C., Liao C-J., Lewis K., Klibanov A. M.: Designing surfaces that kill bacteria on contact. Procedings of the National Academy of Science of the United States of America, **98**, 5981–5985 (2001).
DOI: 10.1073/pnas.111143098

[14] Kügler R., Bouloussa O., Rondelez F.: Evidence of a charge-density threshold for optimum efficiency of biocidal cationic surfaces. Microbiology, **151**, 1341–1348 (2005).
DOI: 10.1099/mic.0.27526-0

[15] Gozzelino G., Lisanti C., Beneventi S.: Quaternary ammonium monomers for UV crosslinked antibacterial surfaces. Colloids and Surfaces A: Physicochemical and Engineering Aspects, **430**, 21–28 (2013).
DOI: 10.1016/j.colsurfa.2013.03.061

[16] Silva R. A., Urzúa M. D., Petri D. F. S.: Lysozyme binding to poly(4-vinyl-*N*-alkylpyridinium bromide). Journal of Colloid and Interface Science, **330**, 310–316 (2009).
DOI: 10.1016/j.jcis.2008.10.087

[17] Amim Jr. J., Maia C. B. F., Miranda P. B., Urzúa M. D., Petri D. F. S.: Structural aspects of polyanion and hydrophobically modified polycation multilayers on hydrophilic or hydrophobic surfaces. Soft Matter, **8**, 6462–6470 (2012).
DOI: 10.1039/c2sm25658d

[18] Blachechen L. S., Fardim P., Petri D. F. S.: Multifunctional cellulose beads and their interaction with gram positive bacteria. Biomacromolecules, **15**, 3440–3448 (2014).
DOI: 10.1021/bm5009876

[19] Siedenbiedel F., Tiller J. C.: Antimicrobial polymers in solution and on surfaces: Overview and functional principles. Polymers, **4**, 46–71 (2012).
DOI: 10.3390/polym4010046

[20] Muñoz-Bonilla A., Fernández-García M.: Polymeric materials with antimicrobial activity. Progress in Polymer Science, **37**, 281–339 (2012).
DOI: 10.1016/j.progpolymsci.2011.08.005

[21] Muñoz-Bonilla A., Cerrada M. L., Fernández-Garcia M.: Polymeric materials with antimicrobial activity: From synthesis to applications. The Royal Society of Chemistry, Cambridge (2013).

[22] Simal-Gándara J.: Selection of can coatings for different applications. Food Reviews International, **15**, 121–137 (1999).
DOI: 10.1080/87559129909541180

[23] Urzúa M. D., Ríos H. E.: Adsorption of poly(4-vinylpyridine) *N*-alkyl quaternized at the chloroform/water interface. Polymer International, **52**, 783–789 (2003).
DOI: 10.1002/pi.1148

[24] Oliveira A. M., Miranda P. B., Petri D. F. S.: Self-assembly of poly(4-vynil-*N*-alkylpyridinium) bromide onto silica: Effect of side-chain length on structural aspects at a molecular level. The Journal of Physical Chemistry C, **116**, 18284–18291 (2012).
DOI: 10.1021/jp305606k

[25] Adamson W. A.: Physical chemistry of surfaces. Wiley, Toronto (1980).

[26] Bergmeyer H. U., Bergmeyer J., Graßl M.: Methods of enzymatic analysis. Verlag Chemie, Weinheim (1984).

[27] Clinical and Laboratory Standards Institute: Methods for dilution antimicrobial susceptibility tests for bacteria that grow aerobically; Approved standard-Tenth edition. CLSI document M07-A10, Wayne, USA (2015).

[28] Japanese Industrial Standard JIS Z 2801:2000. Antimicrobial products-Test for antimicrobial activity and efficacy (2000).

[29] Riaz U., Ashraf S. M.: Characterization of polymer blends with FTIR spectroscopy. in 'Characterization of polymer blends: Miscibility, morphology and interfaces' (eds.: Thomas S., Grohens Y., Jyotishkumar P.) Wiley, Weinheim, Vol 2, 509–538 (2014).

[30] Liu C., Xiao C.: Characterization of konjac glucomannan–quaternized poly(4-vinyl-*N*-butyl) pyridine blend films and their preservation effect. Journal of Applied Polymer Science, **93**, 1868–1875 (2004).
DOI: 10.1002/app.20646

[31] Liu C., Xiao C.: Characterization of films from chitosan and quaternized poly(4-vinyl-*N*-butyl) pyridine solutions. Journal of Applied Polymer Science, **92**, 559–566 (2004).
DOI: 10.1002/app.20040

[32] Hiemenz P. C., Lodge T. P.: Polymer chemistry. CRC Press, Boca Raton (2007).

[33] Timofeeva L., Kleshcheva N.: Antimicrobial polymers: Mechanism of action, factors of activity, and applications. Applied Microbiology and Biotechnology, **89**, 475–492 (2011).
DOI: 10.1007/s00253-010-2920-9

eXPRESS Polymer Letters Vol.9, No.9 (2015) 799–808
Available online at www.expresspolymlett.com
DOI: 10.3144/expresspolymlett.2015.75

Mussel-mimetic self-healing polyaspartamide derivative gel via boron-catechol interactions

*B. Wang, Y. S. Jeon, H. S. Park, Y. J. Kim, J-H. Kim**

School of Chemical Engineering, Sungkyunkwan University, Suwon 440-746, Korea

Received 4 February 2015; accepted in revised form 20 April 2015

Abstract. The catechol group from catechol of 3,4-dihydroxyphenethylamine (DOP, dopamine) has the ability to interact with metal ions to form non-covalent bonds in polymer chains. In this study, a novel kind of mussel-inspired copolymer, dopamine-conjugated poly(hydroxyethyl aspartamide), polyAspAm(DOP/EA), was synthesized and its interaction with boric acid (H_3BO_3) to form a cross-linked gel via boron-catechol coordinative binding was investigated. The copolymer was designed to contain a pH responsive adhesive catechol group, which reversibly underwent gelation through the metal-catechol binding, as proved by UV-Vis spectroscopy. When the pH is increased from acidic conditions to a specified pH (pH > 9), the $B(OH)_3$ is considered to have a functionality of two to bind catechols, leading to bis-complexes. In addition, the reversibility of the boron-catechol bonds provides self-healing characteristics to the polyAspAm gels. The rheological results showed that boron-catechol coordination could lead to quick and full recovery after the fracture of a gel specimen. This novel pH-responsive and self-healing gel system has potential in various applications including smart hydrogels, medical adhesives, and sealants.

Keywords: *polymer gels, self-healing, polyaspartamide, boron-catechol interactions*

1. Introduction

Bio-inspired polymers and soft gel-like materials have been extensively reviewed as novel materials for various applications due to their specific functionality and desirable mechanical properties with dynamic bonding interactions [1, 2]. Marine mussels withstand high-energy wave impacts in rocky seashore habitats by fastening tightly to surfaces with tough and self-healing proteinaceous fibers called byssal threads, which are heavily decorated with DOPA, a catecholic functionality [3, 4]. Covalent bonding or non-covalent interactions (such as hydrogen bonding [5, 6], π-π interactions [7], metal-ligand coordination bonding [8–10], or guest-host interactions [11] can form soft three-dimensional polymeric network hydrogels, which are defined as chemical gels or physical gels, respectively. In covalent hydrogels, it is difficult to induce a sol-gel transition in response to external stimuli or provide a self-healing mechanism. In contrast, non-covalent hydrogels can easily respond to the external environment, however, they have poor mechanical properties. Unlike covalent bonds, which are generally irreversible, metal coordination bonds in byssal threads have the capability of reforming after rupture [9, 12]. Thus, mussel-inspired, self-healing materials can be designed, which possess the ability to heal mechanical failure after rupture. Currently there are lots of reports considering self-healing hydrogel based on dynamic crosslinkage. Zhang *et al*. [13] presented an inexpensive, simple, and rapid method to prepare dynamic hydrogels using chitosan and telechelic PEG as main components which can control the release of drugs and other bioactive macromole-

*Corresponding author, e-mail: kimjh@skku.edu

cules. An inexpensive and biocompatible self-healing hydrogel for injectable cell therapy carrier was also investigated by Yang *et al*. [14]. Recently, some significant work has focused on non-covalent hydrogels, which are cross-linked by reversible interactions based on metal-ligand coordination in the polymer chains; these can provide stimuli responsiveness, magnetic self-healing and good mechanical properties [8–10, 15–20]. Because of the thermodynamics and kinetic properties of metal-ligand coordination bonds, metal-ligand interactions can provide stable, reversible crosslinking points between polymers [21]. Recently, some researchers reported mussel-inspired stimuli responsive and self-healing hydrogels containing dynamic metal (Fe^{3+})-catechol interactions. The hydrogels are pH-sensitive, i.e., the Fe^{3+} mono-catecholate, bis-catecholate, or tris-catecholate complexes are formed when the pH is increased to a specified pH [21, 22–25]. Krogsgaard *et al*. [9] reported a self-healing multi-responsive system by incorporating additional features of the mussel adhesive proteins for drug delivery platforms. They found that the catechol-Fe^{3+} complexes worked as cross-links and a sufficient number of cross-links formed a hydrogel. Competition between oxidation and coordination in catechol groups were investigated by Xu *et al.* [4]. They designed a simple polystyrene copolymer containing catechol groups to show that catechol units could afford a dual cross-linking system based on oxidative coupling with oxygen or coordinative coupling through Fe^{3+} [4].

Boric acid is a typical Lewis acid, which has several unique characteristics for biomedical applications [26]. In aqueous media, the Lewis acidity of boron facilitates the reaction with water to abstract OH^-, and the trigonal boron is converted to an anionic tetrahedral geometry [26]. Because the pKa value of boric acid is 4.5–10, anionic tetrahedral boron formed by reaction of the neutral boric acid with a diol of catechol is generally considered hydrolytically unstable [27–29]. In aqueous systems, boric acids maintain equilibrium between an undissociated neutral trigonal form and a dissociated anionic tetrahedral form [28]. Upon increasing the pH to the normal pKa value range of boric acid, $B(OH)_3$ is considered to have a functionality of two to bind catechols, leading to bis-complexes. Vatankhah-Varnoosfaderani synthesized and characterized a mussel-inspired copolymer, poly(dopamine methacrylate-co-*N*-isopropylacrylamide) [p(DMA-co-NIPAM)], and its interaction with boric acid (H_3BO_3) [30]. The supramolecular polymer gel was sensitive to three different external stimuli and a rapid self-healing property based on boron-catechol interactions was demonstrated. Other research groups also developed artificial stimuli-responsive gels, including pH-responsive [29–33] and sugar-responsive [34] polymer gels via boric-catechol complexation for biomaterials applications.

In this study, we present a pH-responsive self-healing hydrogel, inspired by adhesive mussel proteins, based on 3,4-dihydroxyphenethylamine(or dopamine)-conjugated polyaspartamide. Polyaspartamides are water-soluble, non-toxic, non-antigenic and biodegradable polymers, and can be obtained from the aminolysis of polysuccinimide (PSI), which is easily prepared by thermal polycondensation of D,L-aspartic acid, the thermal polycondensation product of aspartic acid monomer [35–39]. By using boric acid (H_3BO_3), the mussel-inspired copolymer exhibited a reversible gelation by pH change, which was based on boron-catechol coordination binding. In addition, the dynamic complexation between boron-catechol coordination can lead to the formation of a rapid self-healing smart material. Hence, this novel biocompatible gel system has potential in several applications including smart hydrogels, medical adhesives, and sealants.

2. Experimental

2.1. Materials and instruments

L-aspartic acid (98+%), ortho-phosphoric acid (98%), *N*,*N*-dimethylformamide (99.8% anhydrous, DMF), dopamine hydrochloride (DOP), ethanolamine (99%, EA), triethylamine (99.5+%), sodium hydrosulfite (~85%), acetic acid (99+%), and boric acid (99.5%+) were purchased from Aldrich Chemical Co. Acetone was obtained from DaeJung Chemical Co. (Siheung, Korea). All other chemicals purchased were of sufficient quality and used as received.

The ^{1}H NMR spectra were recorded on a Unity Inova-500 (Varian, Palo Alto, CA, USA) spectrometer using DMSO and D_2O as the solvents. The structures of the PolyAspAm samples were analyzed by Fourier transform infrared (FT-IR) spectroscopy (Bruker IFS 66/S, Bruker, Germany). UV-Vis absorption data were recorded on a Molecular Devices SpectraMax M5 spectrometer (California, USA) using a quartz cuvette with a path length of 1 cm at room temperature. Solutions of 20 mg/mL PolyAs-

pAm(DOP50/EA50) with a sufficient amount of $B(OH)_3$ solution (catechol/$B(OH)_3$ mole ratio = 2.0) were prepared. The pH of the solutions was then increased by the addition of a NaOH solution under a nitrogen blanket followed by stirring for 12 h and dilution of the solutions with different pH buffers.

2.2. Synthesis of polysuccinimide (PSI)

L-aspartic acid (30 g) and 98% ortho-phosphoric acid (30 g) (50:50 wt. ratio) were put into a round bottom flask and mixed at room temperature. The mixture was heated slowly from room temperature to 180°C under reduced pressure in about 30 min, and maintained at 180°C for 4.5 h. Then, the reaction mixture was cooled, and DMF was added to dissolve the product. The resulting solution was precipitated in excess water, and the precipitate was washed several times with water to remove the residual phosphoric acid until the solution reached pH = 7. The product was finally dried at 70°C in vacuum for 3 days to obtain PSI in a white powder form. The molecular weight was estimated to be approximately 130 000 Da, as calculated from an empirical equation relating the solution viscosity to the molecular weight [40].

2.3. Synthesis of polyaspartamide derivatives, polyAspAm(DOP/EA)

To synthesize polyAspAm(DOP/EA), 1 g of PSI was dissolved in 30 mL of DMF in a three-neck round-bottom flask, and 0.790 g of DOP (50 mol% based on succinimide unit) and 1.723 mL of triethylamine were subsequently added. The flask was placed in an oil bath maintained at 80°C, and the reaction was carried out under a nitrogen atmosphere for 24 h in the presence of 0.05 g sodium hydrosulfite to prevent oxidation of dopamine groups. A 50 mol% excess (0.528 mL) of EA was then added slowly to the reaction mixture, and the mixture was stirred at room temperature for another 24 h. The resulting mixture was precipitated in 500 mL of cold acetone. The filtered product, polyAspAm(DOP/EA), was dissolved in water, and glacial acetic acid was added until the solution pH reached pH 4. The final polymer solution was dialyzed for 3 days and lyophilized.

2.4. Gelation of polyAspAm(DOP/EA) with boric acid

The polyAspAm(DOP/EA) polymers with different catechol group concentrations were used for the preparation of aqueous solutions and reversible gels. As an example, 0.1 g polyAspAm (DOP50/EA50) was dissolved in 0.5 mL deionized water, into which a sufficient amount of $B(OH)_3$ solution (catechol/$B(OH)_3$ mole ratio = 2.0) was added. The pH of the mixtures was increased to the desired final pH of 9 by the addition of a 0.1 N NaOH solution under a nitrogen blanket. The mixture was mechanically mixed to produce gel via boron-catechol coordination binding.

2.5. Rheological properties

The rheological measurements of the polyAspAm gel were conducted on a Bohlin rotational rheometer (Malvern Instruments, U.K.) with parallel plate geometry of 20 mm diameter. Oscillatory shear testing of gels as a function of frequency was performed at constant strain of 1% to measure elastic modulus (G'), viscous modulus (G'') and complex viscosity at 25°C. Self-healing tests were performed by straining each gel to failure under increasing strain from 0.1% to 1000%, then using time sweep test to monitor the recovery G', G'' as a function of time.

3. Results and discussion

3.1. Synthesis and characterization of polyAspAm(DOP/EA)

As shown in Figure 1, novel dopamine-modified polyAspAm derivatives were synthesized from PSI through a successive aminolysis reaction with quantitative dopamine and excess EA. The structure and composition of the PSI and polyAspAm(DOP/EA) were confirmed using ^{1}H NMR spectroscopy (Figure 2). The methine proton (at 5.3 ppm) of the initial succinimide ring disappeared completely after a series of aminolysis reactions, suggesting a quantitative ring-opening to produce the polyAspAm derivatives. Peaks **a**, **b** and **c** were assigned to the aromatic protons of the dopamine phenyl group, and peaks **e** and **f** were assigned to the methylene protons of the EA pendant, respectively. The composition of each group in the polyAspAm(DOP/EA) copolymer was determined from the integration ratio between peaks **a**, **b**, **c** (δ = 6.3–6.8), and **d** (δ = 2.7). Table 1 shows the composition of three different polyAspAm(DOP/EA) copolymers prepared.

Figure 3 shows the FT-IR transmittance spectra of PSI (spectrum a) and polyAspAm(DOP50/EA50) (spectrum b). Spectrum a of PSI showed two characteristic bands at 1727 and 1393 cm^{-1}, which were

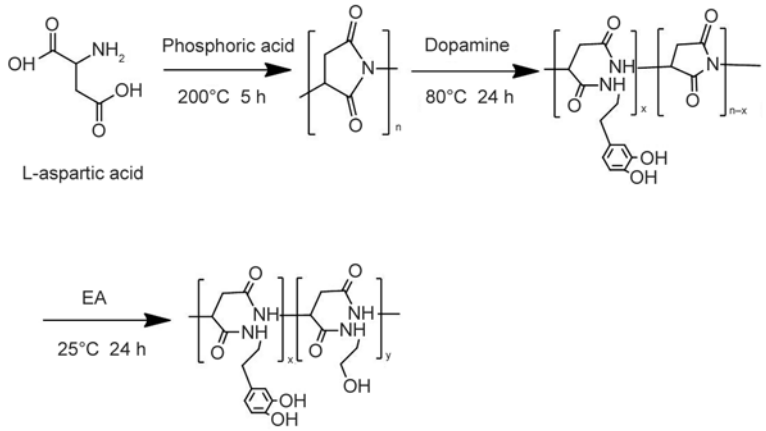

Figure 1. Reaction scheme for polyAspAm(DOP/EA) synthesis

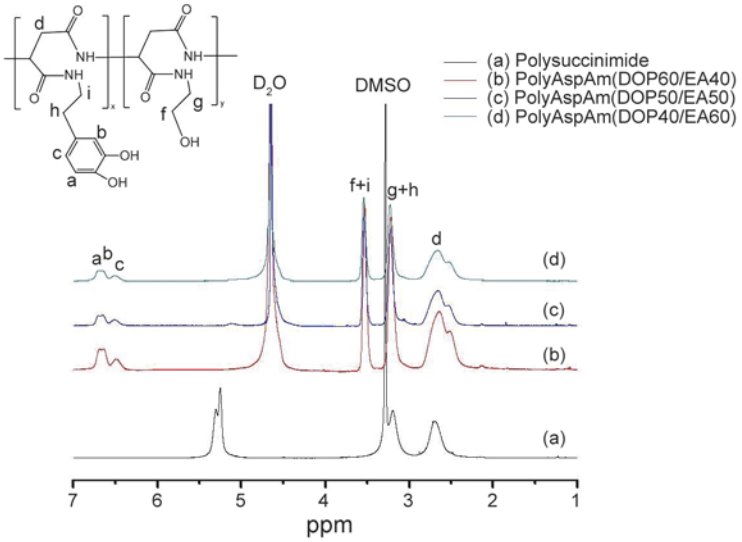

Figure 2. [1]H NMR spectra of dopamine-conjugated polyAspAm derivatives

Table 1. Composition of each pendant group in the polyAspAm(DOP/EA) copolymers

Content [mol%]	PolyAspAm(DOP40/EA60)	PolyAspAm(DOP50/EA50)	PolyAspAm(DOP60/EA40)
Dopamine	22	25	27
Ethanolamine	78	75	73

The proportion of each pendant group in the polyAspAm(DOP/EA) copolymers was determined by [1]H NMR analysis

attributed to the absorption of the imide ring. In the spectrum of b, the peaks relating to succinimide disappeared and new peaks relating to amide I and amide II bands at 1635.4 and 1519.4 cm^{-1}, respectively, are seen. The absorption bands of 1365.7 and 1281.5 cm^{-1} could be assigned to phenolic C–O–H of catechol groups in the dopamine. The broad band in the range of 3500–3200 cm^{-1} was assigned to –OH and –NH of the copolymer. As a result, both [1]H NMR and FT-IR analyses confirmed the successful synthesis of polyAspAm derivatives with dopamine pendants.

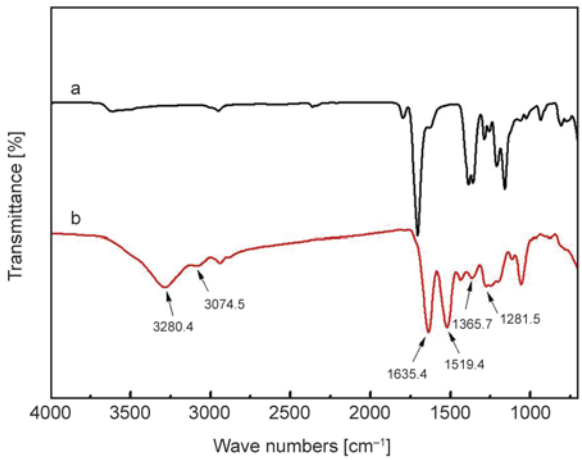

Figure 3. FT-IR Spectra of PSI (a) and polyAspAm(DOP/EA) (b)

3.2. Preparation and characterization of polyaspartamide derivative gels based on boron-catechol interactions

3.2.1. pH-responsive gelation

Boric acid, $B(OH)_3$, is a typical Lewis acid, which is dissolved in water to generate a weak electrolyte. Hydrated boric acid generates a small amount of ionizing $B(OH)_4^-$ and H^+ ions, and the resulting solution is weakly acidic. $B(OH)_3$ is known to be capable of forming complexes with catechol and substituted catechols [41]. Figure 4 shows the general overall reactions with both an addition (one ligand donor atom was present in a non-occupied site on boron) and a substitution reaction (the second ligand donor atom displacing an OH^- from boron). The boron atom has four coordinative bonds with diols from catechol groups, the ligand being bidentate.

Figure 5 shows the pH effect on the gelation of polyAspAm gel, where the polyAspAm(DOP50/EA50) copolymer was treated with boric acid ($B(OH)_3$/DOP = 1:2 molar ratio, 25 mg/mL of the polyAspAm) at different pH values of 8, 9 and 12, respectively. At pH 8, the polyAspAm solution containing boron exists in a liquid state with a yellow color, suggesting that $B(OH)_3$ formed catechol-boron monocomplexes (Figure 5a). When the pH was increased from acidic conditions to a specified pH of pH = 9, the $B(OH)_3$ was considered to have a functionality of two to bind catechols to form non-covalent crosslinking via boron-catechol coordinative complexation.

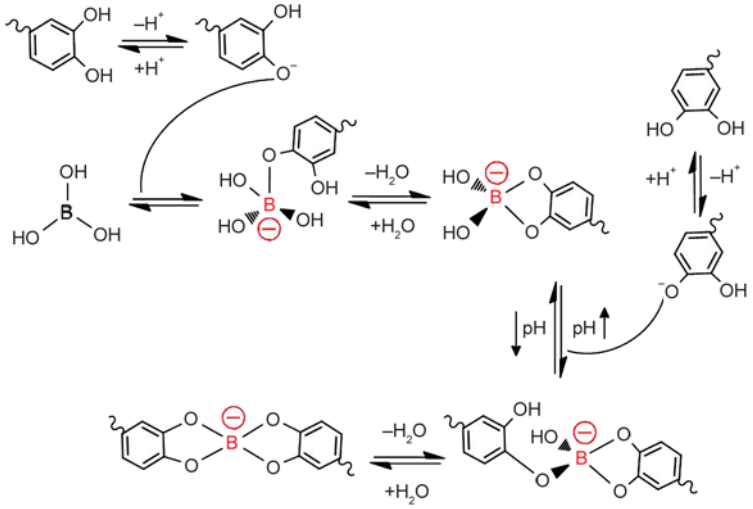

Figure 4. Equilibrium reaction between catechol groups of polyAspAm(DOP/EA) and boric acid

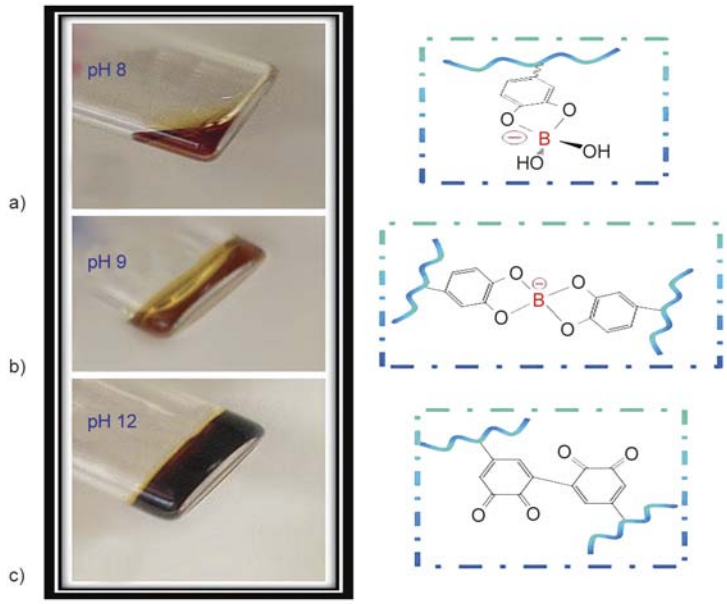

Figure 5. Photographs of polyAspAm(DOP/EA) with boric acid gel at different pH conditions. The physical state, color, and estimated chemical interactions of polyAspAm(DOP/EA) with $B(OH)_3$ at pH values of (a) 8, (b) 9 and (c) 12 were demonstrated

In addition, the color changed to the characteristic dark red (Figure 5b). At a higher pH of 12, it seemed catechol quinone-mediated covalent coupling had occurred to form a permanently cross-linked dark brown gel (Figure 5c) caused by the possible oxidation of catechol groups.

Further evidence of the presence of catechol-$B(OH)_3$ complexes was gained from UV-vis spectroscopic measurements. Figure 6a showed the dominance of catechol-$B(OH)_3$ complexes under different pH conditions. When the solution is acidic, boric acid does not interact with catechol groups, showing the same spectra as that of a pure polyAspAm copolymer solution with only one peak (λ_{max} = 280 nm), assignable to the catechol group. However, boron-catechol bonds are formed when the pH of the solution is increased to pH 9, as the corresponding absorption is shown at 490 nm. The peak at 320–330 nm, appearing in alkaline condition, is related to the oxidation of catechol groups that is not avoidable. When the solution pH was decreased from pH 9 to pH 8, the peak at 490 nm disappeared due to the reversible boron-catechol interactions. Figure 6b-1 showed the gel formed from catechol-$B(OH)_3$ at pH 9. It was transited to a liquid after adjusting the pH to 5 (Figure 6b-2). When the pH is increased from 5 to a specified pH = 9, the gelation occurred again as shown in Figure 6b-3. This observation suggests that dynamic complexation between boric acid and catechol groups at pH 9 can lead to reversible gelation.

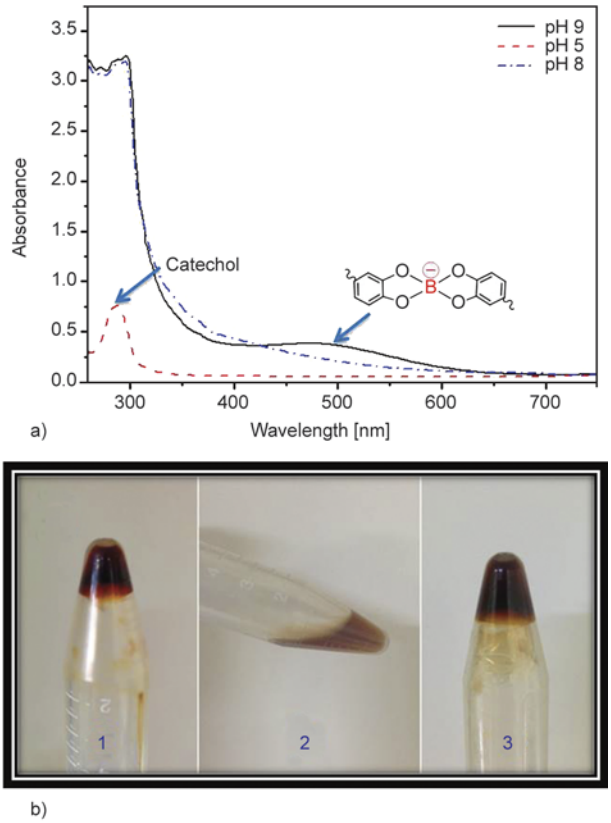

Figure 6. (a) UV-Vis absorbance of polyAspAm(DOP/EA) with boric acid solution. (b) Photographs of reversible gel formation

3.2.2. Reversibility of polyAspAm gel formation

In many prior investigations on the reversible non-covalent catechol-boron bonds, oxidation of the catechol group was a critical issue. Gelation experiments have been carried out to explain two alternative gelation mechanisms in different pH conditions. Increasing pH can lead to catechol group oxidation of the quinone and subsequent formation of irreversible covalent crosslinking. In order to prove these two mechanisms, the same amount of pH = 5 buffer was added to each gel sample, which was prepared under different pH conditions. The reversible coordinatively cross-linked gel (Figure 7a) completely dissolved after 10 min (Figure 7d). The $B(OH)_3$-catechol complex system is assumed to be in dynamic equilibrium, which means that a number of free catechols still exist in the system. Upon increasing the pH, the free catechol would be oxidized to the quinone, which finally damages the reversibility of gel formation. Figures 7b show the

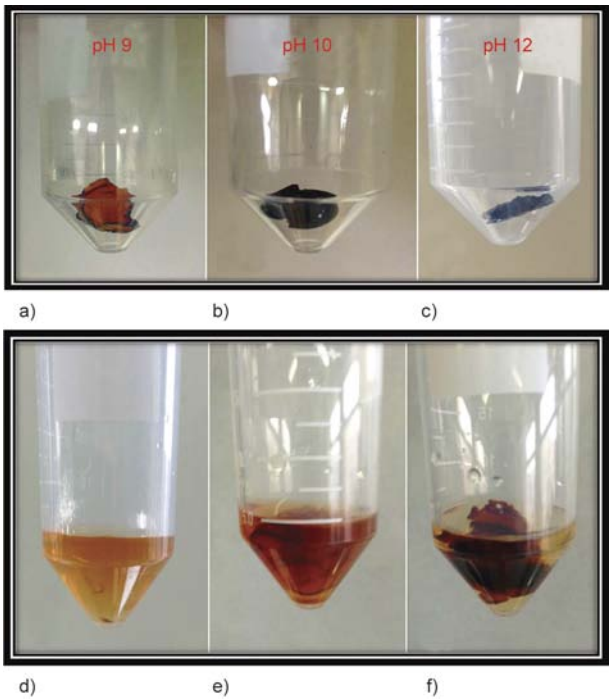

Figure 7. Photographs of gel samples: the original gels (a), (b) and (c) (gel formed at different pH conditions) were added a certain amount of pH 5 buffer solution to form different states (d), (e) and (f).

state of partially coordinative cross-linked gels, where some of the irreversible covalently cross-linked gels remained in a gel state (Figure 7e). In contrast, the dark brown gel (Figure 7c), formed at a higher pH of 12, remained almost the same without dissolution (see Figure 7f) due to the covalent cross-linking by the oxidation process.

3.3. Rheological properties of gels based on boron-catechol interactions

To investigate the rheological behavior of DOP-polyAspAm gels, dynamic mechanical analysis was performed with three different samples (Figure 8). The elastic modulus (G') and viscous modulus (G'') were measured as a function of frequency at a constant strain of 1% at 25°C. The elastic moduli of the three gel samples were highly dependent on frequency, and were more elastic at higher shear rates, showing a plateau. G'', however, increased along with decreasing frequency in the lower frequency range, suggesting a more viscous character at a decreased shear rate. The G' plateau increased slightly with increasing DOP content, probably due to an increase in the crosslinking density.

Figure 9 compared the modulus of two different gel samples obtained at pH 9 and pH 12. Both the boron-catechol coordination and covalent crosslinking via oxidative coupling can contribute to gel formation, but, the latter becomes more important at higher pH values. Although the type of cross-linking shifts from coordinative bonding to covalent bonding by increasing pH values from 9 to 12, the elastic modulus (G') of the $B(OH)_3$-catechol cross-linked gel was over 20-fold higher than the covalently bonded gel. This result indicates that the boron-catechol coordinative crosslinking density is significantly higher than that of quinone-mediated covalent cross-links, as boron-catechol mono-complexes, which remain in the covalently bonded gel, will prevent oxidative crosslinking, resulting in a lower mechanical stiffness of the gel.

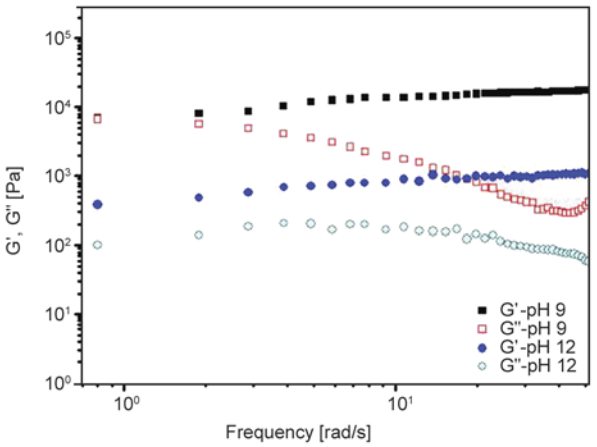

Figure 9. Comparison of moduli data in two different gels prepared at different pH values

The G' and G'' curves of polyAspAm gel at pH 9 with different gelator concentrations ($B(OH)_3$/catechol = 1:2 and 1:1 molar ratio) are presented in Figure 10. When the molar ratio of $B(OH)_3$/catechol was changed from 1:2 to 1:1, both the elastic modulus (G') and viscous modulus (G'') decreased dramatically. Because a sufficient amount of boric acid should lead to a gel comprised of a bidentate cross-linked structure rather than an uncross-linked or mono-dentate one, the mole ratio between boron and catechol is important for generating maximum crosslinking. For this reason, it is suggested that the molar ratio of $B(OH)_3$/catechol = 1:2 can be consid-

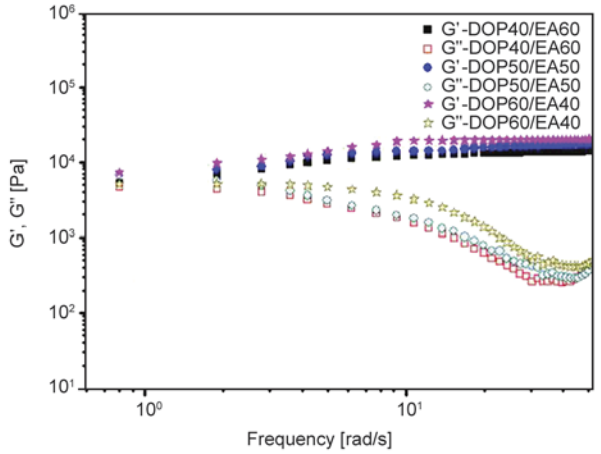

Figure 8. Rheological properties of gels made with dopamine-conjugated polyAspAm derivatives

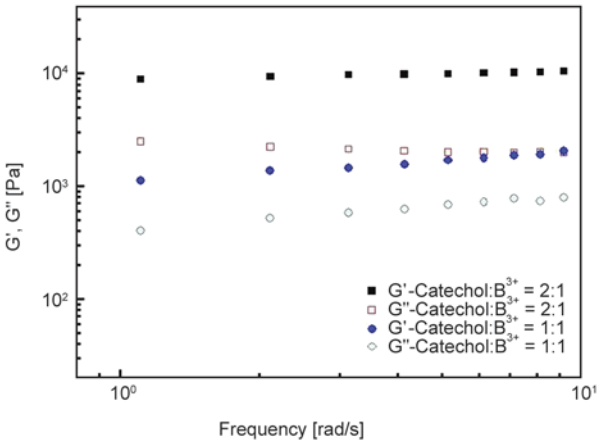

Figure 10. Comparison of moduli of polyAspAm gels made with different H_3BO_3 and DOP molar ratios

ered as an ideal ratio to make gels based on boron-catechol interactions.

3.4. Self-healing properties

The dynamic complexation between boron-catechol coordination can lead to the formation of reversible self-healing gels. As depicted in Figure 10, a plate of DOP-polyAspAm gel (in pH 9) (Figure 11a), cut into two pieces, could be healed autonomously and rapidly in a whole piece by simply contacting the fractured surfaces together without any outer intervention (Figure 11b and 11c). In addition, no obvious cut line was seen in the region of attachment after about 10 min (Figure 11d). Figure 9e showed that the jointed parts after healing were strong enough to be stretched without fracturing by the tweezers. When the healed gel was cut into two pieces, the same self-healing phenomenon was observed again wherever the gels were fractured, showing the property is repeatable and effective. This result can be ascribed to the dynamic complexation between boron and catechol groups.

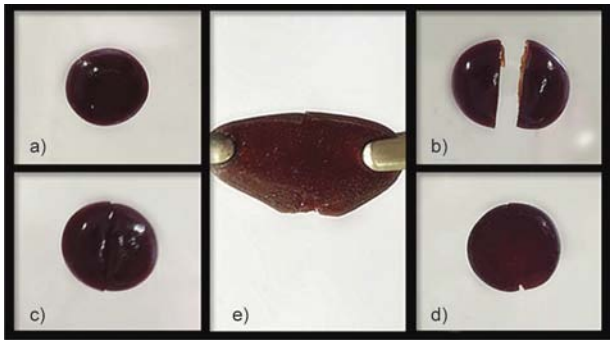

Figure 11. Photographs of evidence of self-healing: (a) the original sample, (b) sample cut into two pieces, (c) joining the pieces together, (d) the recovered sample and (e) the extended healed sample

In order to further demonstrate the self-healing recovery capabilities of the DOP-polyAspAm gel after complete deformation, dynamic mechanical analysis was employed. Figure 12a shows a strain sweep analysis at constant frequency measured by oscillatory rheometry, where the deformation strain was increased from 0.1 to 1000%. In the higher yield strain range, the elastic modulus (G') and viscous modulus (G'') decreased dramatically to result in gel failure. When the strain was increased to above 500%, the G'' value exceeded G', suggesting the gel state changed from solid to liquid. In the time sweep (Figure 12b) test of the gel sample, after the failure and subsequent self-healing, the elastic modulus (G') of the healed gel was found to recover to its original value, while the viscous modulus (G'') decreased by about 2-fold compared to the original value. However, the value of G'' tended to increase continuously during the time sweep, suggesting a gradual structural rearrangement within the healed gel. To summarize, the above results suggest dopamine-modified polyaspartamide possesses a self-healing property via the reversible boron-catechol coordination binding, which can lead to quick recovery after failure. This novel gel system has potential in several applications, including smart hydrogels, medical adhesives, and sealants.

4. Conclusions

A novel pH-responsive self-healing polyaspartamide derivative gel based on boron-catechol interactions has been prepared, and its rheological properties and self-healing behavior were investigated. The dynamic complexation between boric acid and catechol groups at pH 9 can lead to reversible gelation, as evi-

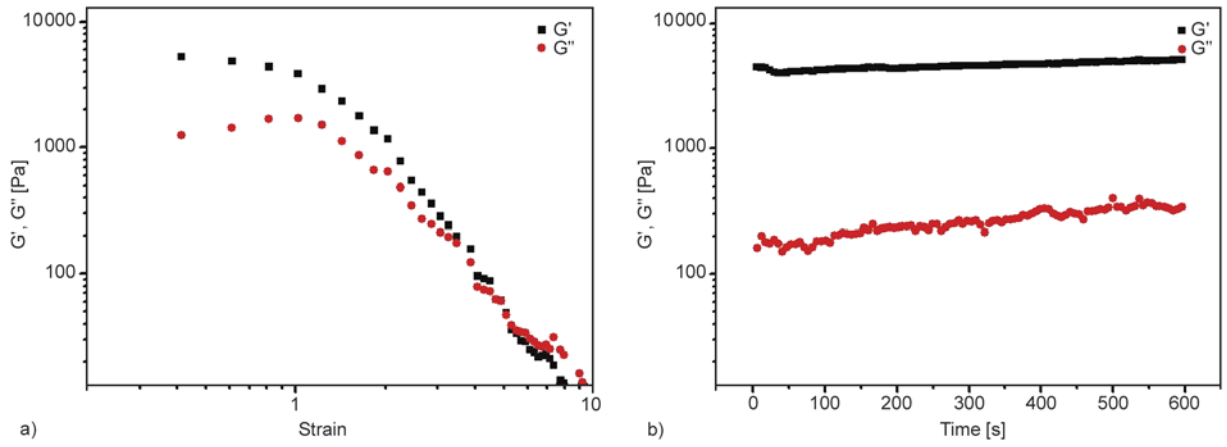

Figure 12. Self-healing behavior of polyAspAm(DOP/EA) with boric acid gel by strain sweep analysis followed by a time sweep analysis

denced by the solubility behavior and UV-Vis spectroscopy. The polyAspAm gels are quickly self-healing, as evidenced by a full recovery after fracture of the gel specimen. In addition, the rheological results showed that $B(OH)_3$-catechol coordinative cross-link density is higher than that of quinone-mediated covalent cross-links, and the molar ratio of $B(OH)_3$/catechol = 1:2 can be considered as an optimum ratio to make gels with improved mechanical properties.

Acknowledgements

This research was supported by the Basic Science Research Program through the National Research Foundation of Korea (NRF) funded by the Ministry of Education, Science and Technology (#2011-0011464).

References

[1] Moulay S.: Dopa/catechol-tethered polymers: Bioadhesives and biomimetic adhesive materials. Polymer Reviews, **54**, 436–513 (2014).
DOI: 10.1080/15583724.2014.881373

[2] Roberts M. C., Hanson M. C., Massey A. P., Karren E. A., Kiser P. F.: Dynamically restructuring hydrogel networks formed with reversible covalent crosslinks. Advanced Materials, **19**, 2503–2507 (2007).
DOI: 10.1002/adma.200602649

[3] Lee B. P., Messersmith P. B., Israelachvili J. N., Waite J. H.: Mussel-inspired adhesives and coatings. Annual Review of Materials Research, **41**, 99–132 (2011).
DOI: 10.1146/annurev-matsci-062910-100429

[4] Xu H., Nishida J., Ma W., Wu H., Kobayashi M., Otsuka H., Takahara A.: Competition between oxidation and coordination in cross-linking of polystyrene copolymer containing catechol groups. American Chemical Society Macro Letters, **1**, 457–460 (2012).
DOI: 10.1021/mz200217d

[5] Montarnal D., Cordier P., Soulié-Ziakovic C., Tournilhac F., Leibler L.: Synthesis of self-healing supramolecular rubbers from fatty acid derivatives, diethylene triamine, and urea. Journal of Polymer Science Part A: Polymer Chemistry, **46**, 7925–7936 (2008).
DOI: 10.1002/pola.23094

[6] Cordier P., Tournilhac F., Soulié-Ziakovic C., Leibler L.: Self-healing and thermoreversible rubber from supramolecular assembly. Nature, **451**, 977–980 (2008).
DOI: 10.1038/nature06669

[7] Burattini S., Colquhoun H. M., Greenland B. W., Hayes W.: A novel self-healing supramolecular polymer system. Faraday Discussions, **143**, 251–264 (2009).
DOI: 10.1039/B900859D

[8] Kalista S. J., Pflug J. R., Varley R. J.: Effect of ionic content on ballistic self-healing in EMAA copolymers and ionomers. Polymer Chemistry, **4**, 4910–4926 (2013).
DOI: 10.1039/C3PY00095H

[9] Krogsgaard M., Behrens M. A., Pedersen J. S., Birkedal H.: Self-healing mussel-inspired multi-pH-responsive hydrogels. Biomacromolecules, **14**, 297–301 (2013).
DOI: 10.1021/bm301844u

[10] Wei Z., Yang J. H., Zhou J., Xu F., Zrínyi M., Dussault P. H., Osada Y., Chen Y. M.: Self-healing gels based on constitutional dynamic chemistry and their potential applications. Chemical Society Reviews, **43**, 8114–8131 (2014).
DOI: 10.1039/C4CS00219A

[11] Yan X., Wang F., Zheng B., Huang F.: Stimuli-responsive supramolecular polymeric materials. Chemical Society Reviews, **41**, 6042–6065 (2012).
DOI: 10.1039/C2CS35091B

[12] Holten-Andersen N., Harrington M. J., Birkedal H., Lee B. P., Messersmith P. B., Lee K. Y. C., Waite J. H.: pH-induced metal-ligand cross-links inspired by mussel yield self-healing polymer networks with near-covalent elastic moduli. Proceedings of the National Academy of Sciences, **108**, 2651–2655 (2011).
DOI: 10.1073/pnas.1015862108

[13] Zhang Y., Tao L., Li S., Wei Y.: Synthesis of multiresponsive and dynamic chitosan-based hydrogels for controlled release of bioactive molecules. Biomacromolecules, **12**, 2894–2901 (2011).
DOI: 10.1021/bm200423f

[14] Yang B., Zhang Y., Zhang X., Tao L., Li S., Wei Y.: Facilely prepared inexpensive and biocompatible self-healing hydrogel: A new injectable cell therapy carrier. Polymer Chemistry, **3**, 3235–3238 (2012).
DOI: 10.1039/c2py20627g

[15] Kupfer S., Zedler L., Guthmuller J., Bode S., Hager M. D., Schubert U. S., Popp J., Gräfe S., Dietzek B.: Self-healing mechanism of metallopolymers investigated by QM/MM simulations and Raman spectroscopy. Physical Chemistry Chemical Physics, **16**, 12422–12432 (2014).
DOI: 10.1039/c4cp00562g

[16] Zhang Y., Yang B., Zhang X., Xu L., Tao L., Li S., Wei Y.: A magnetic self-healing hydrogel. Chemical Communications, **48**, 9305–9307 (2012).
DOI: 10.1039/c2cc34745h

[17] Schmidt S., Reinecke A., Wojcik F., Pussak D., Hartmann L., Harrington M. J.: Metal-mediated molecular self-healing in histidine-rich mussel peptides. Biomacromolecules, **15**, 1644–1652 (2014).
DOI: 10.1021/bm500017u

[18] Deng G., Tang C., Li F., Jiang H., Chen Y.: Covalent cross-linked polymer gels with reversible sol–gel transition and self-healing properties. Macromolecules, **43**, 1191–1194 (2011).
DOI: 10.1021/ma9022197

[19] He L., Fullenkamp D. E., Rivera J. G., Messersmith P. B.: pH responsive self-healing hydrogels formed by boronate–catechol complexation. Chemical Communications, **47**, 7497–7499 (2011).
DOI: 10.1039/C1CC11928A

[20] Fullenkamp D. E., Barrett D. G., Miller D. R., Kurutz J. W., Messersmith P.: pH-dependent cross-linking of catechols through oxidation via Fe^{3+} and potential implications for mussel adhesion. RSC Advances, **4**, 25127–25134 (2014).
DOI: 10.1039/C4RA03178D

[21] Menyo M. S., Hawker C. J., Waite J. H.: Versatile tuning of supramolecular hydrogels through metal complexation of oxidation-resistant catechol-inspired ligands. Soft Matter, **9**, 10314–10323 (2013).
DOI: 10.1039/C3SM51824H

[22] Nakahata M., Takashima Y., Harada A.: Redox-responsive macroscopic gel assembly based on discrete dual interactions. Angewandte Chemie International Edition, **53**, 3617–3621 (2014).
DOI: 10.1002/anie.201310295

[23] Zeng H., Hwang D. S., Israelachvili J. N., Waite J. H.: Strong reversible Fe^{3+}-mediated bridging between dopa-containing protein films in water. Proceedings of the National Academy of Sciences, **107**, 12850–12853 (2010).
DOI: 10.1073/pnas.1007416107

[24] Wilker J. J.: The iron-fortified adhesive system of marine mussels. Angewandte Chemie International Edition, **49**, 8076–8078 (2010).
DOI: 10.1002/anie.201003171

[25] Taylor S. W., Chase D. B., Emptage M. H., Nelson M. J., Waite J. H.: Ferric ion complexes of a DOPA-containing adhesive protein from *Mytilus edulis*. Inorganic Chemistry, **35**, 7572–7577 (1996).
DOI: 10.1021/ic960514s

[26] Yang W., Gao X., Wang B.: Biological and medicinal applications of boronic acids. in 'Boronic acids: Preparation and applications in organic synthesis and medicine' (ed.: Hall D. G.) Wiley, Weinheim, 481–512 (2005).
DOI: 10.1002/3527606548.ch13

[27] Cambre J. N., Sumerlin B. S.: Biomedical applications of boronic acid polymers. Polymer, **52**, 4631–4643 (2011).
DOI: 10.1016/j.polymer.2011.07.057

[28] Pizer R., Babcock L.: Mechanism of the complexation of boron acids with catechol and substituted catechols. Inorganic Chemistry, **16**, 1677–1681 (1977).
DOI: 10.1021/ic50173a021

[29] Paugam M-F., Valencia L. S., Boggess B., Smith B. D.: Selective dopamine transport using a crown boronic acid. Journal of the American Chemical Society, **116**, 11203–11204 (1994).
DOI: 10.1021/ja00103a064

[30] Vatankhah-Varnoosfaderani M., Hashmi S., Ghavami-Nejad A., Stadler F. J.: Rapid self-healing and triple stimuli responsiveness of a supramolecular polymer gel based on boron–catechol interactions in a novel water-soluble mussel-inspired copolymer. Polymer Chemistry, **5**, 512–523 (2014).
DOI: 10.1039/C3PY00788J

[31] Vatankhah-Varnoosfaderani M., GhavamiNejad A., Hashmi S., Stadler F. J.: Mussel-inspired pH-triggered reversible foamed multi-responsive gel – The surprising effect of water. Chemical Communications, **49**, 4685–4687 (2013).
DOI: 10.1039/C3CC41332B

[32] Kan Y., Danner E. W., Israelachvili J. N., Chen Y., Waite J. H.: Boronate complex formation with Dopa containing mussel adhesive protein retards pH-induced oxidation and enables adhesion to mica. PLOS One, **9**, e108869/1– e108869/7 (2014).
DOI: 10.1371/journal.pone.0108869

[33] Nishiyabu R., Kubo Y., James T. D., Fossey J. S.: Boronic acid building blocks: Tools for self assembly. Chemical Communications, **47**, 1124–1150 (2011).
DOI: 10.1039/C0CC02921A

[34] Nakahata M., Mori S., Takashima Y., Hashidzume A., Yamaguchi H., Harada A.: pH- and sugar-responsive gel assemblies based on boronate–catechol interactions. American Chemical Society Macro Letters, **3**, 337–340 (2014).
DOI: 10.1021/mz500035w

[35] White E. M., Seppala J. E., Rushworth P. M., Ritchie B. W., Sharma S., Locklin J.: Switching the adhesive state of catecholic hydrogels using phototitration. Macromolecules, **46**, 8882–8887 (2013).
DOI: 10.1021/ma401594z

[36] Lin W., Kim D.: pH-sensitive micelles with cross-linked cores formed from polyaspartamide derivatives for drug delivery. Langmuir, **27**, 12090–12097 (2011).
DOI: 10.1021/la200120p

[37] Scialabba C., Rocco F., Licciardi M., Pitarresi G., Ceruti M., Giammona G.: Amphiphilic polyaspartamide copolymer-based micelles for rivastigmine delivery to neuronal cells. Drug Delivery, **19**, 307–316 (2012).
DOI: 10.3109/10717544.2012.714813

[38] Ma Y., Jiang X., Zhuo R.: Biodegradable and thermosensitive polyaspartamide derivatives bearing aromatic structures. Materials Letters, **121**, 78–80 (2014).
DOI: 10.1016/j.matlet.2014.01.150

[39] Heo S-B., Jeon Y-S., Kim Y-J., Kim S-H., Kim J-H.: Bioinspired self-adhesive polymer for surface modification to improve antifouling property. Journal of Coatings Technology and Research, **10**, 811–819 (2013).
DOI: 10.1007/s11998-013-9528-9

[40] Neri P., Antoni G., Benvenuti F., Colola F., Gazzei G.: Synthesis of α, β-poly [(2-hydroxyethyl)-DL-aspartamide], a newplasma expander. Journal of Medicinal Chemistry, **16**, 893–897 (1973).
DOI: 10.1021/jm00266a006

[41] Ishihara K., Mouri Y., Funahashi S., Tanaka M.: Mechanistic study of the complex formation of boric acid. Inorganic Chemistry, **30**, 2356–2360 (1991).
DOI: 10.1021/ic00010a025

eXPRESS Polymer Letters Vol.9, No.9 (2015) 809–823
Available online at www.expresspolymlett.com
DOI: 10.3144/expresspolymlett.2015.76

Epoxy/anhydride thermosets modified with end-capped star polymers with poly(ethyleneimine) cores of different molecular weight and poly(ε–caprolactone) arms

C. Acebo[2], M. Alorda[1], F. Ferrando[3], X. Fernández-Francos[2], A. Serra[2], J. M. Morancho[1], J. M. Salla[1], X. Ramis[1]*

[1]Thermodynamics Laboratory, Heat Engines Department, ETSEIB, Universitat Politècnica de Catalunya, Av. Diagonal 647, 08028 Barcelona, Spain
[2]Department of Analytical and Organic Chemistry, Universitat Rovira i Virgili, C/ Marcel·lí Domingo s/n, 43007, Tarragona, Spain.
[3]Department of Mechanical Engineering, Universitat Rovira i Virgili, Països Catalans 26, 43007 Tarragona, Spain

Received 12 March 2015; accepted in revised form 1 May 2015

Abstract. Multiarm star polymers, with a hyperbranched poly(ethyleneimine) (PEI) core and poly(ε-caprolactone) (PCL) arms end-capped with acetyl groups were synthesized by ring-opening polymerization of ε-caprolactone from PEI cores of different molecular weight. These star polymers were used as toughening agents for epoxy/anhydride thermosets. The curing process was studied by calorimetry, thermomechanical analysis and infrared spectroscopy. The final properties of the resulting materials were determined by thermal and mechanical tests. The addition of the star polymers led to an improvement up to 130% on impact strength and a reduction in the thermal stresses up to 55%. The structure and molecular weight of the modifier used affected the morphology of the resulting materials. Electron microscopy showed phase-separated morphologies with nano-sized fine particles well adhered to the epoxy/anhydride matrix when the higher molecular weight modifier was used.

Keywords: *thermosetting resins, star polymers, epoxy resin, toughness, thermal stress*

1. Introduction

Epoxy resins are extensively used in technological fields such as electricity and electronics. They are employed as adhesives, matrices in advanced composites, surface coatings and device assemblies because of their combination of high strength and stiffness, excellent corrosion resistance and good electrical properties [1–3]. However, their inherent rigidity and high crosslinking density makes them brittle, thus limiting their potential range of applications. In addition, when epoxy thermosets are used as coatings, thermal stresses generated from the mismatch between the thermal expansion coefficients (*CTE*) of the coating and of the metallic substrate can lead to the appearance of defects that can limit their service life, such as the generation of microvoids and microcracks, the loss of adhesion due to warping. Thermal stress generated during cooling from the curing temperature down to operating conditions, typically room temperature, tends to be more severe than that consequence of heating or during service at constant temperature, especially when the temperature is below glass transition temperature (T_g) of the thermoset [4].

One of the most successful routes towards toughness improvement is to incorporate polymeric mod-

*Corresponding author, e-mail: ramis@mmt.upc.edu

ifiers into the thermosetting matrix to form fine morphological structures. Some effective polymer modifiers are liquid rubber [5], thermoplastics [6] or core-shell particles [7]. In general, these modifiers are initially miscible with the uncured thermoset precursors but partially or completely phase-separate to typically form spherical structures or bicontinuous structures. The problem of this strategy is a sharp increase of the viscosity of the blends, the drop in the modulus and glass transition temperature and sometimes the poor interfacial adhesion between phases. Recently, a significant toughening effect has been achieved without compromising other properties and processability by using dendritic polymers, especially if the structure and properties of the modifier have been tailored to enhance the physical and chemical interaction between them and the matrix. The improvement in toughness can be achieved by chemically induced phase separation (CIPS) or by *in situ* homogeneous reinforcing and toughening mechanism, but in both cases covalent linkages or a good compatibility between the modifier and the matrix are necessary [8–16].

The thermal stresses generated during cooling of thermosetting coatings applied over metal can be minimized by reducing the *CTE* and elastic modulus in the glassy state of the coating, as well as by decreasing its T_g, which in certain applications may not be desired. We recently reported the use of multiarm stars with poly(ethyleneimine) core and poly(ε-caprolactone) or poly(lactide) arms as modifiers in the curing of DGEBA using a tertiary amine as anionic curing agent [17, 18]. Upon addition of the modifiers, the decrease on T_g and glassy modulus led to a significant reduction in internal stresses, in spite of the increase in the glassy *CTE*. In another work, it could be seen that the addition of hyperbranched poly(ester-amide)s to epoxy/anhydride systems allowed reaching a significant reduction of the *CTE* in the glassy state and consequently on the thermal stress [19], the effect being more important when higher molecular weight modifiers were used. Recently, we used multiarm star polymers with hyperbranched poly(ethyleneimine) core and poly(ε-caprolactone) arms of different length with reactive and unreactive terminal groups as modifiers of epoxy/anhydride thermosets [20]. The overall stresses, measured on a steel substrate using the beam bending technique, were significantly reduced with modifiers containing reactive hydroxyl terminal groups and low degree of polymerization of the poly(ε-caprolactone) arms.

Taking all these precedents into account, in the present work we synthesized, following the 'core-first' approach, multiarm star polymers with hyperbranched poly(ethyleneimine) cores of different molecular weight and poly(ε-caprolactone) short arms. All the end hydroxyl groups resulting from the polymerization of ε-caprolactone were end-capped with acetyl moieties, but some amine groups of the poly(ethyleneimine) remain unmodified and can potentially react with epoxy groups. These multiarm star polymers were used to modify diglycidylether of bisphenol A/methyl hexahydrophthalic anhydride formulations in the presence of benzyl dimethyl amine as catalyst.

The synthesis of an amphiphilic modifier with hydrophilic core and hydrophobic shell, aimed at reaching phase-separated morphologies. The existence of reactive amino groups in the hyperbranched core would permit the incorporation of the modifier into the network structure, enhancing the interfacial adhesion between phases, if present. Moreover, the hydrophobic poly(ε-caprolactone) arms could contribute to the good interfacial adhesion between the hydrophobic matrix and the modifier-rich phase. To summarize, the goal of the present work is to enhance the toughness and reduce the internal stress in epoxy/anhydride formulations using amphiphilic star polymers with cores of different molecular weight, end-capped arms and reactive amine groups in the core structure.

The curing process was studied by calorimetry, infrared spectroscopy and thermomechanical analysis and the curing kinetics was analyzed by model-free and model-fitting methods. The final properties of the resulting materials were characterized by means of thermogravimetry, thermomechanical analysis and electron microscopy on the fracture surface. Impact resistance was evaluated by Izod impact tests and thermal stresses were estimated on the basis of *CTE*, T_g and elastic modulus measurements.

2. Experimental

2.1. Materials

Poly(ethyleneimine) (PEI) Lupasol®FG (M_w = 800 g/mol, data sheet) and Lupasol®WF (M_w = 25 000 g/mol, data sheet) were kindly donated by BASF (Ludwigshafen, Germany) and used without

further purification. From the molecular weight of the polymer and of the repeating unit, average degrees of polymerization of 18.3 for Lupasol®FG and 581.4 for Lupasol®WF were calculated. According to the data sheet, the relationship (NH_2/NH/N) was (1/0.82/0.53) for Lupasol®FG and (1/1.2/0.76) for Lupasol®WF, therefore the equivalent number of primary, secondary and tertiary amines is 10, 8.4, and 5.3 meq/g for Lupasol®FG and 8.0, 9.6, and 6.1 meq/g for Lupasol®WF.

ε-Caprolactone (ε-CL, 97%) was distilled under vacuum before use. Tin (II) 2-ethylhexanoate ($Sn(oct)_2$, 98%), *N*,*N*-dimethylbenzylamine (BDMA, >99%) and methyl hexahydrophthalic anhydride (MHHPA) were used without further purification. All these chemicals were purchased from Sigma-Aldrich (St. Louis, MO, USA). For the end-capping process by acetylation, extra pure acetic anhydride was used and purchased from Scharlau (Sentmenat, Spain). Triethyl amine (TEA) and *N*,*N*-dimethylamino pyridine (DMAP) were purchased from Fluka (Sentmenat, Spain). Chloroform ($CHCl_3$) was dried under $CaCl_2$ and distilled before use. Solvents were purchased from Scharlab (Sentmenat, Spain).

Diglycidylether of bisphenol A (DGEBA) with an epoxy equivalent of 187 g/eq (Epikote 828, Hexion Speciality Chemicals B.V. Louvain, Belgium) was dried for 4 hours at 40°C under vacuum before use.

2.2. Synthesis of poly(ethyleneimine)-poly(ε-caprolactone) end-capped multiarm stars (PEIX)

In the acronyms for both types of stars (PEIX), X accounts for the data sheet molecular weight times 10^{-2} and take the values of 8 and 250 for Lupasol®FG and Lupasol®WF, respectively.

The hydroxyl terminated star polymers were synthesized by ring-opening polymerization of ε-caprolactone from a hyperbranched poly(ethyleneimine) core in bulk at 130°C. The acetylation to obtain PEIX was performed with acetic anhydride at room temperature overnight in the presence of TEA and a catalytic amount of DMAP in $CHCl_3$ solution as previously described [17, 20]. Figure 1 depicts the synthetic procedure applied in the preparation of the stars.

For both PEIX star polymers ^{1}H NMR (400 MHz, $CDCl_3$, δ in ppm): 4.08 (–C<u>H</u>$_2$–OCO–), 2.32 (–NHCO–<u>CH</u>$_2$–, –<u>CH</u>$_2$–COO), 1.92 (OCO–<u>CH</u>$_3$), 1.70–1.30 (–<u>CH</u>$_2$–,CL chain) and 3.5–1.5 (PEI core). The structural data of the stars prepared determined by ^{1}H NMR and values in data sheet were as follows:

PEI8: polymerization degree of arms is 11.8. Fraction of unmodified primary/secondary amines of 0.15. T_g = –54°C, T_m = 58°C, Δh_m = 96 J/g, T_{max} = 390°C (temperature of the maximum rate of weight loss calculated by TGA).

PEI250: polymerization degree of arms is 13.5. Fraction of unmodified primary/secondary amines of 0.26. T_g = –59°C, T_m = 50°C, Δh_m = 75 J/g, T_{max} = 390°C.

2.3. Preparation of curing formulations

Mixtures containing MHHPA and the selected proportion of the star polymer were heated mildly until the modifier was dissolved and the solution became clear. The mixture was then cooled down to room temperature and added to the corresponding amount of DGEBA and catalyst. Finally, samples were carefully stirred and degassed under vacuum (at 40°C) during 15 min to prevent the appearance of bubbles during curing. The catalyst, BDMA, was used at a concentration of 1 phr (1 part of catalyst per hundred parts of DGEBA/MHHPA mixture). The modifier was added at concentrations of 5, 10 and 20% with

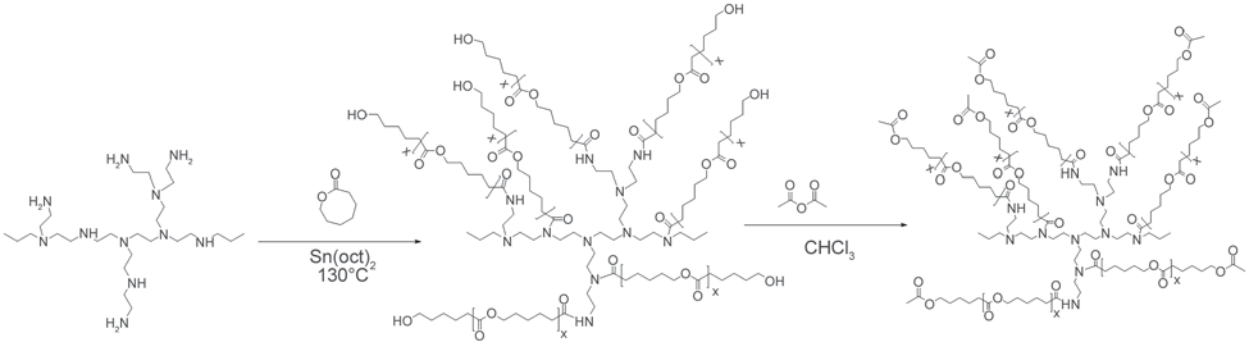

Figure 1. Synthetic procedure for the preparation of the multiarm stars PEI8 and PEI250

Table 1. Notation and composition of the neat and modified formulations in weight percentage [wt%] and in equivalents per gram of mixture. The weight percentage of the star polymer is indicated in formulation.

Formulation	DGEBA		MHHPA		BDMA		NH from SP
	[wt%]	[eq/g]	[wt%]	[eq/g]	[wt%]	[eq/g]	[eq/g]
Neat	52.1	$2.79\cdot10^{-3}$	46.9	$2.79\cdot10^{-3}$	0.99	$7.32\cdot10^{-5}$	0
5% PEI8	49.6	$2.65\cdot10^{-3}$	44.7	$2.65\cdot10^{-3}$	0.94	$6.97\cdot10^{-5}$	$3.95\cdot10^{-6}$
10% PEI8	47.4	$2.53\cdot10^{-3}$	42.6	$2.53\cdot10^{-3}$	0.90	$6.66\cdot10^{-5}$	$7.54\cdot10^{-6}$
20% PEI8	43.4	$2.32\cdot10^{-3}$	39.1	$2.32\cdot10^{-3}$	0.83	$6.10\cdot10^{-5}$	$1.38\cdot10^{-5}$
5% PEI250	49.6	$2.65\cdot10^{-3}$	44.7	$2.65\cdot10^{-3}$	0.94	$6.97\cdot10^{-5}$	$1.00\cdot10^{-5}$
10% PEI250	47.4	$2.53\cdot10^{-3}$	42.6	$2.53\cdot10^{-3}$	0.90	$6.66\cdot10^{-5}$	$1.92\cdot10^{-5}$
20% PEI250	43.4	$2.32\cdot10^{-3}$	39.1	$2.32\cdot10^{-3}$	0.83	$6.10\cdot10^{-5}$	$3.51\cdot10^{-5}$

respect to DGEBA/MHHPA/BDMA mixture. Table 1 collects the notation and composition of the different formulations studied.

Fully cured samples for DMA, TMA, TGA, DSC, impact and SEM assays were prepared by isothermal curing in oven at 100°C for 2 h followed by a postcuring at 180°C for one hour.

2.4. NMR Spectroscopy

^{1}H NMR and ^{13}C NMR measurements were carried out at 400 and 100.6 MHz, respectively, in a Varian Gemini 400 spectrometer (Palo Alto, USA). $CDCl_3$ was used as solvent. For internal calibration the solvent signals were used: δ (^{13}C) = 77.16 ppm and δ (^{1}H) = 7.26 ppm for $CDCl_3$.

2.5. Calorimetric measurements (DSC)

Calorimetric analyses were carried out on a Mettler DSC-822e thermal analyser (Greifensee, Switzerland). The calorimeter was calibrated using an indium standard (heat flow calibration) and an indium-zinc standard (temperature calibration).

Samples of approximately 10 mg were placed in aluminium pans with pierced lids and cured non-isothermally from 0 to 300°C at heating rates of 2, 5, 10 and 15°C/min, under nitrogen atmosphere, to determine the reaction heat associated with the complete conversion of all reactive groups and study the curing kinetics. In a non-isothermal curing process, the degree of conversion by DSC was calculated according to Equation (1):

$$\alpha = \frac{\Delta h_T}{\Delta h_{dyn}} \tag{1}$$

where Δh_T is the heat released up to a temperature T, obtained by integration of the calorimetric signal up to this temperature, and Δh_{dyn} is the total reaction heat associated with the complete conversion of all reactive groups. The reaction rate $d\alpha/dt$ was calculated as the first derivative of the conversion with respect to time.

The glass transition temperatures ($T_{g\infty}$s) of the obtained thermosets, uncured materials and star polymers were determined by means of a scan at 10°C/min under nitrogen atmosphere, as the temperature of the half-way point of the jump in the heat capacity when the material changed from glassy to the rubbery state under N_2 atmosphere and the error is estimated to be approximately ±1°C.

In order to predict the theoretical glass transition temperature of the formulations, Fox equation (Equation (2)) was used:

$$\frac{1}{T} = \frac{w}{T_{g,SP}} + \frac{1-w}{T_{g,matrix}} \tag{2}$$

where $T_{g,SP}$ and $T_{g,matrix}$ are the glass transition temperatures of the star polymer and neat epoxy/anhydride matrix respectively and w is the weight fraction of star polymer in the formulation.

2.6. Curing kinetics (DSC)

The linear integral isoconversional, model-free method of Kissinger-Akahira-Sunose (KAS) was used for the determination of the activation energy based on the non-isothermal curing curves, as shown by Equation (3):

$$\ln\left(\frac{\beta}{T^2}\right) = \ln\left(\frac{A\cdot R}{g(\alpha)\cdot E}\right) - \frac{E}{RT} \tag{3}$$

β is the heating rate, T the temperature, E the activation energy, A the pre-exponential factor, R the gas constant, and $g(\alpha)$ the integral conversion function. For each conversion degree, the representation of $\ln(\beta/T^2)$ versus $1/T$ produces a straight line and makes it possible to determine E and $\ln[A\cdot R/(g(\alpha)\cdot E)]$ from the slope and the intercept without knowing the kinetic model.

Isoconversional isothermal curing times, t, were estimated taking the non-isothermal data $\ln[A \cdot R/(g(\alpha) \cdot E)]$ and E, determined from Equation (3), and applying the rate equation integrated in isothermal conditions, as shown by Equation (4):

$$\ln t = \ln\left(\frac{g(\alpha)}{A}\right) + \frac{E}{RT} \tag{4}$$

Assuming that the approximation given by expression (3) is valid, we can determine the kinetic model that best describes the curing process by rearranging expression (3) as shown in Equation (5):

$$\ln\left(\frac{g(\alpha) \cdot \beta}{T^2}\right) = \ln\left(\frac{A \cdot R}{E}\right) - \frac{E}{RT} \tag{5}$$

which is the basis for the composite integral method for the determination of the kinetic model. Given that the curing of epoxy-anhydride can be satisfactory modelled using autocatalytic-like models with an overall reaction order around 2, we have fitted using Equation (5) the experimental data to autocatalytic kinetic models with $n + m = 2$, where n and m are the order of reaction.

The results of the kinetics analysis were used to model the curing and to determine the optimum curing times to achieve fully cured thermosets. In addition, isothermal curing times determined by simulation of non-isothermal kinetic data (Equations (3) and (4)) were compared with experimental isothermal curing times obtained by means of FTIR experiments.

Details of the kinetic methodology used can be found in previous works [21, 22].

2.7. FTIR spectroscopy

A Bruker Vertex FTIR spectrometer (Ettlingen, Germany) equipped with an attenuated-total-reflectance accessory with a diamond crystal (Golden Gate heated single-reflection diamond ATR, Specac-Teknokroma, Sant Cugat del Vallés, Spain) was used to monitor the curing process. Spectra were acquired in the mid-infrared region (spectral range of 600–4000 cm^{-1}) with a resolution of 4 cm^{-1}. 20 scans were averaged for each spectrum. The evolution of the functional groups was monitored during isothermal curing at 100°C, taking the band at 1508 cm^{-1}, attributed to the DGEBA aromatic rings, as a reference. The conversion was determined by the Lambert-Beer law from the normalized change of absorbance at 1732 cm^{-1} (formation ester groups) and at 1860+1785 cm^{-1} (disappearance of anhydride group) as explained in a previous work [22].

2.8. Thermomechanical analysis (TMA)

A thermo-mechanical analyzer Mettler thermomechanical analysis SDTA840 (Greifensee, Switzerland) was used to determine the conversion at the gel point and the thermal expansion coefficients.

A silanized glass fiber disc about 5 mm in diameter was impregnated with the liquid formulation and sandwiched between two aluminium discs. The sample was heated up from 40 to 200°C at 2°C/min and subjected to an oscillatory force from 0.005 to 0.01 N with an oscillation frequency of 0.083 Hz. The gel point temperature was taken as the onset in the decrease of the oscillation amplitude measured by the probe. The conversion at the gel point was determined from the gel point temperature and a dynamic curing experiment in the DSC at 2°C/min.

Cured samples (1.5×8×8 mm^3) were supported by two silica discs and heated at 5°C/min from 30 up to 150°C by application of a force of 0.02 N. Two heating scans were performed, the first one to erase the thermal history and the second one to determine the thermal expansion coefficients (*CTE*s), below and above the T_g, calculated according to Equation (6):

$$CTE = \frac{1}{L_0} \cdot \frac{\mathrm{d}L}{\mathrm{d}T} = \frac{1}{L_0} \cdot \frac{\frac{\mathrm{d}L}{\mathrm{d}t}}{\frac{\mathrm{d}T}{\mathrm{d}t}} \tag{6}$$

where, L is the thickness of the sample, L_0 the initial length, t the time, T the temperature and $\mathrm{d}T/\mathrm{d}t$ the heating rate.

2.9. Dynamic mechanical analysis (DMA)

DMA was carried out with a TA Instruments DMA Q800 (New Castle, DE, USA). Three point bending of 10 mm at 1 Hz and 0.05% strain was performed at 3°C/min from –150 to 250°C on prismatic rectangular samples (ca. 2×12×20 mm^3).

2.10. Thermal stress

The thermal stress caused by the variation of the temperature, σ_{th}, in a bi-layer strip (epoxy-anhydride coating/steel substrate) was determined from the radius of curvature, R, in the assumptions of the simple beam theory and from the free body analysis of strains in the two layers. The calculation was made

taking account the dependence on the geometrical parameters and properties of the sample and substrate, according to Benabdi and Roche methodology [23], see Equations (7) and (8):

$$\frac{1}{R}=\frac{6(1+\beta)^2(SFT-T_{amb})(CTE_c-CTE_s)}{(t_c+t_s)\left[3(1+\beta)^2(1+\alpha\beta)\left(\beta^2+\frac{1}{\alpha\beta}\right)\right]} \quad (7)$$

$$\sigma_{th}=\frac{1}{R}\cdot\frac{E_s\cdot t_s}{6}\left[\frac{1}{\beta(\beta+1)}(\alpha\beta^3+1)+3\alpha\beta\right] \quad (8)$$

where the subscripts *c* and *s* mean coating and substrate respectively, *t* is the thickness, *E* the elastic modulus, $\alpha = E_c/E_s$, $\beta = t_c/t_s$, *SFT* is the stress free temperature taken as the transition glass transition temperature determined by TMA and T_{amb} is the ambient temperature taken as 40°C.

In this study a stainless steel, with an elastic modulus of 180 053 MPa and thermal expansion coefficient of $16\cdot10^{-6}$°C^{-1}, was selected as the substrate and the thickness of the steel substrate and the epoxy/anhydride coating was respectively 0.1 and 0.4 mm. The elastic modulus of epoxy/anhydride sample was determined by DMA.

2.11. Thermogravimetric analysis (TGA)

Thermogravimetric analysis was carried out with a Mettler TGA/SDTA 851e/LF/1100 thermobalance (Greifensee, Switzerland). Samples with an approximate mass of 10 mg were degraded between 30 and 800°C at a heating rate of 10°C/min in a nitrogen atmosphere (50 cm3/min measured in normal conditions).

2.12. Impact resistance

The impact test was performed at room temperature by means of an Zwick 5110 impact tester (Ulm, Germany) according to ASTM D 4508-10 (2010) using rectangular samples (2×12×25 mm^3). The pendulum employed had a kinetic energy of 0.5 J. For each material, nine determinations were made. The impact strength (*IS*) was calculated from the energy absorbed by the sample upon fracture according to Equation (9):

$$IS=\frac{E-E_0}{S} \quad (9)$$

where *E* and E_0 are the energy loss of the pendulum with and without sample respectively, and *S* is the cross-section of the samples.

2.13. Electron microscopy analysis (SEM)

The fracture surface of the samples, previously fractured by impact at room temperature, was coated with a conductive gold layer and then examined with a Jeol JSM 6400 SEM (JEOL Ltd., Tokyo, Japan) with a resolution of 3.5 nm and different magnifications (100, 500 10 000 and 50 000).

3. Results and discussion

3.1. Synthesis and characterization of multiarm stars

The synthesis of the multiarm stars was performed as previously described in two different papers, one of them describing the growing of the poly(ε-caprolactone) arms from the PEI core and the other to the blocking of hydroxyl end-groups by reaction with acetic anhydride [17, 20]. The length of the arms can be adjusted, in principle, from the amount of ε-CL per reactive group in the core (NH and NH_2). In this paper, PEI cores of 800 and 25 000 g/mol of mass-average molecular weight were employed.

The multiarm star molecules where characterized by ^{1}H NMR spectroscopy as done in the previous works [17, 20]. It could be seen that the increase in the molecular weight of the core did not change significantly the ^{1}H NMR spectrum. From the spectra of the hydroxyl-ended stars we could determine the degree of polymerization of the arms. However, in both cases the arms were longer (*DP* = 11.8 and 13.5) than expected (*DP* = 10) and the difference was higher for the larger core. Since all the ε-CL reacts, the higher polymerization degree of the arms calculated from the spectra led us to the conclusion that part of the NH- and NH_2 groups could not initiate the growth of an arm. From these values we estimated a degree of modification of 0.85 for the PEI8 core and of 0.74 for the PEI250 core. The effect of the core size is noteworthy, as the degree of modification of the PEI250 core is significantly lower. The hydrogen bond interactions and the steric hindrance could be the responsible for these differences. Although the evaluation of the modification achieved in terminal and linear units could not be accomplished, linear units seem to be less reactive because of the lower nucleophilicity of secondary amines and the more internal position of these units in the PEI structure. Moreover, intra-molecular hydrogen bonding in PEI may make difficult the penetration of ε-CL into the core structure and the subsequent polymerization reaction.

The acetylation of the hydroxyl groups at the end of the arms was performed as described and the spectra obtained were similar to the ones published before [20]. The complete disappearance of $–CH_2OH$ signals showed that all hydroxyl groups were blocked. The intensity of the methyl signals (at 1.92 ppm) allowed us to determine that unreacted NH groups were still in PEI8 and PEI250 structures.

By using linear standards the molecular weight of star polymers are usually underestimated by GPC and this method does not rend accurate molecular weights. However, the GPC analysis did not produce signals at low molecular weight, meaning that no detectable poly(ε–caprolactone) homopolymer was formed during the ring-opening polymerization. In addition, the shape of the curves was unimodal in both PEI8 and PEI250, due to the living characteristics of the ε-CL polymerization.

3.2. Study of the curing and thermal properties of DGEBA/MHHPA/PEIX mixtures

The presence of hydroxyl groups and tertiary amines in epoxy-anhydride formulations, leads to a complex competitive mechanism consisting of polycondensation, initiated by hydroxyl groups, and ring opening polymerization, initiated by tertiary amine [19, 24]. Moreover the existence of secondary and/or primary amines in the reaction medium may also lead to a polycondensation between these groups and epoxy resin or even anhydrides and the concomitant appearance of new tertiary amines or amides. In previous works we reported the use of hyperbranched poly(ethyleneimine)s as crosslinking agents in epoxy formulations [25, 26], reacting by an epoxy-amine condensation mechanism and getting thus incorporated into the network structure of the thermoset. The curing kinetics was slowed down by their lower mobility in comparison with smaller amines and they led to more densely crosslinked materials due to the presence of internal branching points in the hyperbranched polymer structure. However, the total number of reactive amino groups introduced in the formulation is very small taking into account the elevated molecular weight of the stars polymers, and the effect would be difficult to quantify. It should be also noticed that not all the amine groups would be able to react because of steric hindrance or topology restrictions.

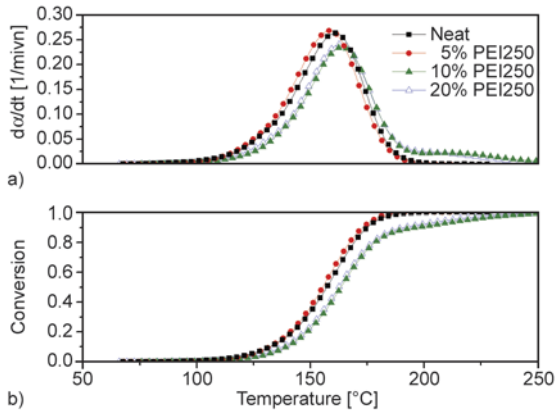

Figure 2. Reaction rate dα/dt (a) and degree of conversion (b) against temperature of neat and PEI250 formulations at 10°C/min

Figure 2 shows the plots of degree of conversion and reaction rate against temperature recorded at 10°C/min of neat formulation and formulations containing different amounts of PEI250. Calorimetric curves for neat and 5% showed a unimodal shape, which indicates that, the different curing mechanism takes place at the same time or that one of them predominates, in particular the epoxy-anhydride alternating copolymerization mechanism, due to the presence of BDMA. Formulations containing 10 and 20% of PEI250 show a secondary process at conversions above 0.8. Because epoxy-amine condensation may take place at a relatively low temperature [25, 26] this process, at high temperature and slow rate, could be related with the non-catalytic epoxy/anhydride curing mechanism or epoxy homopolymerization, although this is generally observed in anhydride-deficient formulations [27].

In the presence of a small amount of star polymer the curing is slightly accelerated possibly due to the additional tertiary amines coming from the modifier. When a higher amount of modifier is used (10 and 20%) the reaction rate decrease and the conversion-temperature curves shift at higher temperatures (Figure 2). In these last cases the higher viscosity of the formulations, the lower mobility of the reactive species and the lower content of epoxides may contribute to decelerate the curing rate of the epoxy/anhydride/PEIX formulations. Although the differences between formulations are not large, the relative influence of the discussed parameters can lead to acceleration or deceleration of the curing.

When PEI8 was used as modifier a similar trend was observed (not shown), although both effects, accel-

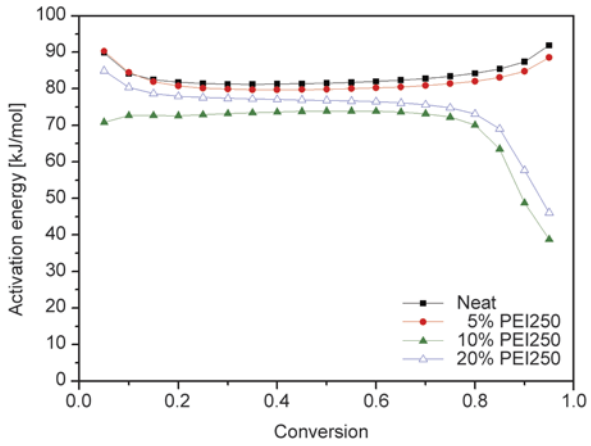

Figure 3. Activation energy during curing of neat and PEI250 formulations obtained by using the Kissinger-Akahira-Sunose method

eration at low modifier content and deceleration at high modifier content, take place to a lesser extent. This result can be rationalized on the basis of the lower tertiary amine content and viscosity of PEI8 than PEI250.

The nonisothermal curing kinetics was analyzed using the isoconversional KAS methodology (Equation (3)). Figure 3 shows that E remains constant during the entire range of conversions for neat and 5% formulations, whereas for 10 and 20% E is maintained constant up to a conversion of 0.8, to decrease sharply between 0.8 and 1. This result is consistent with the existence of two curing mechanisms, activated at different temperatures, in modifier-rich formulations (Figure 2).

As described in the experimental section, model fitting was performed using suitable phenomenological model, autocatalytic model with $n + m = 2$ [22, 24], which may generally describe the autocatalytic behaviour of the catalyzed epoxy-anhydride curing. Non-isothermal data at different heating rates were simultaneously fitted by linear regression (Equation (5)), in the conversion range 0.1–0.8, where activation energy is nearly constant for all formulations.

Table 2 summarizes the results of the linear fitting and other kinetic parameters. The linear regression coefficients get close to one and the similarity between fitted and isoconversional activation energies evidence the quality of the fitting and the suitability of the kinetic model chosen. All formulations show similar kinetic parameters, an indication of the fact that the curing mechanism is not significantly affected by the presence of the star polymer modifier. The values of $d\alpha/dt$ and k, calculated using Arrhenius equation and the kinetic parameters, activation energy and pre-exponential factor obtained by adjustment, agree with the reactivity of the different formulations and with the experimental calorimetric curves (Figure 2). On increasing the content of star polymer up to 5%, the curing accelerates (k and $d\alpha/dt$ increase), but gradually decelerates (k and $d\alpha/dt$ decrease) at higher modifier contents. The kinetic effects of the modifier are more relevant when PEI250 is used, showing greater differences between the values of k and $d\alpha/dt$ and those of the neat formulation.

The curing kinetics of all formulations were studied with FTIR spectroscopy at 100°C in order to identify the main reactions taking place during curing and compared with the curing kinetics obtained by non-isothermal procedure. Figure 4 shows FTIR spectra recorded during isothermal curing of neat formulation at 100°C. The general features of the epoxy-anhydride curing reaction can be observed: the decrease of the anhydride groups (bands at 1780 and 1860 cm^{-1}) that react giving rise to ester groups (1735 cm^{-1}). The disappearance of epoxy groups was also observed but not quantified because of the difficulty to separate its contribution from the different overlapping signals in the region around 910 cm^{-1}.

Table 2. Kinetic parameters of curing process

Formulation	E^a [kJ/mol]	$\ln A^a$ [min^{-1}]	n^a	m^a	r^a	$k_{150°C}{}^b$ [min^{-1}]	$(d\alpha/dt)_{0.5}{}^c$ [min^{-1}]	$E_{iso}{}^d$
Neat	82	22.92	1.58	0.42	0.999	0.66	0.165	83
5% PEI8	76	21.39	1.53	0.47	0.999	0.69	0.174	77
10% PEI8	77	21.42	1.54	0.46	0.999	0.65	0.161	77
20% PEI8	67	18.48	1.53	0.47	0.999	0.50	0.125	69
5% PEI250	81	22.64	1.55	0.45	0.999	0.75	0.187	82
10% PEI250	70	18.95	1.57	0.43	0.992	0.38	0.095	71
20% PEI250	75	20.95	1.57	0.43	0.999	0.45	0.113	75

[a]Kinetic parameters obtained by model-fitting using an autocatalytic model with $n + m = 2$

[b]Values of rate constant at 150°C using the Arrhenius equation and the parameters E and ln A

[c]Values of reaction rate at 150°C obtained using the equation rate $d\alpha/dt = k \cdot f(\alpha) = k \cdot (1 - \alpha)^n \cdot \alpha^n$ at 50% conversion

[d]Average isoconversional activation energy.

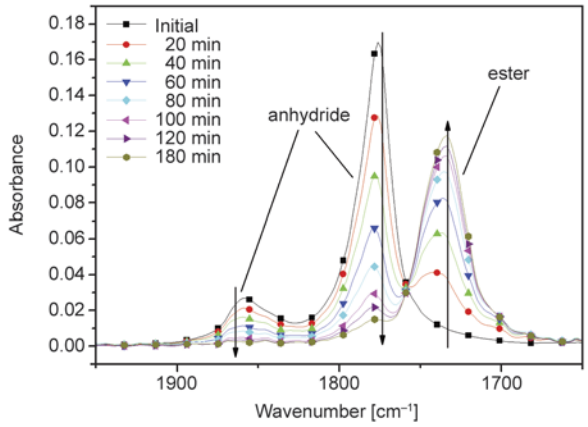

Figure 4. FTIR spectra recorded during curing of neat formulation at 100°C

Figure 5 shows the evolution of ester and anhydride groups against time recorded during curing for the 10%PEI250 formulation at 100°C in the spectrometer. It can be observed that the formation of ester and the disappearance of anhydride groups take place almost at the same time up to 0.6 of conversion, showing little discrepancies at higher conversion. This result agrees with the fact the curing mainly follows an alternating epoxy-anhydride mechanism catalyzed by tertiary amines. The inset in Figure 5 plots the ester conversion with respect to the anhydride conversion at 100°C for neat and all the PEI250 formulations. It can be observed that the evolution of both groups follows the diagonal line, indicating again an alternating copolymerization mechanism. Figure 5 shows the conversion of epoxy groups determined by using Equation (4) from the non-isothermal isoconversional kinetic parameters obtained by DSC.

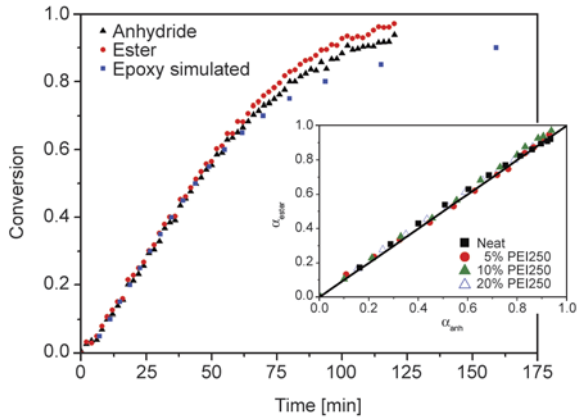

Figure 5. Conversion of the ester groups, α_{ester}, and reacted anhydride, α_{anh}, during curing of 10% PEI250 formulation at 100°C in FTIR. Epoxy conversion simulated using non-isothermal isoconversional DSC data. Inset: conversion of the ester groups against reacted anhydride for neat and PEI250 formulations.

It can be observed that the conversions are similar to those obtained by FTIR. The slight differences between the evolutions of the different reactive species observed at high conversions can be related with the activation of a second curing mechanism that takes place during non-isothermal curing in DSC (Figure 5) at higher temperatures, uncatalyzed epoxy-anhydride reaction or epoxy homopolymerization, a process that is not activated during isothermal curing at moderate temperatures. FTIR and DSC simulation of PEI8 formulations showed similar trends than those observed for PEI250.

It can be concluded that curing of epoxy-anhydride formulations containing PEI8 and PEI250 proceeds mainly by anionic alternating copolymerization catalyzed by tertiary amines. Rocks *et al*. [28] studied the curing of epoxy-anhydride formulations catalyzed by tertiary amines by Raman spectroscopy and concluded that, in spite of the complexity of the curing mechanism, the overall curing profile corresponded to an alternating epoxy-anhydride copolymerization. However, epoxy-amine condensation may take place, thus permitting the covalent linkage between the modifier and the matrix. The quantification of this process is not possible, since it may take place to a very low extent. The other processes, occurring at higher temperatures, as observed by DSC, may not be relevant depending on the isothermal curing schedule selected in the processing.

Table 3 shows the experimental heats of polymerization, Δh, calculated as the average heat of the experiments at different heating rates. On increasing the proportion of modifier Δh [J/g] decreases due to the lower content of reactive epoxy and anhydride groups, whereas Δh [kJ/ee] remains almost constant and similar to the values reported for other similar epoxy systems [29]. FTIR spectra of both isothermal and non-isothermal cured samples showed that the absorbance bands of oxirane and anhydride groups disappeared completely. Moreover, no residual heat was observed after a second dynamic scan made up to 250°C to determine T_g. These results indicate that all formulations reacted almost completely.

The T_g of the isothermally cured samples, determined by DSC, decreases progressively on increasing the proportion of star polymer in the formulation, but this decrease is more evident when PEI250 is used. The different flexibilities of both modifiers, the amount of physical entanglement and crosslinking density and the existence of separated phases of different size

Table 3. Calorimetric data, α_{gel}, thermal stability data and dynamomechanical properties of the formulation studied in this work

Formulation	Δh[a] [J/g]	Δh[b] [kJ/ee]	$T_{g\infty}$[c] [°C]	$T_{g\infty,Fox}$[d] [°C]	α_{gel}[e]	T_{max}[f] [°C]	tan δ[g] peak [°C]	tan δ[h] FWHM [°C]	E_r'[i] [MPa]
Neat	288	103	132	132	0.47	406	143	14	28
5% PEI8	272	103	126	115	0.55	406	139	17	24
10% PEI8	258	103	118	99	0.49	405	130	25	20
20% PEI8	249	112	111	71	0.52	405	124	32	16
5% PEI250	257	97	118	115	0.45	405	127	16	23
10% PEI250	255	102	111	99	0.45	404	124	25	18
20% PEI250	230	103	103	71	0.48	403	114	32	13

[a]Enthalpies per gram of mixtures
[b]Enthalpies per equivalent of epoxy groups
[c]Glass transition temperature after isothermal curing
[d]Calculated glass transition temperature, using DSC data and Fox equation
[e]Degree of conversion at gelation determined as the conversion reached by non-isothermal TMA and DSC tests at 2°C/min
[f]Temperature of the maximum rate of weight loss calculated by thermogravimetry
[g]Temperature of maximum of tan δ
[h]FWHM stands for full width at half maximum of tan δ
[i]Storage modulus in the rubbery state determined at tan δ peak + 50°C

and structure could be responsible of this behaviour. In order to understand the effect of the star on the matrix, the Fox equation was applied to predict the T_g of the fully cured thermosets. Up to 5% of PEI250 content, the thermosets have an experimental value of T_g similar to the predicted by this equation, whereas formulations containing 10 and 20% of both modifiers show experimental T_g's significantly higher than the theoretical ones. These results could be explained by a phase separation of the star polymer due to the incompatibility produced during the curing reaction, which was further confirmed by electron microscopy.

The results of the gelation tests are summarized in Table 3. The conversion at the gelation point α_{gel} is only little affected by the addition of both star polymers, and in all cases the obtained values are within the range commonly observed for epoxy-anhydride systems, around 0.3–0.5 [24, 30, 31]. This scattering of values can be explained not only by the differences and accuracy of the measuring techniques but from the presence of protic impurities or the occurrence of initiator regeneration reactions that tend to increase α_{gel} [30–32].

Figure 6 shows the thermogravimetric curves for neat and PEI250 formulations. It can be observed that the degradation takes place in only one step, indicating random breaking of bonds. Formulations containing PEI8 show similar TGA traces (not shown). The results of the thermogravimetric analysis of all formulations are summarized in Table 3. Although modified formulations contain C–N bonds that are less stable than the C–C bonds of the epoxy matrix,

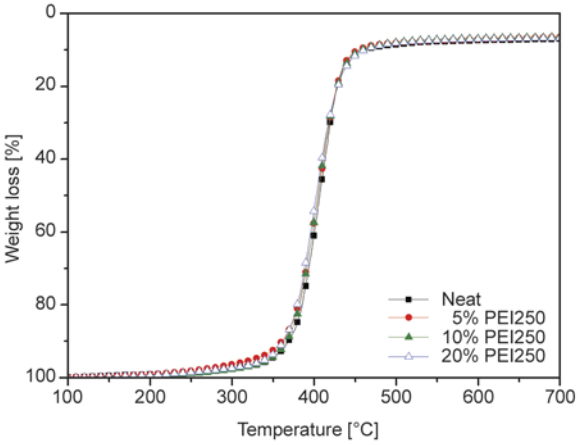

Figure 6. Thermogravimetric curves at 10°C/min in nitrogen atmosphere of the neat and PEI250 formulations

all formulations show similar thermal stability (T_{max}). This is in agreement with previously reported results using poly(ε-caprolactone) modified polymers [17, 20]. This can be explained by the low proportion of hyperbranched core in the modifier structure (even lower in the formulation), the similar thermal stability of the ester bonds in the poly(ε-caprolactone) arms and the epoxy-anhydride polyester network structure, and the possible covalent linkage between the matrix and the modifier.

3.3. Thermomechanical properties and thermal stress

Table 3 collects the results of the DMA characterization of all the samples prepared. Figures 7 and 8 plot the evolution of tan δ and storage modulus of PEI250 and PEI8 formulations, respectively. In

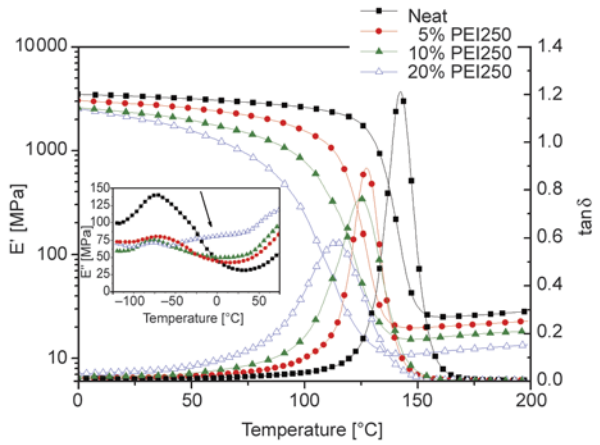

Figure 7. Storage modulus and tan δ curve against temperature for neat and PEI250 modified materials. The inset shows a detail of loss modulus curves at low temperatures.

agreement with the calorimetric data, when the proportion of modifier increases, the network relaxation curves are shifted towards lower temperatures, indicating that T_g decreases on adding modifier, as seen with DSC. The effect is more remarkable in PEI250 formulations, probably due to an increase in the plasticization caused by the longer poly(ε-caprolactone) arms or a decrease in the crosslinking density. It can also be observed that the α-relaxations (related to the T_g) of all formulations are unimodal, indicating that all thermosets have homogeneous network structures, but modifier-rich formulations show a more disperse network, as seen from the broader α-relaxation and higher FWHM values. Meng and coworkers [33, 34] observed the contrary trend using hyperbranched polyethers as toughening for epoxy/amine systems, but their materials showed a homogeneous morphology. Table 3

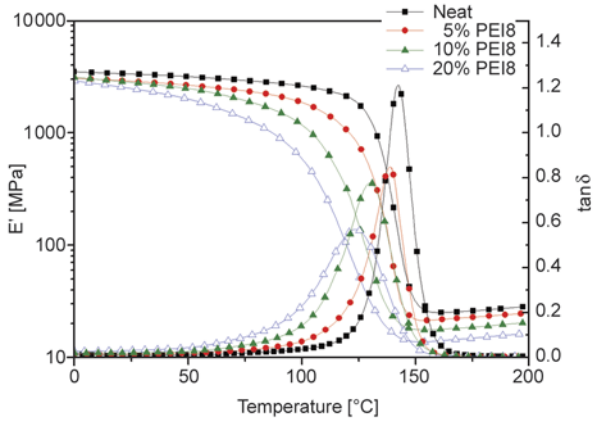

Figure 8. Storage modulus and tan δ curve against temperature for neat and PEI8 modified materials

and Figures 7 and 8 show a decrease in the rubbery modulus and in the height of α-relaxation upon addition of the modifier. According to the rubber elasticity theory, the relaxed modulus is proportional to the crosslinking density, but deviations from the ideal network behaviour are likely to occur for a variety of reasons [26, 35, 36]. The decrease in rubbery modulus is not proportional to the modifier content, suggesting an additional decrease in the crosslinking density connected with the participation of the star polymer in the curing process.

The inset in Figure 7 shows a detail of loss modulus curves in the region of low temperature. It can be seen that the β-relaxation (attributed to glyceryl or diphenylpropane groups) decreases but it broadens on increasing the modifier content. This can be tentatively attributed to a new star polymer-rich phase formed during curing and to a restricted mobility of the matrix structure due to the additional bonding with star-polymer.

In order to determine the potential application of the prepared materials as coatings, the generation of thermal stress during cooling of neat and PEI250 and PEI8 formulations on steel as a rigid substrate were studied using the Benabdi and Roche methodology described in the experimental section [23]. In a previous work, we demonstrated that the intrinsic stress generated during curing of an epoxy system, due to rearrangement of molecular structure, and the thermal stress generated in the rubbery state, are much lower than the thermal stress generated on cooling down from the T_g to room temperature [14, 20], therefore in the present work we only calculate the thermal stress originated on cooling.

Table 4 collects the thermal stress values, σ_{th}, calculated using Equations (7) and (8) and the following experimental data of epoxy/anhydride/PEIX coating: CTE_c in the glassy state determined by TMA, elastic modulus determined by DMA at room temperature (40°C), E_c, and stress free temperature, *SFT*, taken as the glass transition temperature determined by TMA. It can be observed as σ_{th} decreases significantly on increasing the modifier content, due to a decreasing of some of these three parameters: CTE_c, E_c and *SFT*. In general, E_c and *SFT* regularly decrease on increasing PEIX content, according to the high flexibility and low crosslinking density of modified thermosets, whereas CTE_c does not follow a clear trend. While the CTE_c of PEI8 formulations hardly varies, CTE_c of PEI250 formulations

Table 4. Thermal data of the materials and thermal stresses generated during cooling for the different formulations

Formulation	E_c[a] [MPa]	α[b]	SFT[c]	CTE_c[d]	1/R[e] [mm^{-1}]	σ_{th}[f] [MPa]
Neat	3241	0.018	125	87	0.0169	16.4
5% PEI8	2796	0.016	119	83	0.0146	12.5
10% PEI8	2626	0.015	113	85	0.0137	11.2
20% PEI8	2203	0.012	104	92	0.0129	9.1
5% PEI250	2687	0.015	109	93	0.0145	12.1
10% PEI250	2505	0.014	105	95	0.0139	10.9
20% PEI250	1782	0.010	96	102	0.0123	7.4

[a]Elastic modulus determined by DMTA.
[b]Ratio of coating and substrate module $\alpha = E_c/E_s$.
[c]Stress free temperature taken as the transition glass transition temperature determined by TMA.
[d]Thermal expansion coefficient in the glassy state determined by TMA.
[e]Curvature determined using Equation (7).
[f]Thermal stress determined using Equation (8).

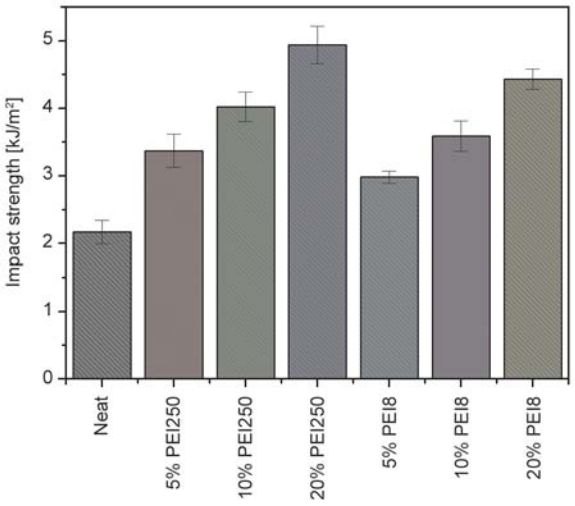

Figure 9. Impact strength for neat DGEBA/anhydride and thermosets with PEI250 and PEI8

increases slightly. Although this increase tends to increase the stresses, the lower E_c and *SFT* values of PEI250 formulations compensate this effect leading to significant reduction of thermal stress. This reduction is higher for PEI250 formulations than for PEI8 formulations and the highest reduction of σ_{th} is achieved by adding a 20% of PEI250. These results agree, again, with the higher flexibility and lower crosslinking density induced by the presence of PEI250 and its possible participation in the curing process.

3.4. Mechanical characterization and morphology

The toughness behaviour of all cured formulations was investigated by impact test and the morphology was analyzed by SEM on the impacted fracture. Figure 9 shows that both PEI250 and PEI8 produce a significant increase in the impact strength of the cured materials, proportional to the amount of modifier used. This increase is more than 100% with respect to the neat formulation, for thermosets containing a 20% of both modifiers. This result is consistent with a phase-separated morphology, where soft particles of modifier adhered to the epoxy/anhydride matrix absorb energy during impact test, although the DMA and DSC results showing a decrease in the T_g of the cured material suggest also some enhancement in the matrix shear yielding. The degree of interfacial adhesion between the soft phase and the matrix is critical in toughening. Effective toughening is believed to occur with an intermediate interfacial bonding, since an excessive adhesion can deteriorate the interfacial adhesion between the toughener phase and the matrix [36]. In previous works we observed that polymeric modifiers with excessive physical-chemical compatibility with the matrix led to their covalent incorporation into the network structure, preventing phase separation and producing very little toughness enhancement, whereas polymers that phase-separate during curing but with certain physical-chemical compatibility with the matrix led to the highest increase in impact strength [14]. Although it is not possible to know the amount of amine groups that react during curing, it is reasonable assuming the formation of some covalent bonds between the remaining amine groups at the core of the star polymer and the epoxy groups. Although the addition of both stars increases toughness characteristics the improvement achieved with PEI250 is higher. The amount of covalent bonds formed between matrix and modifier, the higher flexibility of PEI250 and the resulting polymer matrix and the lower thermal stress in PEI250 formulations can justify the differences observed between PEI250 and PEI8 thermosets.

Figure 10 shows some SEM micrographs of the fractured surfaces of materials after impact tests. In previous works it was observed that the fracture of the neat DGEBA/anhydride formulation is relatively smooth and glassy and does not show any significant morphological features, due to the formation of a homogeneous material [20, 37]. On the contrary, materials containing PEI8 and PEI250 (Figure 7) show a characteristic morphology completely differ-

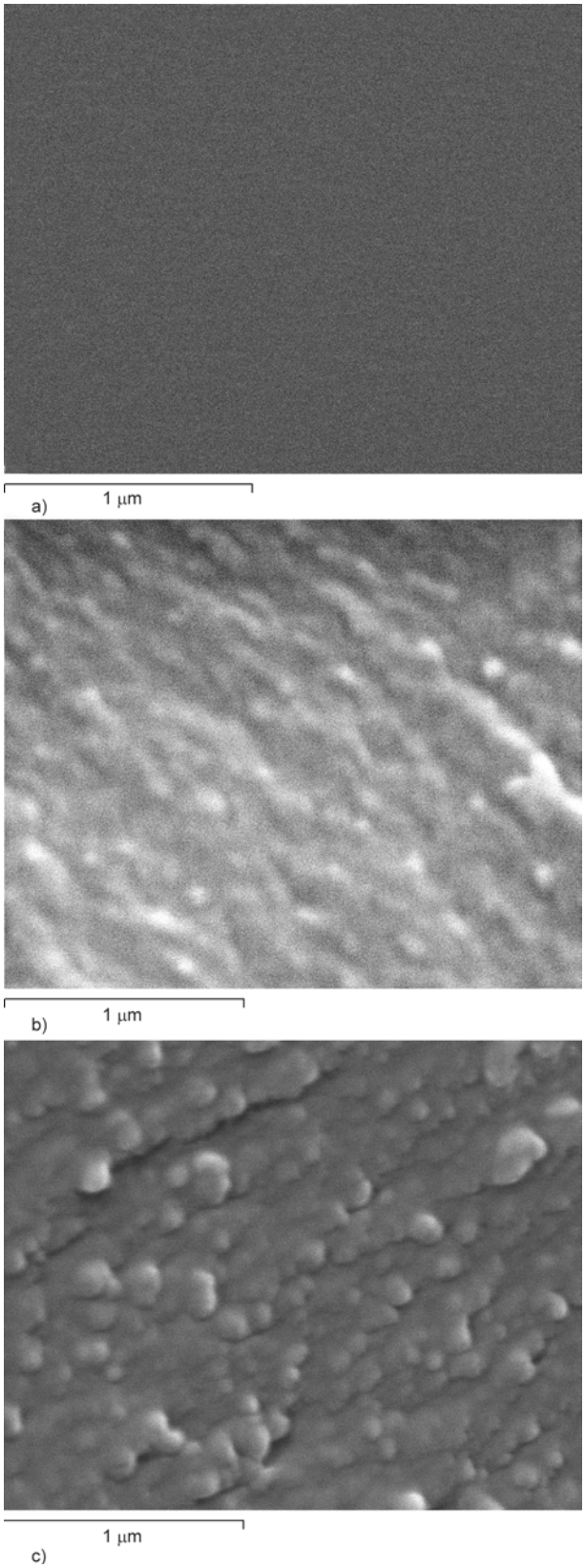

Figure 10. SEM micrographs at 50000 magnifications of the fractured surfaces of the materials obtained from a) neat, b) 10% PEI8 and c) 10% PEI250 formulations

ent from that of the neat formulation. PEI8 micrographs present nanograined morphology with nanosized grains. This nanopatterned organization can be attributed to the presence of amino groups, which can react during curing with epoxides changing the morphology in the surrounding of the star polymer. In a previous study [20] on the modification of DGEBA/anhydride thermosets with star polymers we could observe that the presence of reactive groups in the star led to homogeneous materials, whereas the blocking of these reactive groups produced nanograined morphology. In the present case, PEI8 has a high content of blocked groups and a low content of amine reactive groups, leading to the nanostructure observed by SEM inspection. PEI250 thermosets show a phase-separated morphology with nanosized (75 to 150 nm) fine particles well adhered to the epoxy/anhydride matrix. It can be hypothesized that these particles are formed by PEI250 surrounded by epoxy/anhydride matrix covalently bonded to PEI250 but some aggregation of star polymers cannot be excluded. The differences between two morphologies can be attributed to the different molecular weight of the star polymer and to the amount of amine groups of star polymer that reacts during curing. Although both morphologies lead to significant toughness enhancement in the materials, phase-separated morphology produces a slightly higher improvement than nanograined morphology.

4. Conclusions

The curing of epoxy/anhydride systems in the presence of PEI8 and PEI250 and tertiary amines mainly proceeds by anionic alternating copolymerization catalyzed by tertiary amines, although the uncatalyzed epoxy-anhydride polycondensation and the epoxy-amine reaction can take place to some extent.

The addition of star polymers with poly(ethyleneimine) cores and blocked poly(ε-caprolactone) arms to epoxy/anhydride formulations allows to obtain thermosets with significant improved toughness and low thermal stress generation during cooling, with only a slight reduction on glass transition temperature and crosslinking density.

The flexibility and molecular weight of the star modifiers used, as well as the amount of amino reactive groups in the modifier affect the morphology of the

resulting thermosets but only slightly their thermomechanical properties and curing process. The use of high molecular weight modifier with blocked terminal groups leads to phase-separated morphologies with nano-sized fine particles well adhered to the epoxy/anhydride matrix by the presence of unreacted amine groups.

Acknowledgements

The authors would like to thank MICINN (Ministerio de Ciencia e Innovación) and FEDER (Fondo Europeo de Desarrollo Regional) (MAT2014-53706-C03-01 and MAT2014-53706-C03-02) and to the Comissionat per a Universitats i Recerca del DIUE de la Generalitat de Catalunya (2014-SGR-67).

References

[1] May C. A.: Introduction to epoxy resins. in 'Epoxy resins. Chemistry and technology' (ed.: May C. A.) Marcel Dekker, New York, 1–8 (1988).

[2] Bauer R. S.: Epoxy resin chemistry I. American Chemical Society, Washington (1979).

[3] Pascault J. P., Williams R. J. J.: Epoxy polymers: New materials and innovations. Wiley-VCH, Weinheim (2010).

[4] Lange J., Toll S., Månson J-A. E.: Residual stress build-up in thermoset films cured above their ultimate glass transition temperature. Polymer, **36**, 3135–3141 (1995). DOI: 10.1016/0032-3861(95)97876-H

[5] Thomas R., Durix S., Sinturel C., Omonov T., Goossens S., Groeninckx G., Moldenaers P., Thomas S.: Cure kinetics, morphology and miscibility of modified DGEBA-based epoxy resin – Effects of a liquid rubber inclusion. Polymer, **48**, 1695–1710 (2007). DOI: 10.1016/j.polymer.2007.01.018

[6] Mijovic J., Shen M., Sy J. W., Mondragon I.: Dynamics and morphology in nanostructured thermoset network/block copolymer blends during network formation. Macromolecules, **33**, 5235–5244 (2000). DOI: 10.1021/ma991894e

[7] Choi J., Yee A. F., Laine R. M.: Toughening of cubic silsesquioxane epoxy nanocomposites using core–shell rubber particles: A three-component hybrid system. Macromolecules, **37**, 3267–3276 (2004). DOI: 10.1021/ma0303723

[8] Mezzenga R., Boogh L., Månson J-A. E.: A review of dendritic hyperbranched polymer as modifiers in epoxy composites. Composites Science and Technology, **61**, 787–795 (2001). DOI: 10.1016/S0266-3538(01)00022-7

[9] Morell M., Ramis X., Ferrando F., Serra A.: Effect of polymer topology on the curing process and mechanical characteristics of epoxy thermosets modified with linear or multiarm star poly(ε-caprolactone). Polymer, **52**, 4694–4702 (2011). DOI: 10.1016/j.polymer.2011.07.040

[10] Ratna D., Varley R., Simon G. P.: Toughening of trifunctional epoxy using an epoxy-functionalized hyperbranched polymer. Journal of Applied Polymer Science, **89**, 2339–2345 (2003). DOI: 10.1002/app.12059

[11] Flores M., Fernández-Francos X., Ferrando F., Ramis X., Serra A.: Efficient impact resistance improvement of epoxy/anhydride thermosets by adding hyperbranched polyesters partially modified with undecenoyl chains. Polymer, **53**, 5232–5241 (2012). DOI: 10.1016/j.polymer.2012.09.031

[12] Lagunas C., Fernández-Francos X., Ferrando F., Flores M., Serra A., Morancho J. M., Salla J. M., Ramis X.: New epoxy thermosets modified with amphiphilic multiarm star polymers as toughness enhancer. Reactive and Functional Polymers, **83**, 132–143 (2014). DOI: 10.1016/j.reactfunctpolym.2014.07.022

[13] Tomuta A., Ramis X., de la Flor S., Serra A.: Influence of end groups in hyperbranched polyesters used as modifiers in the characteristics of epoxy thermosets cured by adipic dihydrazide. Express Polymer Letters, **7**, 595–606 (2013). DOI: 10.3144/expresspolymlett.2013.57

[14] Luo L., Meng Y., Qui Y., Li X.: An epoxy-ended hyperbranched polymer as a new modifier for toughening and reinforcing in epoxy resin. Journal of Applied Polymer Science, **130**, 1064–1073 (2013). DOI: 10.1002/app.39257

[15] Zhang D., Chen Y., Jia D.: Toughness and reinforcement of diglycidyl ether of bisphenol-A by hyperbranched poly(trimellitic anhydride-butanediol glycol) ester epoxy resin. Polymer Composites, **30**, 918–925 (2009). DOI: 10.1002/pc.20633

[16] Liu T., Nie Y., Chen R., Zhang L., Meng Y., Li X.: Hyperbranched polyether as an all-purpose epoxy modifier: Controlled synthesis and toughening mechanisms. Journal of Materials Chemistry A, **3**, 1188–1198 (2015). DOI: 10.1039/c4ta04841e

[17] Acebo C., Fernández-Francos X., Ferrando F., Serra A., Salla J. M., Ramis X.: Multiarm star with poly(ethyleneimine) core and poly(ε-caprolactone) arms as modifiers of diglycidylether of bisphenol A thermosets cured by 1-methylimidazole. Reactive and Functional Polymers, **73**, 431–441 (2012). DOI: 10.1016/j.reactfunctpolym.2012.11.007

[18] Acebo C., Fernández-Francos X., Ferrando F., Serra A., Ramis X.: New epoxy thermosets modified with multiarm star poly(lactide) with poly(ethyleneimine) as core of different molecular weight. European Polymer Journal, **49**, 2316–2326 (2013). DOI: 10.1016/j.eurpolymj.2013.05.015

[19] Morell M., Erber M., Ramis X., Ferrando F., Voit B., Serra A.: New epoxy thermosets modified with hyperbranched poly(ester-amide) of different molecular weight. European Polymer Journal, **46**, 1498–1509 (2010). DOI: 10.1016/j.eurpolymj.2010.04.015

[20] Acebo C., Picardi A., Fernández-Francos X., de la Flor S., Ramis X., Serra A.: Effect of hydroxyl ended and end-capped multiarm star polymers on the curing process and mechanical characteristics of epoxy/anhydride thermosets. Progress in Organic Coatings, **77**, 1288–1298 (2014).
DOI: 10.1016/j.porgcoat.2014.04.014

[21] González S., Fernández-Francos X., Salla J. M., Serra A., Mantecón A., Ramis X.: New thermosets obtained by cationic copolymerization of DGEBA with γ-caprolactone with improvement in the shrinkage. II. Time–temperature–transformation (TTT) cure diagram. Journal of Applied Polymer Science, **104**, 3406–3416 (2007).
DOI: 10.1002/app.26021

[22] Flores M., Fernández-Francos X., Ramis X., Serra A.: Novel epoxy-anhydride thermosets modified with a hyperbranched polyester as toughness enhancer. I. Kinetics study. Thermochimica Acta, **544**, 17–26 (2012).
DOI: 10.1016/j.tca.2012.06.008

[23] Benabdi M., Roche A. A.: Mechanical properties of thin and thick coatings applied to various substrates. Part I. An elastic analysis of residual stresses within coating materials. Journal of Adhesion Science and Technology, **11**, 281–299 (1997).
DOI: 10.1163/156856197X00363

[24] Fernández-Francos X., Rybak A., Sekula R., Ramis X., Serra A.: Modification of epoxy–anhydride thermosets using a hyperbranched poly(ester-amide): I. Kinetic study. Polymer International, **61**, 1710–1725 (2012).
DOI: 10.1002/pi.4259

[25] Santiago D., Fernández-Francos X., Ramis X., Salla J. M., Sangermano M.: Comparative curing kinetics and thermal–mechanical properties of DGEBA thermosets cured with a hyperbranched poly(ethyleneimine) and an aliphatic triamine. Thermochimica Acta, **526**, 9–21 (2011).
DOI: 10.1016/j.tca.2011.08.016

[26] Fernández-Francos X., Santiago D., Ferrando F., Ramis X., Salla J. M., Serra A., Sangermano M.: Network Structure and thermomechanical properties of hybrid DGEBA Networks cured with 1-methylimidazole and hyperbranched poly(ethyleneimine)s. Journal of Polymer Science Part B: Polymer Physics, **50**, 1489–1503 (2012).
DOI: 10.1002/polb.23145

[27] Mauri A. N., Riccardi C. C.: The effect of epoxy excess on the kinetics of an epoxy–anhydride system. Journal of Applied Polymer Science, **85**, 2342–2349 (2002).
DOI: 10.1002/app.10867

[28] Rocks J., Rintoul L., Vohwinkel F., George G.: The kinetics and mechanism of cure of an amino-glycidyl epoxy resin by a *co*-anhydride as studied by FT-Raman spectroscopy. Polymer **45**, 6799–6811 (2004).
DOI: 10.1016/j.polymer.2004.07.066

[29] Leonard J.: Heats and entropies of polymerization, ceiling temperatures, equilibrium monomer concentrations, and polymerizatbility of heterocyclic compounds. in 'Polymer handbook' (eds.: Brandrup J., Immermut E. H., Grulke E. A.) Wiley-Intersecience, New York, Vol 1, II/363–II/407 (1999).

[30] Dušek K., Luňák S., Matějka L.: Gelation in the curing of epoxy resins with anhydrides. Polymer Bulletin **7**, 144–152 (1982).
DOI: 10.1007/BF00265465

[31] Mauri A. N., Galego N., Riccardi C. C., Williams R. J. J.: Kinetic model for gelation in the diepoxide–cyclic anhydride copolymerization initiated by tertiary amines. Macromolecules, **30**, 1616–1620 (1997).
DOI: 10.1021/ma9614048

[32] Fernandez-Francos X., Ramis X., Serra A.: From curing kinetics to network structure: A novel approach to the modeling of the network buildup of epoxy–anhydride thermosets. Journal of Polymer Science Part A: Polymer Chemistry, **52**, 61–75 (2014).
DOI: 10.1002/pola.26972

[33] Liu T., Nie Y., Zhang L., Chen R., Meng Y., Li X.: Dependence of epoxy toughness on the backbone structure of hyperbranched polyether modifiers. RCS Advances, **5**, 3408–3416 (2015).
DOI: 10.1039/c4ra10974k

[34] Miao X., Meng Y., Li X.: A novel all-purpose epoxy-terminated hyperbranched polyether sulphone toughener for an epoxy/amine system. Polymer, **60**, 88–95 (2015).
DOI: 10.1016/j.polymer.2015.01.034

[35] Pascault J. P., Sautereau H., Verdu J., Williams R. J. J.: Thermosetting polymers. Marcel Dekker, New York (2002).

[36] Sue H-J., Garcia-Meitin E. I., Pickelman D. M.: Fracture behavior of rubber-modified high performance epoxies. in 'Polymer toughening' (ed.: Arends C. B.) Marcel Dekker, New York, 131–174 (1996).

[37] Tomuta A., Fernández-Francos X., Ferrando F., Serra A., Ramis X.: New epoxy-anhydride thermosets modified with multiarm stars with hyperbranched polyester cores and poly(ϵ-caprolactone) arms. Polymer-Plastics Technology and Engineering, **53**, 645–654 (2014).
DOI: 10.1080/03602559.2013.869599

eXPRESS Polymer Letters Vol.9, No.9 (2015) 824–837
Available online at www.expresspolymlett.com
DOI: 10.3144/expresspolymlett.2015.77

Effects of benzoxazine resin on property enhancement of shape memory epoxy: A dual function of benzoxazine resin as a curing agent and a stable network segment

T. Tanpitaksit[1], *C. Jubsilp*[2], *S. Rimdusit*[1*]

[1]Polymer Engineering Laboratory, Department of Chemical Engineering, Faculty of Engineering, Chulalongkorn University, 10330 Bangkok, Thailand
[2]Department of Chemical Engineering, Faculty of Engineering, Srinakharinwirot University, 26120 Nakhonnayok, Thailand

Received 9 March 2015; accepted in revised form 4 May 2015

Abstract. An ability of bisphenol-A/aniline based benzoxazine resin (BA-a) to simultaneously acts as a curing agent and a stable or rigid network segment for shape memory epoxy, i.e. a two component system, is demonstrated. This significantly simplifies a formulation of present shape memory epoxy systems, i.e. a three or four component system. A suitable content of BA-a in the aliphatic epoxy (NGDE)/polybenzoxazine (PBA-a) samples for good shape memory performance is in a range of 30 to 50 mol%. The storage modulus of the obtained NGDE/PBA-a shape memory polymers (SMPs) was increased from 3.57 GPa for 30 mol% BA-a content to 4.50 GPa for 50 mol% BA-a content. Glass transition temperature of the sample was also substantially increased with increasing BA-a fraction, i.e. from 51°C to 140°C. Flexural modulus and strength at room temperature of the samples at 50 mol% BA-a were found to be as high as 3.97 GPa and 132 MPa compared to the maximum values of 2.54 GPa and 100 MPa of SMP based on cyanate ester-epoxy. All samples exhibited a high value of shape fixity close to 100%. A presence of the BA-a in the samples also imparted a greater recovery stress ranging from 0.25 to 1.59 MPa. Consequently, the obtained NGDE/PBA-a copolymers are highly attractive for shape memory materials to be used in a broader range of applications particularly at elevated temperature and a higher recovery stress value.

Keywords: *polymer blends and alloys, smart polymer, shape memory polymers, polybenzoxazine, aliphatic epoxy*

1. Introduction

Shape memory polymers (SMPs) belong to a novel class of smart materials having been a topic of active research since 1980s, particularly in the past few years [1–7]. They possess an ability to return from a temporary shape to their permanent shape induced by external stimuli such as light, humidity, solvents, electric or magnetic fields, ionic strength, pH or most typically thermal activation [8]. Interestingly, SMPs have a number of advantages over shape memory metal alloys (SMAs) such as light weight, high elastic deformation with a strain value as high as 200%, a broad range of application temperatures which can be tailored, ease of manipulation, potential biocompatibility and biodegradability as well as cost competitiveness [5, 9]. SMPs have a wide application range in self-deployable structures in spacecraft [1, 10], orthodontic applications, intelligent medical devices [5, 9] or smart textiles and apparels [11].

In general, SMPs can be either thermoplastics, i.e. polyethylene [2] and polyester [5] or thermosetting polymers such as epoxy [12, 13] or polyurethane [14, 15]. In case of SMP thermoplastics, their networks can be constructed with physical crosslinks by physical interactions. This characteristic will allow very easy reshaping or re-formation of this class of poly-

*Corresponding author, e-mail: sarawut.r@chula.ac.th

mers. However, they can potentially melt at high temperature, and lose their memory properties over time [16]. Contrarily, chemical crosslinks by covalent bonds can be formed for thermoset SMPs; they soften but do not melt at elevated temperature [4, 17]. As a consequence, thermosetting SMPs, especially epoxy-based SMPs, have been highly attractive particularly in advanced applications [13, 18, 19]. To further broaden the useful property range of shape memory epoxy, epoxy-based shape memory copolymers and epoxy-based shape memory composites have also been developed [18–21]. Recently, Xie and Rousseau [20] had developed methods to tailor transition temperature (T_g) and shape recovery properties of SMPs based on aromatic epoxy as hard segments, aliphatic epoxy as soft segments and aliphatic amine as curing agents. The authors reported that all of their crosslinked epoxy samples showed good SMP characteristics, including excellent shape fixity with shape recovery close to 100% as well as easily tailored thermal transition temperatures ranging from room temperature to 89°C. However, in polymerization step of oxirane group containing epoxy, the resin requires a suitable curing agent. In general, epoxy curing agents, i.e. aromatic amines possess some drawbacks such as relatively low elongation and rather slowly curing for epoxy resin as well as serious toxicity concerning in some cases and corrosion to the processing apparatus [22]. In addition, they show no direct benefit to the shape memory performance of the obtained shape memory epoxy.

Benzoxazine resin, a novel class of thermosetting phenolics [23], has been developed in 1990s to solve various inherent problems occurred in traditional phenolics. For example, the resin can undergo ring-opening polymerization upon heating without strong acid or base catalysts; therefore, no condensation by-product is released during a curing process. This eliminates the formation of voids or air gaps in the fully cured products that normally occur in phenolic resin. A very low A-stage viscosity of the resin results in its high processing ability including ease of filler wetting and high filler loadings [24–26]. The polymer from this resin has been reported to show high thermal stability, excellent mechanical performance, good dimensional stability and relatively high glass transition temperature even though they exhibit relatively low crosslinking density [23, 27, 28]. More importantly, the benzoxazine resin has been shown to be able to blend with various types of resins or polymers to provide even broader spectrum of the copolymer properties. As exemplified, benzoxazine resin had been shown to be able to function as a latent curing agent for epoxy resin and, in some cases, provide synergism in thermal and mechanical properties of the obtained benzoxazine/epoxy copolymers [27, 29–31]. Very recently, shape memory polymers between bisphenol-A/aniline based benzoxazine resin (BA-a) and shape memory polyurethane (SMPU) have been investigated by Erden and Jana [32]. From their investigation, the authors suggested that the BA-a can be either chemically bonded with SMPU chains by copolymerization or grafting reactions or blended with SMPU as a separate phase. Furthermore, the polybenzoxazine (PBA-a) can act as an additional hard phase for the SMPU due to its higher glass transition temperature and much greater storage modulus than the soft segment phase of the SMPU. An addition with only 17 wt% of the BA-a in the SMPU rendered a recovery stress and shape recovery ratio as high as 13 MPa and 93%, which was substantially higher than those of the starting SMPU, i.e. 6.8 MPa and 72%. In addition, Rimdusit *et al.* [7] have recently developed shape memory polymer copolymers based on bisphenol-A/ aniline based benzoxazine resin (BA-a), aliphatic-aromatic epoxy mixture, and Jeffamine D230 as the epoxy curing agent. Enhanced thermomechanical performance of the obtained epoxy SMPs was achieved by an addition of the BA-a fraction. The incorporation of the BA-a contributed to higher storage modulus in the glassy state, higher crosslink density, enhanced flexural strength, and greater flexural modulus at room temperature. Moreover, the recovery stress of the obtained SMPs was reported to increase with increasing BA-a content up to 33 mol% with the reported recovery stress of about 38 kPa. It was 1.8 times higher comparing with 20.4 kPa of the unmodified shape memory epoxy.

The purpose of this study is to investigate the potential use of bisphenol-A/aniline based benzoxazine resin (BA-a) as a sole curing agent for aliphatic shape memory epoxy. Moreover, it is expected that the aromatic structure of the BA-a can act as a hard or stable phase for the aliphatic epoxy network thus eliminate the need for aromatic epoxy that is normally added in typical shape memory epoxy products. Twofold benefits are expected from this aliphatic epoxy/benzoxazine SMPs, i.e. (1) a potential improvement of thermomechanical properties and

recovery stress of the copolymer samples with an addition of the more rigid polybenzoxazine and (2) a simpler shape memory epoxy formulation from the dual function of the BA-a above. Some essential properties, such as glass transition temperature, flexural modulus, flexural strength, recovery stress and shape recovery performance will also be investigated.

2. Experimental

2.1. Materials

Materials used in this study was bisphenol-A/aniline-based benzoxazine resin (BA-a). The BA-a was synthesized according to the solventless technology [23, 33]. Bisphenol-A (polycarbonate grade) was provided by Thai Polycarbonate Co., Ltd. (Rayong, Thailand). Para-formaldehyde (AR grade) and aniline (AR grade) was purchased from Merck Co., Ltd. (Darmstadt, Germany) and Panreac Quimica, S.A. (Barcelona, Spain), respectively. Aliphatic epoxy (Neopentyl glycol diglycidyl ether; NGDE) was available from Aditya Birla Chemicals Thailand Ltd. (Rayong, Thailand). All chemicals were used as received. The NGDE/BA-a mixtures at different mole percent of the BA-a varied from 30 to 50 mol% were prepared. The mixture was heated at about 80°C in an aluminum pan and stirred for about 15 min to yield a homogeneous mixture. The molten resin was poured into an aluminum mold and was thermally cured at 80°C for 2 h in vacuum oven and 130°C/12 h, 140°C/4 h, 150°C/4 h and 160°C/2 h, respectively, in an air circulated oven. Then, the cured NGDE/polybenzoxazine (PBA-a) shape memory samples were cut into various shapes for each specific test.

2.2. Characterization methods

Curing behaviors of the BA-a, NGDE and NGDE/BA-a mixtures were studied using a differential scanning calorimeter (DSC) model 2910 from TA Instruments (New Castle, DE, United States). Each sample with a mass in a range of 3–5 mg was sealed in an aluminum pan with lid. The heating rate used was 5 and 10°C/min and the sample temperature was scanned from room temperature to 320°C under nitrogen purging with the gas flow rate of 50 mL/min. The degree of conversion of a sample was determined according to the relationship in Equation (1):

$$\text{Conversion}\,[\,\%\,] = \left(1 - \frac{H_{\text{rxn}}}{H_0}\right)\cdot 100 \qquad (1)$$

where H_{rxn} is the heat of reaction of the partially cured samples and H_0 is the heat of reaction of the uncured resin mixture.

Chemical structure and network formation of all samples was studied by a Fourier transform infrared spectroscopy (FTIR), a Spectrum GX FT-IR spectometer from Perkin Elmer with an ATR accessory (Waltham, Massachusetts, United States). All spectra were taken as a function of time with 64 scans at a resolution of 4 cm^{-1} and wavenumber ranging from 4000–650 cm^{-1}. For viscous liquid NGDE/BA-a mixtures, a small amount of mixture was casted as thin film on a potassium bromide (KBr) window and its FTIR spectrum was obtained.

Dynamic mechanical analyzer (DMA) model DMA242 from Netzsch, Inc. (Bavaria, Germany) was used to determine a storage modulus (E') and loss tangent ($\tan\delta$) of the NGDE/PBA-a shape memory samples. The sample in rectangular shape, with a dimension of 10 mm×50 mm×3 mm, was tested using a three-point bending mode with 40 mm supporting span at the frequency of 1 Hz and a heating rate of 2°C/min from room temperature to the temperature beyond the glass transition temperatures (T_g) of each sample. The T_g was taken as the maximum peak on the loss tangent curve in the DMA thermogram.

Flexural properties of NGDE/PBA-a shape memory samples were measured according to ASTM D 790M using a universal testing machine (model 5567) from Instron (Thailand) Co., Ltd. (Bangkok, Thailand). The test method was a three-point bending load with a supporting span of 32 mm and tested at a crosshead speed of 1.0 mm/min. A dimension of a rectangular shape sample was 10 mm×50 mm×2 mm.

A systematic shape recovery test of NGDE/PBA-a shape memory samples under bending load was also performed. The procedure for the thermomechanical bending cycling of NGDE/ PBA-a shape memory samples includes the following steps: firstly, the sample in its permanent shape was kept in an oven for 20 min at T_g + 20°C; then the sample was bent to a storage angle θ_0 in a 'U' shape with the radius of 2 mm in the soft rubbery state, after that the sample was kept at room temperature with the external con-

straint to freeze the elastic deformation energy for 20 min. The sample fixed on the apparatus was then immersed into air circulated oven at elevated temperature, and it recovered to an angle θ_N [34]. The value of the shape recovery ratio (R_N) can be calculated by Equation (2):

$$R_N = \frac{\theta_0 - \theta_N}{\theta_0} \cdot 100\% \quad (2)$$

Shape fixity and recovery stress of NGDE/PBA-a shape memory samples were studied by a universal testing machine under three point bending mode. The experimental procedure for the shape fixity and recovery stress was performed using the same method as described in [35]. Firstly, a fixed shape was formed by applying force to a sample (10 mm×50 mm× 2 mm) at T_g + 20°C and left to cool down to room temperature. The force was then removed completely to obtain a temporary shape. The deflection after unloading was then measured, and shape fixity (R_f) of each sample was determined. In addition, the sample was also heated up to T_g + 20°C by keeping the fixed deflection content, afterwards, deflection force of each sample during heating was measured and the coresponding recovery stress was obtained.

3. Results and discussion

3.1. Effects of BA-a contents on curing behaviors of NGDE/BA-a mixtures

Curing characteristics of aliphatic epoxy (NGDE)/ benzoxazine resin (BA-a) mixtures at BA-a contents of 30, 40 and 50 mol% were studied by a differential scanning calorimeter (DSC) at a heating rate 5°C/min as shown in Figure 1. The thermogram of the BA-a showed a curing exothermic peak located at about 210°C, while the NGDE showed no sign of any curing reaction in this temperature range because no initiators or catalysts were added to the resin. Instead the endothermic thermal event starting at about 200°C a result of the evaporation process of the NGDE was observed. For the NGDE/BA-a mixtures, the thermograms revealed three exothermic peaks of these resin mixtures. The two overlapping peaks at lower temperature were found to be in a range of 235–240°C whereas the third peak at high temperature were observed at temperature about 275–285°C. Both peaks tended to shift to higher temperature with increasing epoxy content. The phenomenon is attributed to diluent effect of the liquid epoxy on benzoxazine curing [29]. Furthermore, the

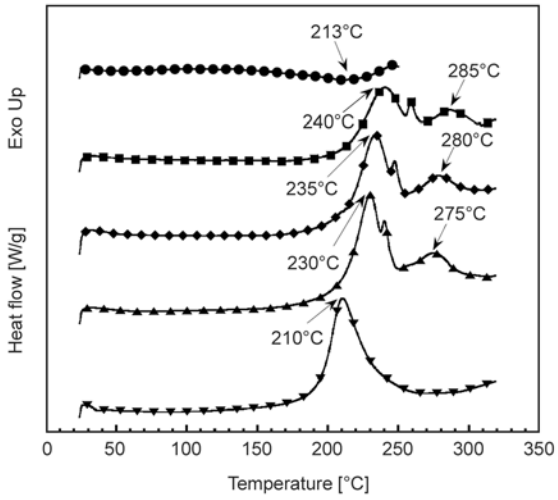

Figure 1. DSC thermograms of NGDE/BA-a mixtures at various mole percents of BA-a: (●) NGDE, (■) 30 mol%, (◆) 40 mol%, (▲) 50 mol%, (▼) BA-a

reactions between the BA-a and the NGDE were found to comprise of at least two major reactions. The first reaction at the two overlapping exothermic peak at lower temperature is attributed to the polymerization reaction of the BA-a monomers, whereas the third exothermic peak at a higher temperature is the reaction between the phenolic hydroxyl group of the polybenzoxazine (PBA-a) and the epoxide group of the NGDE. This result is in good agreement with the curing behaviors of bisphenol-A based epoxy by the BA-a [29, 36].

Figure 2 illustrates DSC thermograms at a heating rate 10°C/min of the NGDE/BA-a mixture at 50 mol% of the BA-a content at various curing conditions. The optimal curing conditions of the NGDE/ BA-a mixtures were determined from the partial disappearance of the area under the curve of the exothermic peak in the DSC experiment. The heat of reaction of the uncured sample was measured to be 272.0 J/g. After a step curing at 130°C/12 h, 140°C/4 h, 150°C/4 h and 160°C/2 h, the values decreased to 245.6, 236.7, 231.7 and 101.4 J/g, respectively, which corresponded to the degree of conversion of 9.7, 12.9, 14.8 and 62.7%. Liu *et al.* [37] suggested that the degree of conversion about 60% of shape memory epoxy provided samples with good balance properties between shape memory performance and thermomechanical properties. The fully cured samples, i.e. 100% conversion, were reported to give samples with too high crosslink density thus resulting in great reduction in molecular chain mobility and poorer shape memory perform-

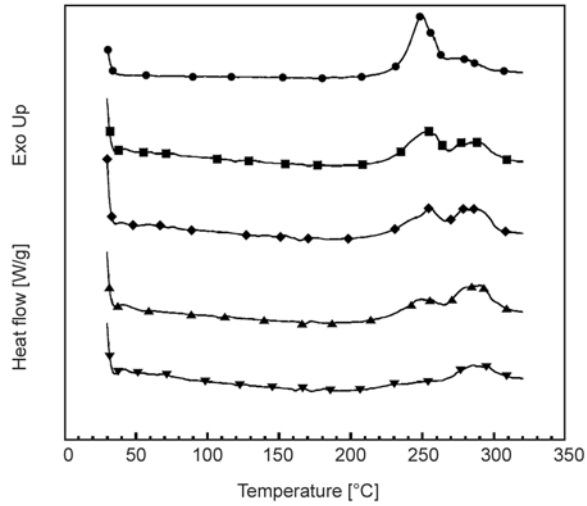

Figure 2. DSC thermograms of NGDE/BA-a samples at 50 mol% BA-a at various curing conditions: (●) uncured, (■) 130°C/12 h, (◆) 130°C/12 h + 140°C/4 h, (▲) 130°C/12 h + 140°C/4 h + 150°C/4 h, (▼) 130°C/12 h + 140°C/4 h + 150°C/4 h + 160°C/2 h

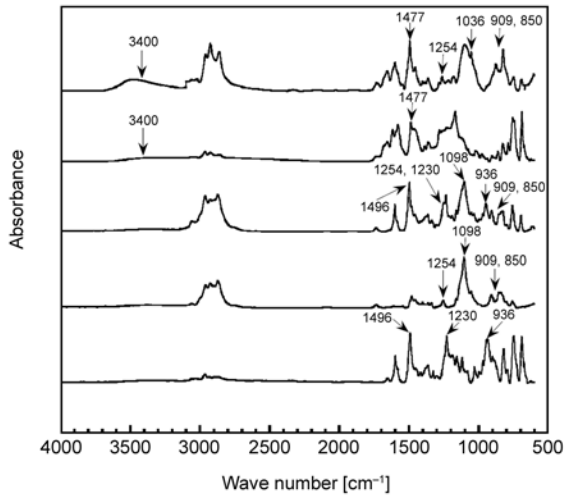

Figure 3. FTIR spectra of (a) BA-a, (b) NGDE, (c) NGDE/BA-a mixture at 50 mol% BA-a, (d) PBA-a, (e) NGDE/PBA-a copolymer at 50 mol% BA-a

ance. Therefore, the curing process under the above step cure conditions to achieve approximately 60% conversion was used in our work to cure all NGDE/BA-a mixtures preparing the NGDE/PBA-a shape memory samples for further characterizations.

3.2. Fourier transform infrared spectroscopy (FTIR) of BA-a/NGDE network formation

Chemical structures of benzoxazine resin (BA-a), aliphatic epoxy (NGDE) and their network formation were studied by FTIR spectroscopy. Figure 3 shows FTIR spectra taken from the BA-a, the NGDE and the NGDE/BA-a mixture at 50 mol% BA-a. The characteristic IR absorption bands of the BA-a were found at 1230 cm^{-1} assigned to C–O–C stretching mode of benzene ring and 1496 and 936 cm^{-1} assigned to tri-substituted benzene ring as shown in Figure 3 curve a [23, 38]. The IR absorption bands of the NGDE were observed at 1098 cm^{-1} assigned to C–O–C stretching mode of ethers as well as the peaks at 1254, 909 and 850 cm^{-1} assigned to epoxide ring mode [33] as depicted in Figure 3 curve b. In Figure 3 curve c, it was evidently confirmed by FTIR that the NGDE/BA-a mixture contained both BA-a and NGDE characteristic IR absorptions, such as those at 1496 and 936 cm^{-1} from the BA-a species and that of 1254, 909 and 850 cm^{-1} from epoxide ring of the NGDE.

The network formation between the BA-a and the NGDE after thermal cure were also monitored by FTIR. Figures 3a and 3d showed FTIR spectra taken from the BA-a and the polybenzoxazine (PBA-a). For BA-a polymerization process, the oxazine ring was opened by the breakage of a C–O bond of the ring. Then, the BA-a molecules were transformed from a ring structure to a network structure. During this process, the tri-substituted benzene ring, backbone of BA-a ring, became tetra-substituted benzene ring [23, 38]. The ring-opening polymerization of the BA-a was observed from the decrease of the absorption bands at 1496, and 936 cm^{-1} and the appearance of the new absorption band at 1477 cm^{-1} of the tetra-substituted benzene ring. In addition, a broad intensive IR absorption band appeared at 3400 cm^{-1} was assigned to O–H groups of the phenolic hydroxyl group that can react with epoxide group in the NGDE for ring opening polymerization. Moreover, the FTIR spectra of the NGDE/BA-a mixture at 50 mol% BA-a before and after polymerization were also shown in Figures 3c and 3e. After being step cured at 160°C for 2 h. The absorption band at 1477 cm^{-1} of the PBA-a was also found in the NGDE/PBA-a copolymers whereas the absorption bands at 1254 (vibration modes), 909 and 850 cm^{-1} (asymmetric stretching) assigned to the remained epoxide group appeared. Therefore, it can be suggested that epoxide groups can react with the phenolic hydroxyl group of the ring opened BA-a monomers to form new ether linkages and hydroxyl groups in epoxy moieties [39] as clearly seen the absorption bands at 1036 and 3400 cm^{-1}, respectively, in Figure 3 curve e. A possible chemical reaction

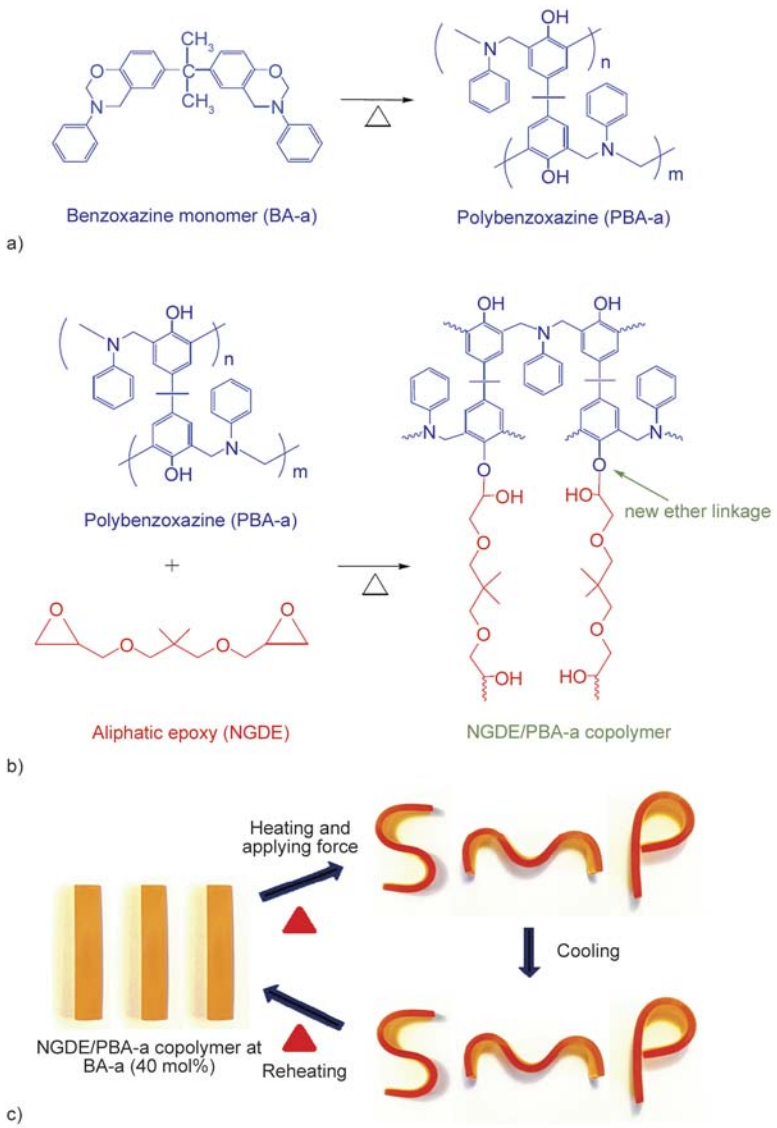

Figure 4. (a) Curing reaction of BA-a, (b) A possible chemical reaction between PBA-a and NGDE and (c) NGDE/PBA-a SMP at original shape, temporary shape and recovered shape at T_g + 20°C

between the BA-a and the NGDE is shown in Figure 4. It was postulated that the BA-a ring was opened by heating at suitable temperature (Figure 4a). The phenolic hydroxyl groups of the ring opened the BA-a monomer then acted as an epoxy curing agent to open the epoxide ring to form the ether linkages in the copolymer networks as proposed in Figure 4b. These results are also in good agreement with the previous reports by our research group [30, 36] and Kimura *et al.* [31] using different types of epoxy resins.

3.3. Dynamic mechanical analysis of NGDE/PBA-a SMPs

Viscoelastic properties served as one key characterization for screening the series of NGDE/PBA-a shape memory polymers (SMPs) for good shape-memory performance. Figure 5 and Figure 6 displays the temperature-dependence of storage modulus (E') and loss tangent (tan δ) of the aliphatic epoxy (NGDE)/polybenzoxazine (PBA-a) shape memory samples. From Figure 5, the storage moduli at a glassy state (35°C) of the NGDE/PBA-a SMPs at BA-a contents of 30, 35, 40, 45 and 50 mol% were measured to be 3.57, 3.79, 3.92, 4.29 and 4.50 GPa, respectively. From the results, the storage moduli of the samples tended to increase with increasing BA-a content. The phenomenon is attributed to the addition of the more rigid molecular segments of the PBA-a in the NGDE/PBA-a shape memory samples. Moreover, to obtain the optimum performance for a shape-memory polymer, the drop in modulus should not only be large and sharp but it should ideally be followed by an extended rubbery plateau

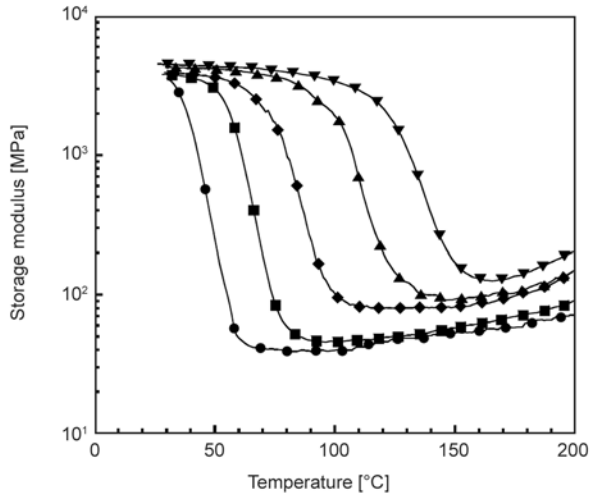

Figure 5. Storage modulus versus temperature of NGDE/PBA-a SMPs at various mole percents of BA-a: (●) 30 mol%, (■) 35 mol%, (◆) 40 mol%, (▲) 45 mol%, (▼) 50 mol%

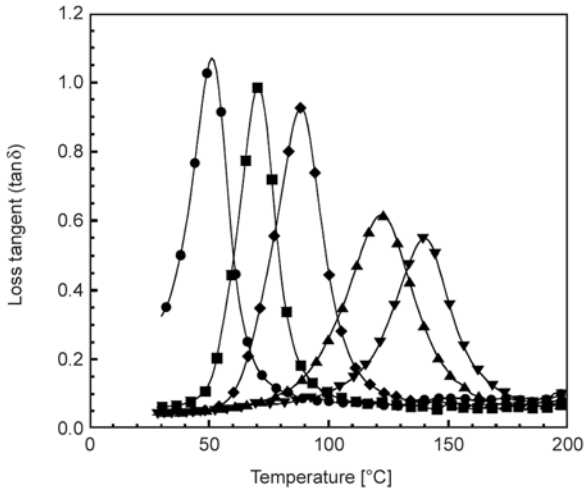

Figure 6. Loss tangent versus temperature of NGDE/PBA-a SMPs at various mole percents of BA-a: (●) 30 mol%, (■) 35 mol%, (◆) 40 mol%, (▲) 45 mol%, (▼) 50 mol%

[40]. As seen in Figure 5, the addition of the BA-a also resulted in a systematic increase of the modulus in rubbery plateau region from 40 to 172 MPa. This characteristic suggested the BA-a to be an effective crosslinker for the aliphatic epoxy. In addition, we can see that a difference of two orders of magnitude of the high elasticity ratio between glassy state modulus (E_g) and rubbery modulus (E_r) was obtained in the SMPs. Therefore, the NGDE/PBA-a SMPs are easy shaping at $T > T_s$ (shape memory temperature) and they show great resistance to deformation at $T < T_s$ [41].

Loss tangent (tan δ) curves from a DMA experiment of the NGDE/PBA-a SMPs at various BA-a contents are depicted in Figure 6. The peak positions of the tan δ were used to indicate T_g of the samples. We can see that, an increase of the BA-a content in the NGDE/PBA-a SMPs resulted in a systematic increase in the T_g of the samples. The T_g of the NGDE/PBA-a samples were 51°C for 30 mol% BA-a, 70°C for 35 mol% BA-a, 88°C for 40 mol% BA-a, 122°C for 45 mol% BA-a and 140°C for 50 mol% BA-a. As a consequence, a wide range of the T_g from 51 to 140°C allowing relatively wide range of service temperature was obtained in these NGDE/PBA-a SMPs. This behavior was attributed to the more rigid molecular structure of the polybenzoxazine compared to the epoxy [42]. Moreover, the peak height of the tan δ corresponding to the strain energy dissipated by viscous friction was observed to decrease with increasing mole percent of the BA-a which suggested the elastic behavior of the NGDE/PBA-a SMPs to be enhanced with the amount of the BA-a crosslinker. We also observed a broader width at half height of the curves which implied network heterogeneity to be more pronounced when the amount of the BA-a increased. However, the transparency and the single peak of tan δ of each sample confirmed the single microscopic domain of the NGDE/PBA-a SMPs implying no phase separation in these copolymers. The single broad T_g or switching transition is desirable in some special cases of shape memory polymers such as in multiple shape memory polymers (MSMPs). Moreover, our samples also showed a relatively broad T_g range covering that of the commercially available epoxy-based shape memory polymer, i.e. Veriflex®E (T_g = 62°C) and styrene-based shape memory polymer, i.e. Veriflex® (T_g = 90°C) from Cornerstore Industries [43].

3.4. Mechanical properties of NGDE/PBA-a SMPs

Mechanical properties, i.e. flexural strength (σ_f) and modulus (E_f) at room temperature of the aliphatic epoxy (NGDE)/polybenzoxazine (PBA-a) SMPs as a function of BA-a content were examined as plotted in Figure 7. It can be seen that the flexural strength of the samples increased with an increase in the amount of the BA-a. The flexural strength of the samples were measured to be 52 MPa for 30 mol% BA-a, 78 MPa for 35 mol% BA-a, 108 MPa for 40 mol% BA-a, 124 MPa for 45 mol% BA-a, and 132 MPa for 50 mol% BA-a. This characteristic was due to the addition of high flexural strength PBA-a,

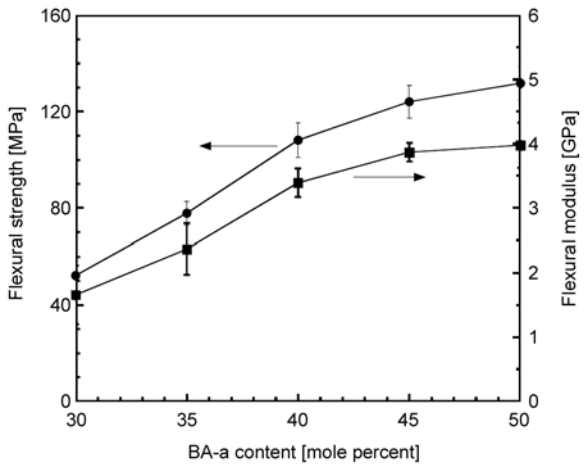

Figure 7. Flexural strength (●) and flexural modulus (■) at room temperature (25°C) of NGDE/PBA-a SMPs at various mole percents of BA-a

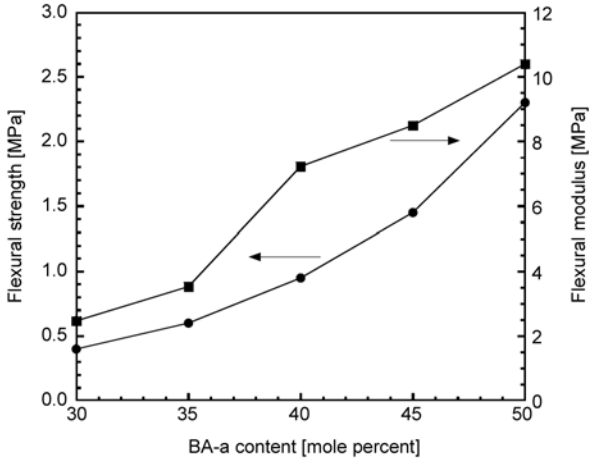

Figure 8. Flexural strength (●) and flexural modulus (■) at T_g + 20°C of NGDE/PBA-a SMPs at various mole percents of BA-a

i.e. σ_f ~ 126–139 MPa [44] and chemical linkage formation between PBA-a with the epoxy network. The NGDE/PBA-a SMPs also rendered flexural strength higher than that of cyanate ester-epoxy shape memory samples, i.e. 14–100 MPa [45]. Moreover, an addition of the BA-a into the NGDE was expectedly found to improve flexural modulus of the NGDE/PBA-a SMPs, i.e. 1.6 GPa for BA-a = 30 mol% to 4.0 GPa for BA-a = 50 mol% as also seen in Figure 7. This is due to the addition of the more rigid PBA-a, i.e. E_f ~ 4.5–5.8 GPa [44] into the more flexible aliphatic epoxy as well as an enhanced crosslink density of the obtained polymer network described previously.

The potential applications in deployable structure of the NGDE/PBA-a SMPs were systematic investigated by flexural testing in the rubbery state (T_g + 20°C). In this work, the flexural testing was carried out on the universal testing machine equipped with the environmental chamber at T_g + 20°C. Figure 8 displayed a plot of flexural strength at T_g + 20°C of the NGDE/PBA-a SMPs at different BA-a contents. The flexural strength at a rubbery state of the samples with BA-a contents of 30, 35, 40, 45 and 50 mol% were measured to be 0.4, 0.6, 0.9, 1.5 and 2.3 MPa, respectively. From the results, the flexural strength at the rubbery state of the samples increased with increasing amount of BA-a similar to what observed in the strength at room temperature. The greater values of flexural strength at the rubbery state of the samples are attributed to the enhancement of crosslink density of the samples as discussed in DMA experiment. The flexural strength at the rubbery state of our NGDE/PBA-a SMPs at 50 mol% BA-a is about 10 times higher than commercial SMPs based on styrene resin (Veriflex®), i.e. 0.23±0.03 MPa [46]. Furthermore, the effects of BA-a contents on flexural modulus at T_g + 20°C of the shape memory samples are illustrated in Figure 8. The addition of the BA-a into the NGDE was found to increase flexural modulus at T_g + 20°C of the samples. The flexural modulus of the samples were ranging from 2.5 MPa for 30 mol% BA-a, up to 10.4 MPa for 50 mol% BA-a. The obtained values are in a same range as that of a commercial thermoset SMP epoxy system (DP7AR), i.e. E_f at T_g + 20°C = 8.51 MPa [12] and a commercial SMPs based on styrene resin (Veriflex®), i.e. 6.48±1.71 MPa [46].

3.5. Effect of BA-a contents on shape fixity of NGDE/PBA-a SMPs

Shape fixity (R_f) is one important shape memory performance indicating an ability to memorize temporary shape of shape memory polymers (SMPs). When SMPs is heated to a temperature above its glass transition temperature (T_g), the sample can develop relatively large deformation. Then, it can be fixed this temporary shape by cooling to a temperature below T_g or room temperature (25°C). Figure 9 showed shape fixity at various fixing temperatures of the NGDE/PBA-a shape memory samples. From the figure, R_fs of the samples were measured to be in a range of 83.1 to 84.5% at T_g – 10°C, 96.5 to 97.4% at T_g – 20°C and 98.1 to 99.3% at 25°C. We can see that the R_f values of all samples at various fixing temperatures decreased slightly by an increase in the BA-a contents from 30 to 50 mol%. The decrease in the shape fixity values with an incorporation of the

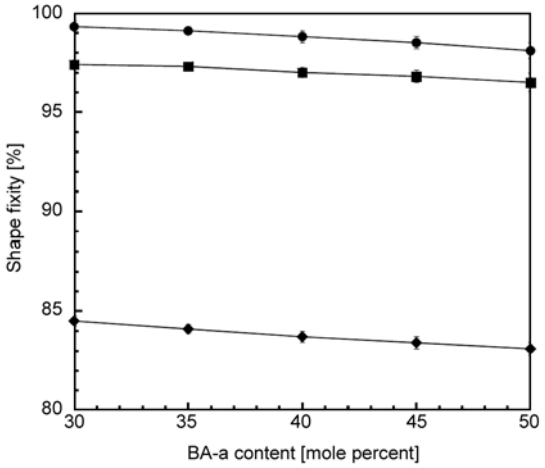

Figure 9. Effect of BA-a contents on shape fixity at different fixing temperatures of NGDE/PBA-a SMPs: (●) room temperature (25°C), (■) T_g – 20°C, (◆) T_g – 10°C

hard rigid phase of the shape memory polymers had also been reported by Ji *et al*. [15]. In their studies, the shape fixity at fixing temperature of T_g – 20°C of polyurethanes (PUs) was reported to decrease from 96% to 84% with an increase of PU hard-segment content from 30% to 50%.

Moreover, it was also found that R_f of the NGDE/PBA-a SMPs comparing at the same BA-a content increased with lower fixing temperature, i.e. from T_g – 10°C to 25°C. This behavior is because some molecular chain segments were unfixed at T_g – 10°C. Therefore, the samples can partially restore to permanent shape that made the samples less controllable of its temporary shape. The shape fixity values at T_g – 20°C and at 25°C are close to 100% because these fixing temperatures were sufficiently low to freeze the motion of the molecular segments. The shape fixities of our samples, i.e. about 83.1–84.5% at T_g – 10°C and 96.5– 97.4% at T_g – 20°C, are still higher than that of polyurethane SMPs (i.e. about 77% at T_g – 10°C and 95% at T_g – 20°C) [47] suggesting a less chain mobility of our polymer network comparing at the same fixing temperature below their T_g above.

3.6. Effect of BA-a contents on shape recovery behaviors of NGDE/PBA-a SMPs

Shape recovery behaviors of the aliphatic epoxy (NGDE)/polybenzoxazine (PBA-a) SMPs were studied using a fold-deploy shape memory test. Bending deformation was widely employed for evaluating shape memory properties of polymer materials due to a large deflection being easily obtained in a range of small strain through bending [48]. Figure 10 presents snapshots of the shape recovery sequence at T_g + 20°C of the sample at 40 mol% BA-a. It can be seen that the sample can fully recover its permanent shape with 100% shape recovery or with recovery angle of 180°. In addition, all of our SMPs, i.e. with benzoxazine resin (BA-a) contents from 30–50 mol%, also displayed shape recovery performance of about 100% at T_g + 20°C. The photographs of NGDE/PBA-a SMP at original shape, temporary shape and recovered shape at T_g + 20°C was presented in Figure 4b. This characteristic suggests that the deformation of stable PBA-a network could be recovered completely if the NGDE/PBA-a SMPs were heated to sufficiently high temperature. In addition, it implies that the NGDE/PBA-a copolymers are covalently crosslinked to form three-dimensional network structures which become reversibly rubbery at above T_g [49].

The effect of BA-a contents on recovery angle as a function of time for the NGDE/PBA-a SMPs under a bending test at T_g and T_g + 20°C, are depicted in Figure 11 and Figure 12, respectively. From the figures, all samples can completely recover to their permanent shape. The recovery time of the SMPs was found to increase with increasing BA-a from 30 to 50 mol%, i.e. from 75 to 145 s at T_g and from 60 to 120 s at T_g + 20°C. Its recovery time is about the same as that of shape memory materials based on epoxy and activity polyurethane (APU) [50] showing recovery time of about 120 s at their T_g. In addition, the curve in Figures 11 and 12 can be divided into three zones. The start stage (at a recovery angle of 0 to 50°), transition stage (a recovery angle of 50 to 150°) and terminal stage (a recovery angle of 150 to 180°). This behavior suggests that the NGDE/PBA-a SMPs have a relative low recovery rate at the start and terminal stage. At the start stage, the release of constrained force was followed by heavy friction among molecules, thus the recovery angle slowly increased. After that, fraction force reduced under the gradual adjustment of segments results in the slopes of recovery angle is sharply as named the transition stage. At the terminal stage, the shape recovery rate becomes slower than the transition stage because the constrained force of the sample had been released due to a little of it remaining [7, 37, 51].

In addition, the shape recovery time of the samples tended to decrease with increasing the active temperature from T_g to T_g + 20°C. This phenomenon is

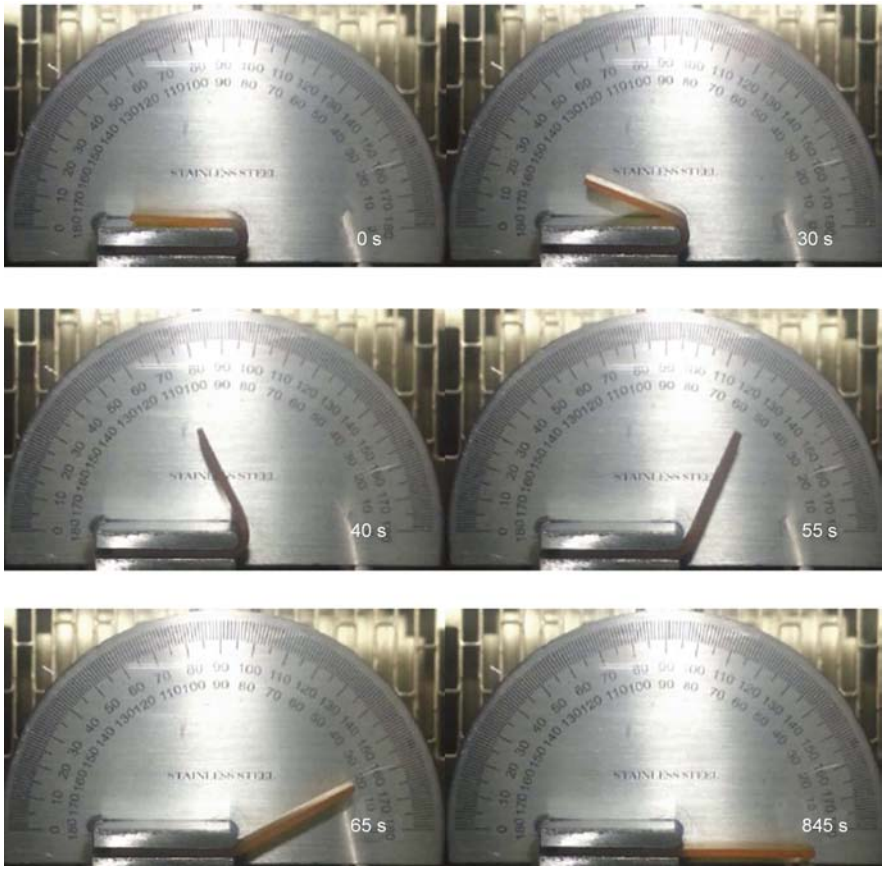

Figure 10. Series of images showed shape recovery of NGDE/PBA-a SMP with 40 mol% BA-a at a T_g + 20°C (108°C). The permanent and temporary shapes are rectangular and U-shape, respectively.

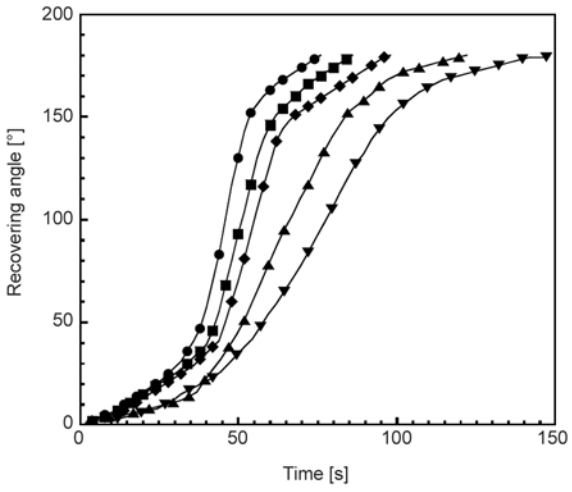

Figure 11. Recovery angle as a function of recovery time during the shape recovery process at a T_g of NGDE/PBA-a SMPs at various mole percents of BA-a: (●) 30 mol%, (■) 35 mol%, (◆) 40 mol%, (▲) 45 mol%, (▼) 50 mol%

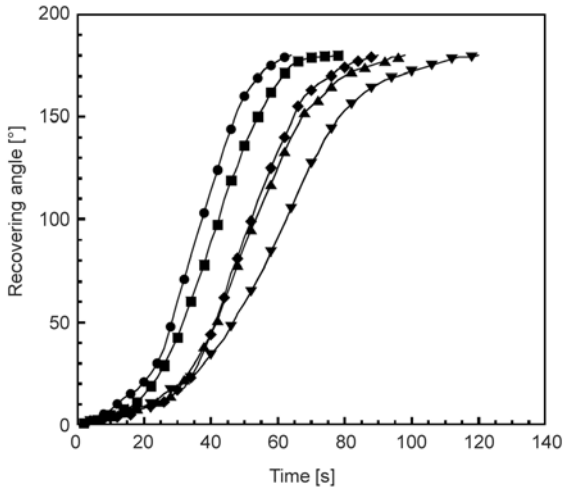

Figure 12. Recovery angle as a function of recovery time during the shape recovery process at a T_g + 20°C of NGDE/PBA-a SMPs at various mole percents of BA-a: (●) 30 mol%, (■) 35 mol%, (◆) 40 mol%, (▲) 45 mol%, (▼) 50 mol%

due to the fact that, at higher temperature, the activated molecular chain segments can move more intensely. Moreover, the shape recovery time of the samples increased with an increasing amount of BA-a content. This implied that the movement of the molecular chain segment of the NGDE/PBA-a shape memory samples could be more restricted with increasing BA-a content since an increasing of storage modulus at rubbery plateau was observed in the DMA results. The recovery times of our SMPs were in the same range as that of epoxy resin E-51 (WSR 618) cured by aromatic amine curing agent [37].

Therefore, the incorporation of the BA-a into the NGDE/PBA-a SMPs can prolong the shape recovery time thus broadening the range of application of these SMPs.

Furthermore, in order to observe the performance of the shape memory behavior over period of time for fixed temporary shape. The NGDE/PBA-a SMP at 40 mol% BA-a was used as a representative sample to demonstrate the shape memory behavior after the time period of 20 min, 7 days, 15 days and 30 days used to fix its temporary shape. The samples showed negligible change in its temporary shape after all time periods. In addition, the time for complete recovery to their permanent shape of these samples after heated up to T_g + 20°C was 84, 85, 85 and 86 s, respectively. This result implied that the performance of the SMPs based on the NGDE/PBA-a copolymers indicates a relatively good shape memory as they can be maintained over a long period of time.

3.7. Effect of BA-a contents on recovery stress of NGDE/PBA-a SMPs

The experimental procedure of the recovery stress test of the aliphatic epoxy (NGDE)/polybenzoxazine (PBA-a) SMPs is depicted in Figure 13. Firstly, the sample at its permanent state was heated to 20°C above T_g (T_g + °C) as seen in Figure 13a. After that it was applied by flexural load during heating at T_g + 20°C until its maximum deflection (y_{max} = 10 mm) as shown in Figure 13b. The deformed state of y_{max} = 10 mm at T_g + 20°C is almost maintained after cooling down to room temperature. Then, the sample was held at room temperature under unloaded condition for 20 min as presented in Figure 13c. Finally, the sample was heated to T_g + 20°C by maintaining the fixed deflection constant as can be seen in Figure 13d. Recovery stress during heating was masured from the transition stage of the shape-fixed stage to the recovery shape stage.

The recovery stress versus time of the SMPs is shown in Figure 14. The maximum recovery stress of the samples were observed to be 0.25, 0.39, 0.62, 0.98 and 1.59 MPa at BA-a contents ranging from 30, 35, 40, 45 and 50 mol%, respectively. As a result, it could be seen that content of the BA-a is an efficient way to increase recovery stress of the SMPs. Recently, the recovery stress obtained from the thermomechanical analysis (TMA) experiments of shape memory polymer based on styrene cured with benzoyl peroxide has been studied [17, 52–54]. It

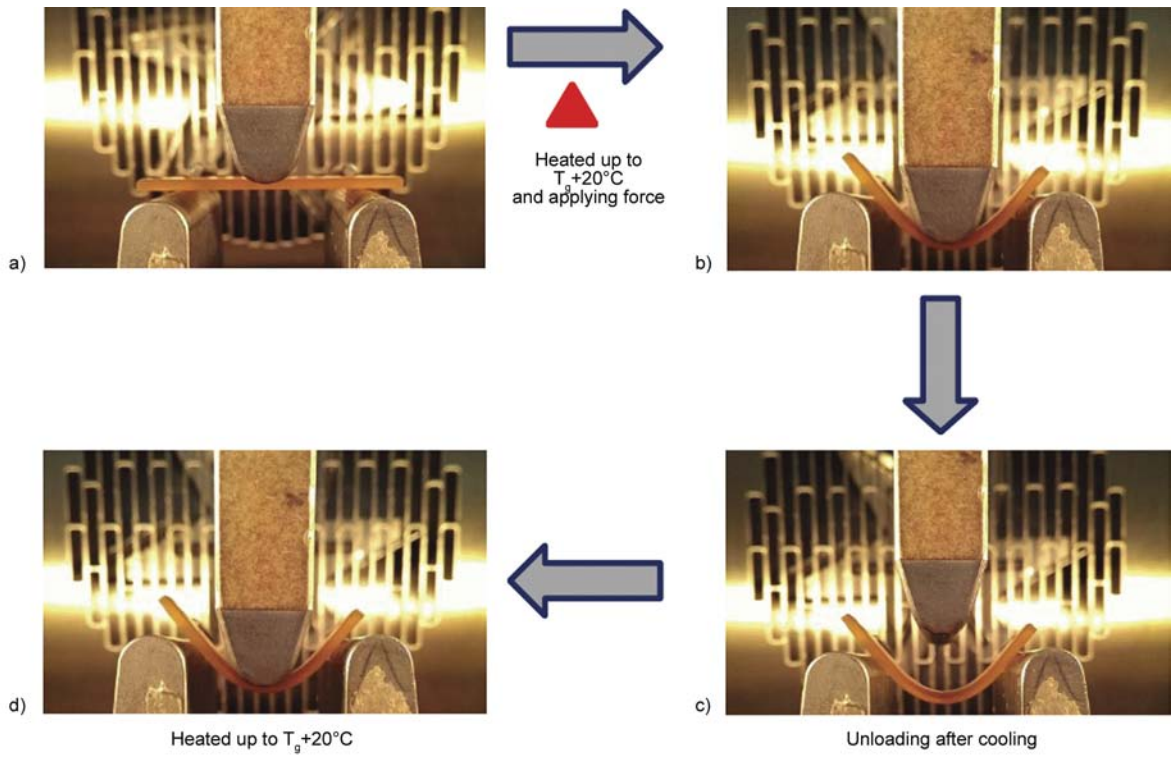

Figure 13. Photographs showing various states of bending in recovery stress process for NGDE/PBA-a SMPs: (a) permanent state of the sample at room temperature, (b) deformed state with y_{max} = 10 mm at T_g + 20°C, (c) shape-fixed state after cooling followed by unloading at room temperature for 20 min and (d) shape-recovered state after heating up to T_g + 20°C and stress during reheating was measured

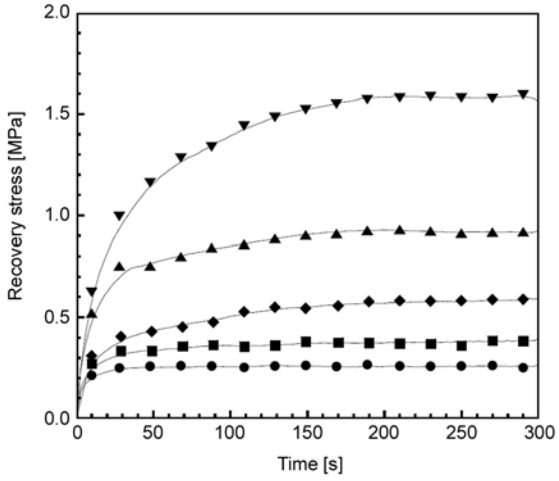

Figure 14. Recovery stress versus time of NGDE/PBA-a SMPs at various mole percents of BA-a: (●) 30 mol%, (■) 35 mol%, (◆) 40 mol%, (▲) 45 mol%, (▼) 50 mol%

has been reported that the recovery stress obtained from the TMA experiments of the commercial styrene cured with benzoyl peroxide based shape memory polymer (Veriflex VF62 of CRG Industries in Dayton, OH) was reported to be about 0.05 MPa [17]. Therefore, some of our SMPs showed a significantly high shape recovery stress that could result in complete expansive shape recovery within a spatially constraint environment such as narrowed or middle-sized vessel. In addition,the increase of the recovery stress was observed in shape memory epoxy nanocomposites [12]. It was found that at maximum SiC nano powder filler loading (20 wt%), the recovery stress of the nanocomposite was observed to be 1.5 MPa, i.e. 1 time greater than that of the neat epoxy SMP, having the recovery stress of about 0.8 MPa. Interestingly, NGDE/PBA-a SMPs can provide recovery stress about 6 times from 0.25 MPa at 30 mol% BA-a to 1.59 MPa at 50 mol% BA-a, which is substantially more than that of the epoxy SMPs nanocomposites. This is to say that the increasing of the recovery stress of the NGDE/PBA-a SMPs was due to the presence of the BA-a in the copolymers, resulting in increasing crosslink density that can enhance storage modulus at rubbery state of the copolymers [49]. Thus, the SMPs based on the polybenzoxazine is a good candidate to use for deployable structures, such as hinge [55].

4. Conclusions

Polybenzoxazine blending with aliphatic epoxy based shape memory polymer (SMP) is developed. The effect of benzoxazine resin content in aliphatic epoxy based SMPs on thermal stability, mechanical properties and shape memory properties were characterized. An incorporation of the benzoxazine resin in the aliphatic epoxy based SMP resulted in an increase of glass transition temperature, storage modulus, crosslink density and recovery stress of the SMPs. The same trend was also observed in their flexural strength and modulus at room temperature as well as in the rubbery state. Interestingly, the obtained SMPs provided an outstanding shape fixity value up to 99% at room temperature. At different active temperatures, i.e. T_g and $T_g + 20°C$, all SMPs needed only 1–3 minutes to fully recover to their permanent shape. Moreover, the addition of the benzoxazine fraction can prolong the shape recovery time of the resulting SMPs. Therefore, the obtained aliphatic epoxy/polybenzoxazine SMPs are attractive as shape memory materials to be used in a broad range of applications such as hinge or deployable structure.

Acknowledgements

This research is supported by the 90th Anniversary of Chulalongkorn University Fund and by the Ratchadaphiseksomphot Endowment Fund 2014 of Chulalongkorn University (CU-57-056-EN). Prof. S. Hiziroglu is also acknowledged for his valuable comments on this work.

References

[1] Liu Y., Du H., Liu L., Leng J.: Shape memory polymers and their composites in aerospace applications: A review. Smart Materials and Structures, **23**, 023001/1–023001/22 (2014).
DOI: 10.1088/0964-1726/23/2/023001

[2] Kolesov I. S., Radusch H-J.: Multiple shape-memory behavior and thermal-mechanical properties of peroxide cross-linked blends of linear and short-chain branched polyethylenes. Express Polymer Letters, **2**, 461–473 (2008).
DOI: 10.3144/expresspolymlett.2008.56

[3] Kang S. M., Lee S. J., Kim B. K.: Shape memory polyurethane foams. Express Polymer Letters, **6**, 63–69 (2012).
DOI: 10.3144/expresspolymlett.2012.7

[4] Ehrenstein G. W.: Polymeric materials: Structure, properties, applications. Hanser, Munich (2001).

[5] Liu L., Cai W.: Novel copolyester for a shape-memory biodegradable material *in vivo*. Materials Letters, **63**, 1656–1658 (2009).
DOI: 10.1016/j.matlet.2009.04.037

[6] Fan K., Huang W. M., Wang C. C., Ding Z., Zhao Y., Purnawali H., Liew K. C., Zheng L. X.: Water-responsive shape memory hybrid: Design concept and demonstration. Express Polymer Letters, **5**, 409–416 (2011).
DOI: 10.3144/expresspolymlett.2011.40

[7] Rimdusit S., Lohwerathama M., Hemvichian K., Kasemsiri P., Dueramae I.: Shape memory polymers from benzoxazine-modified epoxy. Smart Materials and Structures, **22**, 075033/1–075033/12 (2013). DOI: 10.1088/0964-1726/22/7/075033

[8] Leng J., Lan X., Liu Y., Du S.: Shape-memory polymers and their composites: Stimulus methods and applications. Progress in Materials Science, **56**, 1077–1135 (2011). DOI: 10.1016/j.pmatsci.2011.03.001

[9] Karger-Kocsis J., Kéki S.: Biodegradable polyester-based shape memory polymers: Concepts of (supra) molecular architecturing. Express Polymer Letters, **8**, 397–412 (2014). DOI: 10.3144/expresspolymlett.2014.44

[10] Hu J., Zhu Y., Huang H., Lu J.: Recent advances in shape–memory polymers: Structure, mechanism, functionality, modeling and applications. Progress in Polymer Science, **37**, 1720–1763 (2012). DOI: 10.1016/j.progpolymsci.2012.06.001

[11] Meng Q., Hu J.: A review of shape memory polymer composites and blends. Composites Part A: Applied Science and Manufacturing, **40**, 1661–1672 (2009). DOI: 10.1016/j.compositesa.2009.08.011

[12] Liu Y., Gall K., Dunn M. L., McCluskey P.: Thermomechanics of shape memory polymer nanocomposites. Mechanics of Materials, **36**, 929–940 (2004). DOI: 10.1016/j.mechmat.2003.08.012

[13] Santhosh Kumar K. S., Biju R., Reghunadhan Nair C. P.: Progress in shape memory epoxy resins. Reactive and Functional Polymers, **73**, 421–430 (2013). DOI: 10.1016/j.reactfunctpolym.2012.06.009

[14] Meng H., Li G.: A review of stimuli-responsive shape memory polymer composites. Polymer, **54**, 2199–2221 (2013). DOI: 10.1016/j.polymer.2013.02.023

[15] Ji F. L., Hu J. L., Li T. C., Wong Y. W.: Morphology and shape memory effect of segmented polyurethanes. Part I: With crystalline reversible phase. Polymer, **48**, 5133–5145 (2007). DOI: 10.1016/j.polymer.2007.06.032

[16] Havens E., Snyder E. A., Tong T. H.: Light actived shapem polymers and associated applications. Proceeding of SPIE, Smart Structures and Materials, **5762**, 48–55 (2005). DOI: 10.1117/12.606109

[17] Ivens J., Urbanus M., De Smet C.: Shape recovery in a thermoset shape memory polymer and its fabric-reinforced composites. Express Polymer Letters, **5**, 254–261 (2011). DOI: 10.3144/expresspolymlett.2011.25

[18] Dorigato A., Giusti G., Bondioli F., Pegoretti A.: Electrically conductive epoxy nanocomposites containing carbonaceous fillers and *in-situ* generated silver nanoparticles. Express Polymer Letters, **7**, 673–682 (2013). DOI: 10.3144/expresspolymlett.2013.64

[19] Fejős M., Karger-Kocsis J.: Shape memory performance of asymmetrically reinforced epoxy/carbon fibre fabric composites in flexure. Express Polymer Letters, **7**, 528–534 (2013). DOI: 10.3144/expresspolymlett.2013.49

[20] Xie T., Rousseau I. A.: Facile tailoring of thermal transition temperatures of epoxy shape memory polymers. Polymer, **50**, 1852–1856 (2009). DOI: 10.1016/j.polymer.2009.02.035

[21] Zheng N., Fang G., Cao Z., Zhao Q., Xie T.: High strain epoxy shape memory polymer. Polymer Chemistry, **6**, 3046–3053 (2015). DOI: 10.1039/C5PY00172B

[22] Wright W. W.: High performance polymers and composites. Wiley, New York (1991).

[23] Ishida H., Agag T.: Handbook of benzoxazine resins. Elsevier, New York (2011).

[24] Ishida H., Rimdusit S.: Very high thermal conductivity obtained by boron nitride-filled polybenzoxazine. Thermochimica Acta, **320**, 177–186 (1998). DOI: 10.1016/S0040-6031(98)00463-8

[25] Rimdusit S., Tanthapanichakoon W., Jubsilp C.: High performance wood composites from highly filled polybenzoxazine. Journal of Applied Polymer Science, **99**, 1240–1253 (2006). DOI: 10.1002/app.22607

[26] Jubsilp C., Takeichi T., Hiziroglu S., Rimdusit S.: High performance wood composites based on benzoxazine-epoxy alloys. Bioresource Technology, **99**, 8880–8886 (2008). DOI: 10.1016/j.biortech.2008.04.057

[27] Rimdusit S., Jubsilp C., Tiptipakorn S.: Alloys and composites of polybenzoxazines: Properties and applications. Springer, Singapore (2013).

[28] Jubsilp C., Rimdusit S., Takeichi T.: Aniline-based polybenzoxazine and their copolymers or composites: Molecular design and potential applications. in 'Aniline: structure/phyxical properties, reactions and environmental effects' (eds.: Hernandez K., Holloway M.) Nova Science Publishers, New York, 55–90 (2013).

[29] Jubsilp C., Punson K., Takeichi T., Rimdusit S.: Curing kinetics of benzoxazine–epoxy copolymer investigated by non-isothermal differential scanning calorimetry. Polymer Degradation and Stability, **95**, 918–924 (2010). DOI: 10.1016/j.polymdegradstab.2010.03.029

[30] Rimdusit S., Kunopast P., Dueramae I.: Thermomechanical properties of arylamine-based benzoxazine resins alloyed with epoxy resin. Polymer Engineering and Science, **51**, 1797–1807 (2011). DOI: 10.1002/pen.21969

[31] Kimura H., Matsumoto A., Hasegawa K., Ohtsuka K., Fukuda A.: Epoxy resin cured by bisphenol A based benzoxazine. Journal of Applied Polymer Science, **68**, 1903–1910 (1998). DOI: 10.1002/(SICI)1097-4628(19980620)68:12<1903::AID-APP2>3.0.CO;2-P

[32] Erden N., Jana S. C.: Synthesis and characterization of shape-memory polyurethane–polybenzoxazine compounds. Macromolecular Chemistry and Physics, **214**, 1225–1237 (2013).
DOI: 10.1002/macp.201200315

[33] Ishida H.: Process for preparation of benzoxazine compounds in solventless systems. U.S. Patent 5543516, USA (1996).

[34] Lan X., Liu Y., Lv H., Wang X., Leng J., Du S.: Fiber reinforced shape-memory polymer composite and its application in a deployable hinge. Smart Materials and Structures, **18**, 024002/1–024002/6 (2009).
DOI: 10.1088/0964-1726/18/2/024002

[35] Tobushi H., Hayashi S., Hoshio K., Makino Y., Miwa N.: Bending actuation characteristics of shape memory composite with SMA and SMP. Journal of Intelligent Material Systems and Structures, **17**, 1075–1081 (2006).
DOI: 10.1177/1045389X06064885

[36] Rimdusit S., Ishida H.: Development of new class of electronic packaging materials based on ternary systems of benzoxazine, epoxy, and phenolic resins. Polymer, **41**, 7941–7949 (2000).
DOI: 10.1016/S0032-3861(00)00164-6

[37] Liu Y., Han C., Tan H., Du X.: Thermal, mechanical and shape memory properties of shape memory epoxy resin. Materials Science and Engineering: A, **527**, 2510–2514 (2010).
DOI: 10.1016/j.msea.2009.12.014

[38] Jubsilp C., Ramsiri B., Rimdusit S.: Effects of aromatic carboxylic dianhydrides on thermomechanical properties of polybenzoxazine-dianhydride copolymers. Polymer Engineering and Science, **52**, 1640–1648 (2012).
DOI: 10.1002/pen.23107

[39] Silverstein R. M., Bassler G. C., Morrill T. C.: Spectrometric identification of organic compounds. Wiley, New York (1981).

[40] Schuh C., Schuh K., Lechmann M. C., Garnier L., Kraft A.: Shape-memory properties of segmented polymers containing aramid hard segments and polycaprolactone soft segments. Polymers, **2**, 71–85 (2010).
DOI: 10.3390/polym2020071

[41] Cao Y-P., Guan Y., Du J., Peng Y-X., Yip C. W., Chan A. S. C.: Polymer network-poly(ethylene glycol) complexes with shape memory effect. Chinese Journal of Polymer Science, **21**, 29–33 (2003).

[42] Rimdusit S., Pirstpindvong S., Tanthapanichakoon W., Damrongsakkul S.: Toughening of polybenzoxazine by alloying with urethane prepolymer and flexible epoxy: A comparative study. Polymer Engineering and Science, **45**, 288–296 (2005).
DOI: 10.1002/pen.20273

[43] Barnell T., Margraf T. W.: Healable, shape memory polymer for reflexive composites. in 'SAMPE 2008 - 52nd International SAMPE Symposium, Baltimore, USA' p.10 (2008).

[44] Rimdusit S., Tiptipakorn S., Jubsilp C., Takeichi T.: Polybenzoxazine alloys and blends: Some unique properties and applications. Reactive and Functional Polymers, **73**, 369–380 (2013).
DOI: 10.1016/j.reactfunctpolym.2012.04.022

[45] Biju R., Gouri C., Reghunadhan Nair C. P.: Shape memory polymers based on cyanate ester-epoxy-poly (tetramethyleneoxide) co-reacted system. European Polymer Journal, **48**, 499–511 (2012).
DOI: 10.1016/j.eurpolymj.2011.11.019

[46] Beblo R., Gross K., Mauck Weiland L.: Mechanical and curing properties of a styrene-based shape memory polymer. Journal of Intelligent Material Systems and Structures, **21**, 677–683 (2010).
DOI: 10.1177/1045389X10364860

[47] Hu J. L., Ji F. L., Wong Y. W.: Dependency of the shape memory properties of a polyurethane upon thermomechanical cyclic conditions. Polymer International, **54**, 600–605 (2005).
DOI: 10.1002/pi.1745

[48] Ratna D., Karger-Kocsis J.: Shape memory polymer system of semi-interpenetrating network structure composed of crosslinked poly (methyl methacrylate) and poly (ethylene oxide). Polymer, **52**, 1063–1070 (2011).
DOI: 10.1016/j.polymer.2010.12.054

[49] Rousseau I. A.: Challenges of shape memory polymers: A review of the progress toward overcoming SMP's limitations. Polymer Engineering and Science, **48**, 2075–2089 (2008).
DOI: 10.1002/pen.21213

[50] Liu Y., Sun H., Tan H., Du X.: Modified shape memory epoxy resin composites by blending activity polyurethane. Journal of Applied Polymer Science, **127**, 3152–3158 (2013).
DOI: 10.1002/app.37688

[51] Fan M., Yu H., Li X., Cheng J., Zhang J.: Thermomechanical and shape-memory properties of epoxy-based shape-memory polymer using diglycidyl ether of ethoxylated bisphenol-A. Smart Materials and Structures, **22**, 055034/1–055034/7 (2013).
DOI: 10.1088/0964-1726/22/5/055034

[52] Nji J., Li G.: A biomimic shape memory polymer based self-healing particulate composite. Polymer, **51**, 6021–6029 (2010).
DOI: 10.1016/j.polymer.2010.10.021

[53] Li G., Uppu N.: Shape memory polymer based self-healing syntactic foam: 3-D confined thermomechanical characterization. Composites Science and Technology, **70**, 1419–1427 (2010).
DOI: 10.1016/j.compscitech.2010.04.026

[54] Li G., Nettles D.: Thermomechanical characterization of a shape memory polymer based self-repairing syntactic foam. Polymer, **51**, 755–762 (2010).
DOI: 10.1016/j.polymer.2009.12.002

[55] Tandon G. P., Goecke K., Cable K., Baur J.: Environmental durability of fabric-reinforced shape-memory polymer composites. Journal of Intelligent Material Systems and Structures, **21**, 1365–1381 (2010).
DOI: 10.1177/1045389X10386265